NASA Reference Publication 1223

July 1989

Polar Microwave Brightness Temperatures From Nimbus-7 SMMR

Time Series of Daily and Monthly Maps From 1978 to 1987

Josefino C. Comiso
and H. Jay Zwally

NASA

Insert: NASA Reference Publication 1223, July 1989

NOTE

This report describes a time-series of daily brightness temperature maps produced from orbital-format data obtained from the Nimbus-7 project. Also included are monthly sea-ice concentration maps derived with a particular algorithm (Comiso, 1986). Other algorithms may produce slightly different concentrations. The Nimbus-7 SMMR Science Team algorithm (Cavalieri et al, 1984) was used by the project to produce 6-day average concentration maps (Nimbus-7 SMMR Map Tape Users Guide, SASC Technologies Document No SASC-T-5-5100-0004-0024-84) and will be used by NSIDC for processing of the SSM/I data set.

The brightness temperatures have not been corrected for some recently discovered long-term shifts in the instrument calibration, as discussed in the report.

Global Sea Ice, 1978-1987 by P. Gloersen, W.J. Campbell, D.J. Cavalieri, J.C. Comiso, C.L. Parkinson, and H.J. Zwally, NASA Special Publication (in preparation) will incorporate corrections for the long-term shifts in the instrument calibration and provide a comprehensive description of global sea ice concentrations using the Nimbus-7 SMMR Science Team algorithm.

NASA Reference Publication 1223

1989

Polar Microwave Brightness Temperatures From Nimbus-7 SMMR

Time Series of Daily and Monthly Maps From 1978 to 1987

Josefino C. Comiso
and H. Jay Zwally
Goddard Space Flight Center
Greenbelt, Maryland

National Aeronautics and Space Administration
Office of Management
Scientific and Technical Information Division

TABLE OF CONTENTS

PRECEDING PAGE BLANK NOT FILMED

LIST OF FIGURES:

POLAR MICROWAVE BRIGHTNESS TEMPERATURES FROM NIMBUS 7 SMMR:

Time Series of Daily and Monthly Maps from 1978 - 1987

Josefino C. Comiso and H. Jay Zwally

SUMMARY

A time series of daily brightness temperature gridded maps (October 25, 1978 through August 15, 1987) have been generated from all ten channels of the Nimbus-7 Scanning Multichannel Microwave Radiometer orbital data. This unique data set can be utilized in a wide range of applications including heat flux, ocean circulation, ice edge productivity, and climate studies. Two sets of data in polar stereographic format are created for the Arctic region: one with a grid size of about 30 km on a 293 by 293 array similar to that previously utilized for the Nimbus-5 Electrically Scanning Microwave Radiometer, while the other has a grid size of about 25 km on a 448 by 304 array identical to what is now being used for the DMSP Scanning Multichannel Microwave Imager. Data generated for the Antarctic region are mapped using the 293 by 293 grid only. The general technique for mapping, and a quality assessment of the data set are presented. Monthly and yearly averages are also generated from the daily data and sample geophysical ice images and products derived from the data are given. Contour plots of monthly ice concentrations derived from the data for October 1978 through August 1987 are presented to demonstrate spatial and temporal detail which this data set can offer, and show potential research applications.

1. INTRODUCTION

Multispectral brightness temperatures emitted from the earth's surface and its atmosphere were measured by the Nimbus-7 Scanning Multichannel Microwave

Radiometer (SMMR) from October 25, 1978 through August 15, 1987. SMMR is a dual polarized instrument operating at five frequencies: 6.7, 10.6, 18, 21, and 37 GHz (Gloersen and Barath, 1977). The gridded brightness temperature data described in this report have been archived at the National Snow and Ice Data Center (NSIDC, University of Colorado) and the National Space Science Data Center (NSSDC, Goddard Space Flight Center). The data are also stored in CD ROM's for easy access to personal (and other) computers. This report aims partly to document technical details and provide guidance to users of the data products. It describes how the data was gridded and generated and presents an analysis of the stability of the measured brightness temperatures during the nine years the data were collected. Some apparent instrument-related errors in the data will be discussed and suggestions for possible ways of enhancing the data set will be given. Contour maps of monthly ice concentrations from 1978 to 1987 using 37-GHz and 18-GHz dual polarized data are given to enable the user to browse through a summary of data derived from the entire data set and provide a better appreciation of the temporal and spatial detail which this product can offer.

Despite difficulty in obtaining absolute calibration, the data collected have been generally very consistent, and reflect very well the expected variations in brightness temperatures as the satellite passed by different regions and atmospheric conditions on the surface of the globe. The size of the satellite field-of-view varied from 25 km to 150 km depending on frequency, but the coverage is spatially uniform at each frequency. The temporal resolution is sufficiently good to enable on a daily basis, almost complete coverage of the polar regions except inside the 85^{o} latitude which are not covered because of the 110^{o} inclination of the satellite orbit. This microwave data set is unique, in that it provides a very comprehensive and

relatively long historical record of global microwave emissions. The data can be further converted into sea ice concentrations, ice type, snow cover, sea surface temperature, water vapor, wind speed, and other geophysical parameters with varying accuracies depending on parameter, weather, time of the day, and season (e.g., Svendson et al., 1983, Gloersen et al., 1984, Hollinger et al., 1984, Cavalieri et al., 1985, Swift et al., 1985, and Comiso, 1986). The data can also be combined with similar data sets (e.g., data from the Electrically Scanning Microwave Radiometer from 1973 to 1976, and Special Scanning Microwave Imager from 1987 to the present) for studies of long-term variability on a global scale of many geophysical parameters. Orbital brightness temperature data and certain derived geophysical parameters were produced by the Nimbus 7 project. These data have been available from NSSDC and are described in the Nimbus 7 SMMR user's guide (Fu et al., 1988).

The performance of the SMMR sensor was phenomenal throughout the almost nine years it was in operation, especially because it was expected to have a lifetime of only one to two years. It should be noted, however, that there have been evidences of degradations in the quality of the data during later years. Such degradation was more serious with the 21-GHz channel at horizontal polarization than with the other channels. When power requirements became critical in 1985 because of reduced output from the solar panels, the two 21-GHz channels were turned off permanently. Effects on the brightness temperatures of the order of two degrees in 1983 due partly to changes in the attitude of the satellite, and therefore the effective incident angle for the sensor, have also been noted. These and other instrumental effects are discussed in Section 5.

2. ORBITAL DATA SOURCE AND CELL MAPPING

The basic uncalibrated (raw) orbital data which have earth surface locations corresponding to each observation are stored in data tapes called TAT (Tapes of Antenna Temperature). The TAT data contain all the engineering parameters, including those used to calibrate the raw radiometer antenna (C_A) scalar counts. For more information than given here, the reader is referred to the Nimbus-7 SMMR User's Guide (1985). The basic algorithm used to convert the raw radiometer antenna data to brightness temperature data (T_A) is given by

$$T_A = t_W + (t_C - t_W)(C_A - C_W)/(C_C - C_W) \qquad (1)$$

where t_W and t_C are physical temperatures of warm and cold references, respectively, while C_W and C_C are the corresponding scaler counts for the same set of references measured by the radiometer. The cold and warm sources are functions of calibration constants derived from pre-launch calibrations of the instrument, and of the switch, horn, and waveguide temperatures. The data calibrated using equation (1) were further enhanced to correct for polarization mixing caused by unexpected mismatch in orthogonal polarizations measured by SMMR and the actual vertical and horizontal components. This was caused partly by leakage in the ferrite switches as described in Gloersen et al. (1980). The algorithm applied for the mixing is a first-order correction and is of the form

$$T_A{}^{V'} = a\, T_A{}^{V} + b\, T_A{}^{H} \qquad (2)$$

$$T_A{}^{H'} = a\, T_A{}^{V} + b\, T_A{}^{H} \qquad (3)$$

where the superscripts V and H stand for vertical and horizontal polarizations,

respectively, the unprimed are measured values while the primed are corrected values. Except for 37-GHz measurements, the horizontal and vertical observations are not coincident measurements but are taken sequentially. Therefore, spatial interpolation had to be applied to the SMMR data before the mixing algorithm could be applied.

The Instantaneous Fields-Of-View (IFOV) of the ten SMMR channels are given in Table 1. Also, the scanning rate and the satellite velocity are such that there is substantial overlap in the measurements from one scan to the next. The sampling frequency along track is about 13 km for 37 GHz channels and 26 of the other channels. Furthermore, the scanning mechanism of the instrument is such that the area on the earth's surface covered by each scan is sinusoidal in shape. Such a scanning pattern keeps the incidence angle constant at 50^{o} from nadir. After calibration, the orbital data are gridded into cells to simplify analysis and facilitate utilization of the multiple channel capabilities of the instrument, especially when used to derive geophysical parameters. Because of the large disparity in the sizes of the IFOV for the different channels, four grid sizes were chosen: 5 x 5, 8 x 8, 13 x 13, and 26 x 26. Thirty consecutive scans corresponding to a block size of 780 by 780 km are processed at a time. The brightness temperature representing each cell is derived from a weighted average of all the measurements overlapping the cell and weighted depending on the proximity of the center of the IFOV to the center of the cell. The weight is one when the IFOV center coincides with the center of the cell, whereas, it is zero when the IFOV center coincides with the edge of the cell. All the ten SMMR channels are mapped into the 5 x 5 grid which has a resolution of 156 km. All, except the 6-GHz channels, are mapped into 8 x 8 data elements with grid sizes of about 97.5 km. Only the 18-, 21-, and 37-GHz data are mapped into 13 x 13 cells with grid size of 60 km. Finally, only

the 37-GHz data are mapped into 26 x 26 cells with grid size of 30 km.

The SMMR cell data also provide the latitude, longitude and the incidence angle at each cell center. In addition, a day-night-twilight flag is supplied to indicate whether the spacecraft and the earth's surface inside the cell are both illuminated by the sun, or are both in shadow, or if the spacecraft is illuminated and the measured surface is in shadow. The reflected sun-boresight angles, defined as the angle between the spacecraft-to-FOV vector and the vector of the reflected sunlight from the FOV, are also calculated. This information is usually used to detect possible contamination of the antenna temperatures by the sun glint.

3. POLAR STEREOGRAPHIC GRIDDING AND DATA INTERPOLATION

The orbital SMMR data provide the best temporal resolution to study changes in brightness temperatures of a particular area on the surface of the globe. However, to examine spatial variations of brightness temperatures on a global scale, data from several orbits have to be combined and gridded using a convenient format. The polar data set described in this document utilizes the polar stereographic projection technique to map the SMMR cell data onto a 293 by 293 grid map previously utilized for ESMR data (Zwally et al., 1983). The scaling was adjusted such that each data element covers an area of about 30 km by 30 km on the surface of the globe. In this projection, a satellite observation from an area centered at latitute ϕ and longitude λ in the southern hemisphere is mapped to grid elements i and j (see Figure 1a and 1b) as follows:

$$j = 147 + d \tan \alpha \cos (90^{o} - \lambda) + 0.5 \qquad (4)$$

$$i = 147 - d \tan \alpha \sin (90^{o} - \lambda) + 0.5 \qquad (5)$$

where $\alpha = (90 - \phi)/2$, and d is the diameter of the earth expressed in pixel units. The constant 0.5 added in both equations makes the center of the map element, defined by i and j, coincident with the geographic location specified by the latitude and longitude. There is a subtle difference in the mapping procedure used for ESMR data (described in Zwally et al., 1983) and that used for the SMMR data described in this document. This involves a slight change in the value used for the parameter d. At zero-degree longitude, the number of data elements from the edge of the map to the center is 146. The value for d used to generate the current SMMR data set, has been adjusted such that the pixels at the midpoint edges of the map are entirely enclosed by the 50^{0} latitude. In the ESMR data, only three fourths of these edge pixels are enclosed by the 50^{0} latitude.

The northern hemisphere data were gridded in the same manner as the southern hemisphere data except for a change in orientation. In the southern hemisphere grid, λ longitude is along the vertical axis of the grid (Figure 1b), while in the northern hemisphere, λ longitude is 45^{0} below the horizontal axis (Figure 1c). A satellite footprint, the center of which is located at latitude ϕ and longitude λ in the northern hemisphere is mapped to grid elements i and j (Figure 1a and 1c) as:

$$j = 147 + d \tan \alpha \cos (\lambda - 45^{0}) + 0.5 \qquad (6)$$

$$i = 147 - d \tan \alpha \sin (\lambda - 45^{0}) + 0.5 \qquad (7)$$

where α and d are as previously defined.

The mapping procedure for the SSM/I grid is similar to that of the above procedure but with slight modification. Instead of the projected plane of the

grid being tangential to the earth at the north (or south) pole, it intersects the earth at the 70^{o} latitude. This would make the area of each grid more uniform within the gridded map. However, the resolution of the grid is finer at 25 km and the area covered is extended along the vertical to include the Labrador Sea and the whole of the Sea of Oshotsk as shown in Figures 2a and 2b. The satellite footprint is mapped to the SSM/I grid elements i and j using the equations:

$$j = 152 + d'\tan\alpha \cos(\lambda - 45^{o}) + 0.5 \quad (8)$$

$$i = 224 + d'\tan\alpha \sin(\lambda - 45^{o}) + 0.5 \quad (9)$$

where $d' = 0.970d$ as shown in Figure 2a.

The technique for assigning brightness temperature values to each pixel on either the SSM/I (or ESMR) grid is schematically illustrated in Figures 3a and 3b. The 37 GHz data at both horizontal and vertical polarizations were mapped on a one-on-one basis from CELL to SSM/I (or ESMR) grid because the size of the CELL 37-GHz data is approximately the same as that of the polar grid. The brightness temperature value of each CELL is assigned to the corresponding pixel in the SSM/I (or ESMR) grid which is closest to the center of the cell, as illustrated in Figure 3a. If the size of the cell is smaller or comparable to that of the SSM/I (or ESMR) grid (i.e., $p \leq q$), most of the pixels in the SSM/I (or ESMR) grid covered by the swath of the orbital data would be filled up. In some cases, SSM/I (or ESMR) pixels are not given any value because p is greater than q, as shown in Figure 3a (see grids with horizontal lines).

Since the sizes of the cells are considerably larger than the size of the SSM/I (or ESMR) grid for the other SMMR channels, a different procedure was

used to minimize the number of pixels with no data in the gridded map. The procedure adopted was to assign the same brightness temperature to all the pixels in the SSM/I (or ESMR) grid whose midpoints are within the SMMR CELL (Figure 3b). If the center of a pixel is located inside the boundary of the cell, the pixel is given the brightness temperature associated with the cell. For example, in Figure 3b, the pixels assigned with the same value are labeled with the same character (e.g., +, *, o, or x).

Examples of color coded SMMR images (reproduced in black and white) for the 18-GHz and 37-GHz channels at vertical polarizations in the ESMR grid are shown in Figure 4. The two-day-average images show that except for few data gaps (indicated by black in the image), the nearly entire Antarctic ice pack is covered by SMMR data over this period. Since the SMMR is turned off every other day, this is the best spatial coverage over a period of three successive days. An average of three adjacent daily maps (six days) is needed to fully cover the Antarctic ice pack. However, even the combined three-daily maps sometimes show some gaps at low latitudes. In the Arctic region, the areal coverage by the gridded data is the same. However, the entire northern hemisphere ice pack is not fully covered by the ESMR grid because of the presence of ice in low latitude regions, especially in areas like the Sea of Okhotsk and the Labrador Sea. To overcome the problem, the SSM/I grid was introduced. Similar examples of daily SMMR images in the SSM/I grid are shown in Figure 5. Because the pixel sizes, especially at low latitudes, are smaller than the sizes of the orbital grid elements, there are more pixels in these maps with no data as explained previously. However, the spatial coverage by the satellite at low latitudes in the daily maps is very sparse, causing lots of data gaps. To get good spatial coverage, averages over a six-day period have to be utilized. The SMMR image in Figure 5 shows the southernmost extent

of sea ice in the northern hemisphere.

Overall, brightness temperatures from all ten channels have consistent spatial representation. The different channels show the same basic information but have different sensitivity to different surface and atmospheric effects. The contrast of brightness temperatures between sea ice and water are seen to be larger at the low frequency end than the high frequency end. Also, the contrast between sea ice and water is larger at horizontal polarization than at vertical polarization. Furthermore, the expected larger sensitivity to weather and near surface effects at high frequencies than at low frequencies is evident.

4. INSTRUMENT PERFORMANCE AND CALIBRATION STUDIES

The SMMR sensor performed very well during the almost nine years (up to August 1987) it was in scanning mode. From August 1987 through August 1988, the sensor was taking data but with one beam position only, and therefore the spatial coverage was very sparse. To quantify long term behavior of the instrument, the brightness temperatures of three different types of surfaces in the polar regions were studied namely: ice free ocean, sea ice, and ice sheet. These surfaces are suitable for this study because they represent low, high and intermediate brightness temperatures, and they have predictable emission characteristics. Also, the use of three different surfaces enhances the potential of discriminating real physical change of the radiative characteristics of the surface from that associated with the instrument. The ocean study area is approximately 24,336,000 km^2 located in the southern Pacific Ocean basin. The sea ice study area, about 892,800 km^2 in size, is located in the Weddell Sea region, while the ice sheet study area of about 1,296,000 km^2 is located in the central regions of East Antarctica.

Plots of monthly brightness temperature averages at five frequencies from November 1978 to August 1987 over the three study regions are shown separately for each polarization in Figures 6 and 7. The vertical polarization graphs (Figure 6) show practically no systematic trend in the brightness temperature except that for 6 GHz which decreased by about 4 K over the ocean during the approximately nine-year period. Such drift is also discernible in the ice sheet data but is not equally obvious in the sea ice data because of the large seasonal variability for the latter.

The distributions for the horizontal polarization channels (Figure 7) also indicate no obvious systematic trend except at 21 GHz. The horizontally polarized 21-GHz channel shows an increase of almost 50 K over a seven year period. The effect is most apparent over the oceans and the ice sheets and slightly less obvious over sea ice. Such a strong interannual change should be reflected in the other channels if it was caused by a real physical change in characteristics of the emitting surface. Since the other channels do not exhibit similar behavior, the effect is likely associated with instrumental problems.

Figures 8 and 9 show minimum brightness temperature distributions from the same set of surfaces and the same study areas. These plots actually provide better quantification of long-term trends over the oceans than previous plots because the data points represent areas which are least affected by weather and other atmospheric effects (Wentz, 1983). Minimum brightness temperatures over the sea ice study area in winter should reflect leads and polynyas while those over the Antarctic ice sheet should correspond to the coldest areas or areas where the snow crystals are most granular. No obvious interannual trend at any frequency is evident.

Figures 10 and 11 show similar distributions but with the maximum

brightness temperatures plotted within the study areas. The distributions over the ocean region show considerable variability reflecting significant weather effects especially at high frequencies. On the other hand, the distributions over sea ice in winter show stability of the brightness temperatures during period at all frequencies except at 21 GHz, horizontal polarization. The maximum brightness temperature over the sea ice study area in winter represents highly consolidated first-year ice and should have minimal interannual changes because the same type of ice cover within the satellite footprint is expected to be present from one year to the next. Over the Antarctic ice sheet, high brightness temperatures are expected in areas of minimal internal scattering (fresh snow) and/or areas of relatively high physical temperatures. However, areas where the surface is slightly wet, as is possible near the coast in spring, would also show high brightness temperatures. Again, no obvious trend except that for the 21 GHz at horizontal polarization is evident from the five frequencies and at both polarizations.

Standard deviations of brightness temperatures over the same study regions are presented in Figures 12 and 13 for vertical and horizontal polarizations, respectively. The plots show that the standard deviations are of the order of 1 to 2 K at 6 GHz over the ocean and increase with frequency. At 37 GHz, large standard deviations are apparent, largely because of monthly fluctuations of atmospheric effects. The seasonality of the standard deviations is obvious for both ice sheet and sea ice surfaces. The higher standard deviation in winter than summer in the ice sheet data is caused by scattering effects associated with spatial variations in the granularity of the snow crystals. This effect is suppressed during the summer in areas where the surface is wet and therefore opaque. For sea ice, large variations are apparent during autumn and spring when the type of surface is changed dramatically (either from open water to ice

cover or from ice cover to open water).

Overall, except for the horizontally polarized 21-GHz channel, the instrumental drifts including those due to real physical processes are observed to be about 5^{o} or less. This is remarkable for an instrument which was originally designed to provide good data for two years only. For some studies like those involving sea ice, in which bootstrap analysis can be effectively implemented (Comiso, 1986), errors in the derived parameters (e.g., ice concentration) due to such instrumental drifts can be minimized. However, such instrumental problems are more difficult to deal with in other studies, such as sea surface temperature and scalar wind studies, because of more unpredictable emitting surfaces. The concern for the latter problem led to the formation of the SMMR Calibration Assessment Team (SCAT), consisting of representatives from various laboratories at Goddard Space Flight Center, to examine the overall accuracy of the SMMR calibration and determine the existence of any systematic trend related to the instrument. One of the results of the study that is relevant to this data set is the need for a correction due to the variations in incidence angle of the sensor caused by time-dependent change in the attitude of the satellite. The processing of the entire SMMR data set was nearly finished before it was discovered that the attitude of the satellite was slightly adjusted in 1983 and was therefore different from that time through August 1987. This discovery was preceeded by several studies showing some problems with the calibration (E. A. Francis, 1987, F. Wentz and D. Han, private communications, 1988). The change in attitude caused a change of about a fraction of a degree in the incidence angle for the SMMR sensor. Figures 14 and 15 show time series brightness distributions over an ocean region which illustrate the effect of not accounting for the change in incidence angle. A radiative transfer model for the ocean was used to account for this deviation.

For greater sensitivity, the "day" data, or those collected when the sensor was between the earth and the sun (as discussed previously) were plotted separately from the "night" data. The difference between the corrected and uncorrected versions in the day data is seen to be very small and is normally less than one degree and is almost random throughout the entire period. The corresponding distributions for the night data show much better agreement of corrected and uncorrected data up to 1983. This is seen in practically all the channels but the effects on each channel are not the same, especially at 21 GHz. However, since 1983, about 2 degree (or less) difference between the corrected and uncorrected brightness temperatures is apparent. Also, the corrected version makes the distribution more stable. Such a difference is important especially when data is used for evaluating time-dependent trends in sea surface temperatures, because the precision requirements for such a study are so high.

The gridded data set discussed in this report was derived from CELL data which were produced without any incidence angle correction. There is no easy procedure for making the corrections without redoing the entire data set since the gridded data already combines the night and the day data. Since the correction scheme is model dependent, it is also not easy to evaluate the errors such a procedure would introduce. It is nevertheless important that users are aware of these problems, especially when working with parameters in which such corrections might be very important. A NASA document describing these and other problems associated with the data is forthcoming.

Other trends in the data of the order of a few degrees which may be different in origin have also become apparent from studies of various surfaces. In Figure 16a, a plot of daily brightness temperatures over Greenland at 18 GHz, horizontal polarization, show that the summer minima

increased by about 4 K from 1979 to 1984. The corresponding plot using a 12 month running mean is shown in Figure 16b. The cause for this increase during the 1983-1984 period is not known but since a similar increase is not apparent in the other channels, it is believed to be caused by problems related with the instrument. Studies to resolve this and other problems are in progress.

5. ICE CONCENTRATION CONTOURS

One of the most useful parameters which can be inferred from the multispectral microwave data in the polar regions is ice concentration. The ice concentration corresponding to each pixel has been derived from the multichannel data using a bootstrap and parametrization scheme described by Comiso (1986) for the Arctic and Comiso and Sullivan (1986) for the Antarctic. The reason why bootstrapping can be done effectively is because there are areas in the Arctic and the Antarctic regions which are covered by nearly 100% ice in winter. The multispectral signatures of such areas are predictable and are then utilized, together with that for open ocean, to derive ice concentration on a global scale. The technique takes into account spatial variations in the brightness temperatures of sea ice which varies by as much as a few tens of degrees Kelvin, depending on frequency. In the Central Arctic region, the data points for 100% ice follow a predictable linear pattern as shown in the scatter plot for horizontal versus vertical polarizations at 37 GHz (Figure 17). The consolidated ice data follow a line with slope almost equal to 1 (1.04) and standard deviation of about 2.5 K about the line. This makes it possible to obtain ice concentration with the set of channels that provides the best resolution and with an accuracy of about 3 % in the Central Arctic region where open water has been reported to be usually less than 10 %. In regions other than the Central Arctic, the 18-GHz and 37-GHz channels at vertical resolution

are utilized. Although this set of channels affords less accuracy than the previous set in consolidated ice areas, it provides more consistent retrievals in the marginal sea ice region and enables removal of much of the superficial ice cover in the open ocean caused by weather effects (Comiso et al., 1984, Comiso and Sullivan, 1986, Gloersen and Cavalieri, 1986). The advantage of using of 18 GHz and 37 GHz channels at vertical polarizations over 37 GHz at both polarizations is illustrated in Figure 18. It is clear that some ambiguities in the interpretation of consolidated ice and of open water could arise if only 37 GHz channel at both polarizations are available.

Contour maps of ice concentrations derived using the technique discussed previously are shown in Figures 19-37 for the Antarctic region and Figures 38-54 for the Arctic region. Three contours are shown namely: 15%, 50%, and 85%, ice cover. A similar set of contours have been shown for the Antarctic region (1974-1976) in Zwally et al., 1983 using ESMR data, but only one contour (15%) were used in the corresponding Arctic data set (Parkinson et al., 1987) because the one channel sensor could not be used effectively for deriving ice concentration in the multiyear ice region.

The contour maps concisely show areas covered by ice during different times of the year and different years. Areas of significantly reduced ice concentrations within the consolidated ice regions are usually revealed by the 85% contours. Some examples are the 85% contours near the Maud Rise (5^{o}E) and the Cosmonaut Sea (40^{o}E) in July and August 1980, respectively, in the southern hemisphere, and those in the Central Arctic during mid winter. The 50% contours represent intermediate ice-covered areas but may have to be interpreted in a different context in many cases because of ambiguities caused by new ice and young ice. The emissivities of new ice and young ice have been observed to be intermediate to that of open water and thick first-year ice.

The values depend on thickness, stage in the growth cycle, and temperature of the ice (Grenfell and Comiso, 1986). Thus, the 15-50% contours might actually represent large areas of new ice and young ice with higher ice concentrations. Although the accuracy is not very high, these characterizations are useful because they indicate areas of rapid change due to growth, decay, and atmospheric or oceanic forcing.

In the summer, there are regions which are supposed to be ice free in the continental coastline around Antarctica as indicated by in situ observations and other satellite sensors. The SMMR data sometimes indicate a few percent concentration in these areas instead. This is caused by a smearing in the coverage caused partly by antenna side lobe effects and partly by a larger antenna footprint than the actual sizes of the grids. Similar effects are expected in other areas including those not covered by sea ice (e.g., Great Britain, Iceland, etc.). This effect is not seen around South America because a rectangular area around it was masked and not included in the contour analysis. It is, however, important that the data near land-ocean (or ice-ocean) boundaries are treated with caution.

The contour maps reflect the spatial and temporal detail which could be obtained from the brightness temperature maps discussed in this document. Except for the every-other-day coverage and lack of data inside the 85^{o} latitudes, data gaps are minimal and this data set should be ideal for time series as well as spatial variation analyses. The study of sea ice cover is only one of the many applications which can be derived from the 10-channel data set. Other parameters with strong potential are surface temperatures, scalar winds, water vapor, and rainfull (e.g., Gloersen et al., 1980). While the polar regions are just a small subset of the global system, its relevance to climate studies, ocean circulation and biological productivity has been

stressed in the current literature.

6. DATA FORMAT AND STORAGE

The SMMR data set consists of sequences of maps stored in arrays, each with a header record. There are ten maps for each day arranged from the highest frequency to the lowest frequency and alternating between vertical and horizontal polarizations. The every other day maps from October 25, 1978 through August 15, 1987 are then arranged chronologically for each hemisphere and stored on magnetic tapes as separate files. The header record for each file, which is similar for both ESMR and SSM/I grids, is described in Table 2. The format of the 293 by 293 maps (ESMR grid) is given in Table 3. The maps are recorded such that each record has 293 words to make up for 294 records including that for the header. In some versions of the data set, a population record 293 words long was also added after each data record making the total number equal to 587 records. A sample program for reading the data is given in the Appendix. The format of the 448 by 304 maps (SSM/I grid) is given in Table 4. Except for the length of each record and the number of records in each file the data storage format for these maps is the same as that used for the 293 by 293 maps.

Another set of orbital SMMR data called TCT has also been generated at Goddard Space Flight Center (Gloersen, 1988). This data set is different from the orbital CELL data in that no gridding was done and therefore the original resolution of each beam position measurement is preserved. The calibration is also adjusted to make the brightness temperatures more consistent with model results. Gridded maps from the two data sets, however, are basically identical, except for the slight difference in resolution. One set of data can be converted to the other using the linear transformation given in Table 5.

REFERENCES:

Cavalieri, D. J., P. Gloersen, and W.J. Campbell, Determination of sea ice parameters with the Nimbus 7 SMMR, *J. Geophys. Res., 89*, 5355-5369, 1984.

Comiso, J.C., Sea ice effective microwave emissivities from satellite passive microwave and infrared observations, *J. Geophys. Res., 88*, 7686-7704, 1983.

Comiso, J.C., Characteristics of winter Arctic sea ice using multispectral microwave observations, *J. Geophys. Res., 91*, 975-994, 1986.

Comiso, J.C., and C.W., Sullivan, Satellite microwave and in situ observations of the Weddell Sea ice cover and its marginal ice zone, *J. Geophys. Res. 91*, 9663-9681, 1986.

Comiso, J.C., S.F. Ackley, and A.L. Gordon, Antarctic sea ice microwave signatures and their correlation with in situ observations, *J.Geophys. Res., 89*, 662-672, 1984.

Francis, E.A., Calibration of the Nimbus-7 Scanning Multichannel Microwave Radiometer (SMMR), 1979-1984, Master Thesis. Oregon State University, 248 pp., October, 1987.

Fu, C.C., D. Han, S. T. Kim, and P. Gloersen, User's guide for the Nimbus 7 Scanning Multichannel Microwave Radiometer (SMMR) CELL-ALL Tape, *NASA RP 1210* 158 pp., 1988.

Gloersen, P., and F.T. Barath, A scanning multichannel microwave radiometer for Nimbus-G and SeaSat-A, *IEEE J. of Oceanic Engr., OE-2*, 172-178, 1977.

Gloersen, P., D.J. Cavalieri, and H.V. Soule, An alternative algorithm for correction of the scanning multichannel microwave radiometer polarization radiances using Nimbus-7 scanning multichannel radiometer, in *Oceanography in Space*, ed. by J.R. F. Gower, pp. 823-829, Plenum, New York, 1981.

Gloersen, P, D.J. Cavalieri, A.T.C. Chang, T.T. Wilheit, W.J. Campbell, O.M. Johannessen, K.B. Katsaros, K.F. Kunzi, D.B. Ross, D. Staelin, E.P.L.

Windsor, F.T. Barath, P. Gudmandsen, E. Langham, and R.O. Ramseier, A summary of results from the first Nimbus 7 SMMR Observation, *J. Geophys. Res., 89,* 5335-5344, 1984.

Grenfell, T.C., and J.C. Comiso, Multifrequency passive microwave observations of first year sea ice grown in a tank, *IEEE Trans. Geoscience and Remote Sensing, GE-24,* 826-831, 1986.

Hollinger, J.P., B.E. Troy, R.O. Ramseier, K.W. Asmus, M.F. Hartman, and C.A. Luther, Microwave emission from high Arctic sea ice during freeze-up, *J. Geophys. Res., 89,* 8104-8122, 1984.

Parkinson, C.L., J.C. Comiso, D.J. Cavalieri, H.J. Zwally, P. Gloersen, and W.J. Campbell, Arctic Sea Ice, 1973-1976: Satellite Passive Microwave Observations, *NASA Spec. Publ. 489,* 296 pp., 1987.

Svendsen, E., K. Kloster, B. Farrelly, O.M. Johannessen, J.A. Johannessen, W.J. Campbell, P. Gloersen, D. Cavalieri, and C. Matzler, Norwegian Remote Sensing Experiment: Evaluation of the Nimbus 7 scanning multichannel microwave radiometer for sea ice research, *J. Geophys. Res., 88,* 2755-2769, 1983.

Swift, C.T., L.S. Fedor, and R.O. Ramseier, An algorithm to measure sea ice concentration with microwave radiometers, *J. Geophys. Res., 90,* 1087-1099, 1985.

Wentz, F. J., A model function for ocean microwave brightness temperature, *J. Geophys. Res., 88 (C3),* 1892-1908, 1983.

Zwally, H.J., J.C. Comiso, C.L. Parkinson, W.J. Campbell, F.D. Carsey, and P. Goersen, Antarctic sea ice 1973-1976 from satellite passive microwave observations, *NASA Spec. Publ. 459,* 224 pp., 1983.

Table 1

The Instantaneous-Fields-Of-View (IFOV) of the ten SMMR channels

Channel	Frequency	Wavelength	Polarization	IFOV (km)
1-2	6.6 GHz	4.55 cm	H and V	148 x 95
3-4	10.7 GHz	2.81 cm	H and V	91 x 59
5-6	18.0 GHz	1.67 cm	H and V	55 x 41
7-8	21.0 GHz	1.43 cm	H and V	46 x 30
9-10	37.0 GHz	0.81 cm	H and V	27 x 18

Table 2

Header Record for Polar Stereographic Maps

Word	Type	Number of bytes/word	Description
1	I6	6	Projection type (1 for polar stereo)
2	I6	6	Number of columns (293 for ESMR grid, 304 for SSMI grid)
3	I6	6	Number of rows (293 for ESMR grid, 448 for SSMI grid)
4	I6	6	Scale (2.5×10^6)
5	I6	6	Latitude Enclosed (50^o for ESMR grid $40\text{-}44^o$ for SSMI grid
6	I6	6	Greenwich Orientation
7	I6	6	Radius of the Earth
8	I6	6	J-coordinate of the Pole (147 for ESMR, 157.5 for SSMI)
9	I6	6	I-coordinate of the Pole (147 for ESMR, 224.5 for SSMI)
10-11	A6	6	Data Type (TB for brightness temp., IC for Ice Concentration, etc.)
12	I6	6	Start time (day)
13	I6	6	Start time (hour)
14	I6	6	Start time (minutes)
15	I6	6	Stop time (day)
16	I6	6	Stop time (hour)
17	I6	6	Stop time (minutes)
18	I6	6	Year data was collected
19	I6	6	Data Format (2 for standard)
20	A6	6	Data Identification
21-153	I5	6	Meaningless

Table 3

Standard Format for Polar Stereographic Maps (ESMR grid)

Record Number	Length (bytes)	Format	Number of Words	Description
1	586	(see below)+	293	Header Record
2	586	293 A2	293	Row 1, TB*50
3	586	293 A2	293	No of Obs. in Row 1
4	586	293 A2	293	Row 2, TB*50
5	586	293 A2	293	No of Obs. in Row 2
.				
.				
.				
586	586	293 A2	293	Row 293 TB*50
587	586	293 A2	293	No of Obs. in Row 293

+ (9I6,2A6,8I6,A6,269I5)

Table 4

Standard Format for Polar Stereographic Maps (SSM/I grid)

Record Number	Length (bytes)	Format	Number of Words	Description
1	608	(see below)+	304	Header Record
2	608	304 A2	304	Row 1, TB*50
3	608	304 A2	304	No of Obs. in Row 1
4	608	304 A2	304	Row 2, TB*50
5	608	304 A2	304	No of Obs. in Row 2
.				
.				
.				
896	608	304 A2	304	Row 448 TB*50
897	608	304 A2	304	No of Obs. in Row 448

+(9I6,2A6,8I6,A6,280I5)

Table 5

CELL to TCT Calibration Conversion

Channel	Frequency (GHz)	a	b	sigma
1	6.6 V	18.0	0.939	0.62
2	6.6 H	-2.6	1.005	0.59
3	10.7 V	16.3	0.950	0.40
4	10.7 H	-1.4	1.001	0.58
5	18.0 V	24.9	0.913	0.69
6	18.0 H	-5.8	1.017	0.93
7	21.0 V	25.4	0.902	1.20
8	21.0 H	-32.8	1.118	1.30
9	37.0 V	20.2	0.943	0.83
10	37.0 H	-11.4	1.043	1.35

APPENDIX: SAMPLE FORTRAN PROGRAMS TO READ THE DATA TAPES.

1. **ESMR Format**

```
      DIMENSION IHEAD(20),AHEAD(20)
      INTEGER *2  IBT(293)
      EQUIVALENCE (IHEAD(1),AHEAD(1))
      INTEGER IDUM (132)
      READ (8,500) (IHEAD(J),J=1,20),IDUM
      DO 50 I=1,293
      READ (8,550) IBT
      READ (8,550) IPOP
   50 CONTINUE
  500 FORMAT (1X,9I6,2A6,9I6,5X,I5)
  550 FORMAT (255A2,38A2)
```

2. **SSM/I Format**

```
      DIMENSION IHEAD(20),AHEAD(20)
      INTEGER *2  IBT(304)
      EQUIVALENCE (IHEAD(1),AHEAD(1))
      INTEGER IDUM (132)
      READ (8,500) (IHEAD(J),J=1,20),IDUM
      DO 50 I=1,448
      READ (8,550) IBT
      READ (8,550) IPOP
   50 CONTINUE
  500 FORMAT (1X,9I6,2A6,9I6,5X,I5)
  550 FORMAT (255A2,49A2)
```

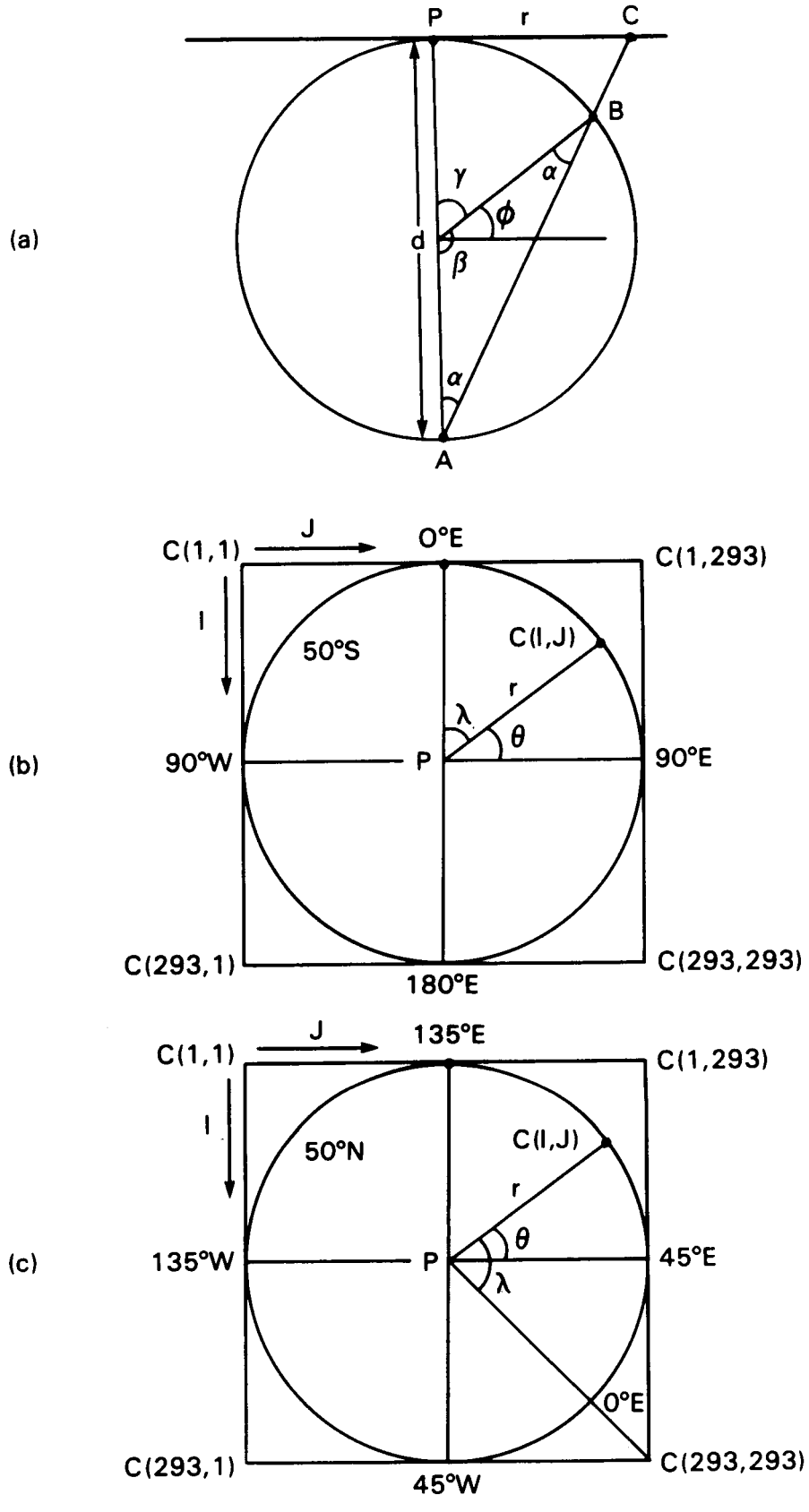

Figure 1. Schematic Diagram for Polar Stereographic Mapping using the ESMR grid.

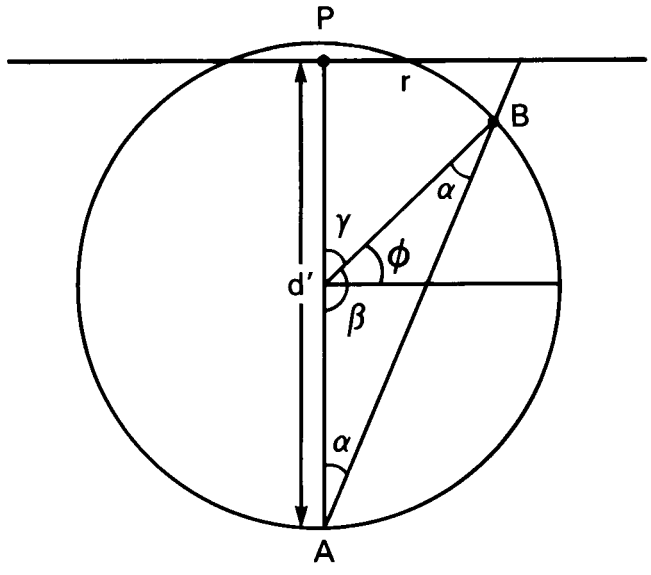

(a)

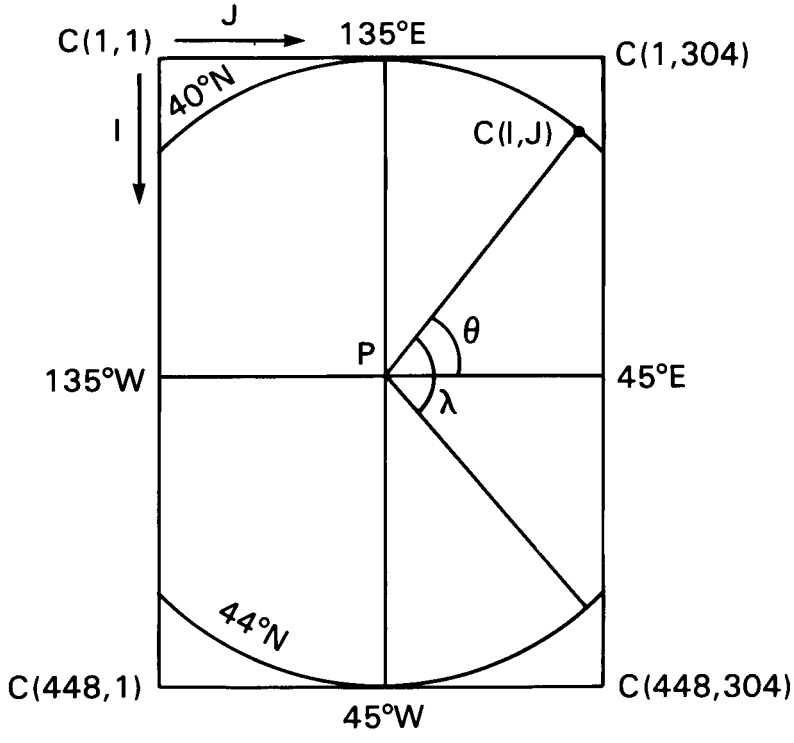

(b)

Figure 2. Schematic Diagram for Polar Stereographic Mapping using the SSM/I grid.

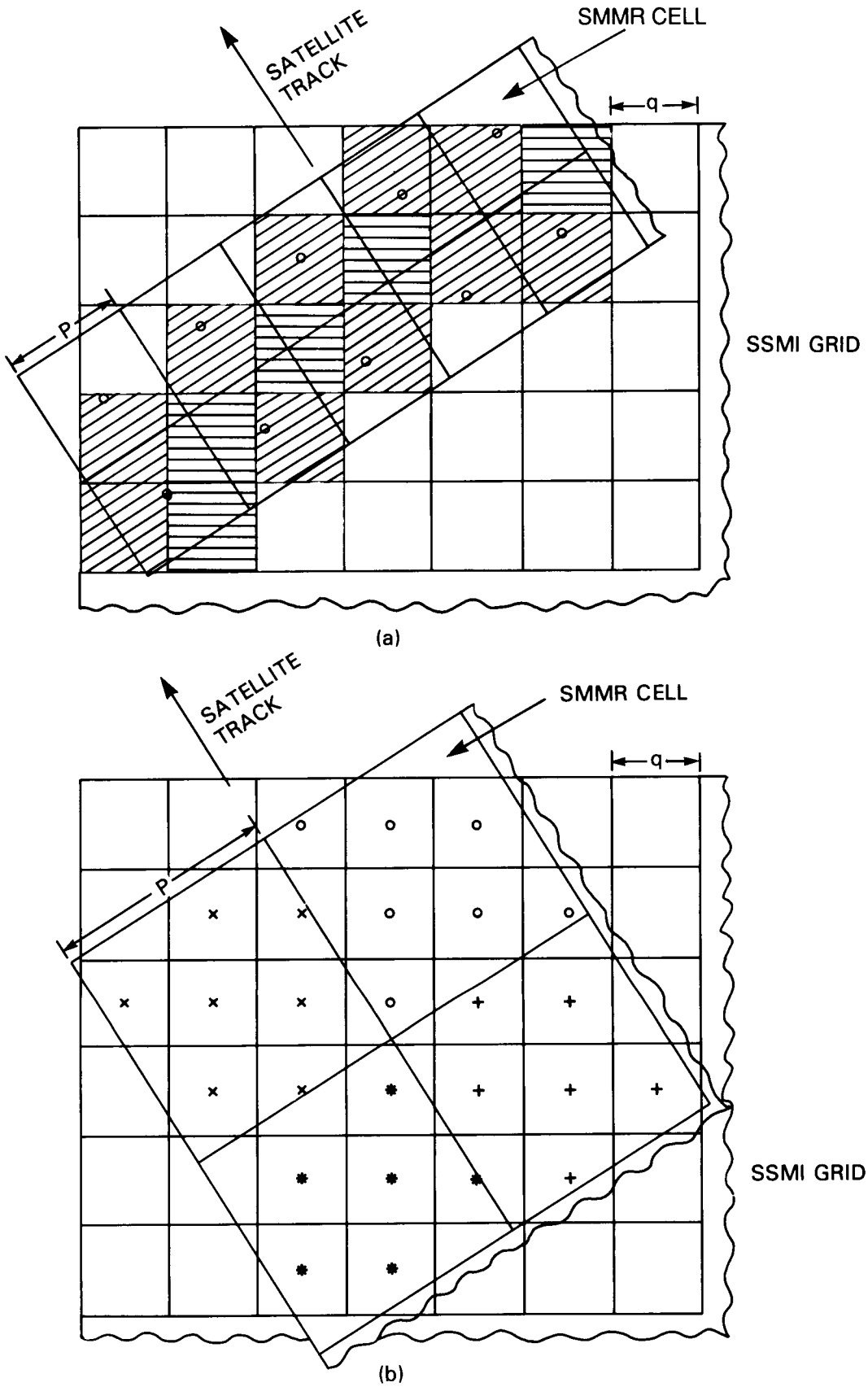

Figure 3. Mapping of orbital CELL data to Polar gridded data for (a) 37 GHz channels and (b) all other channels.

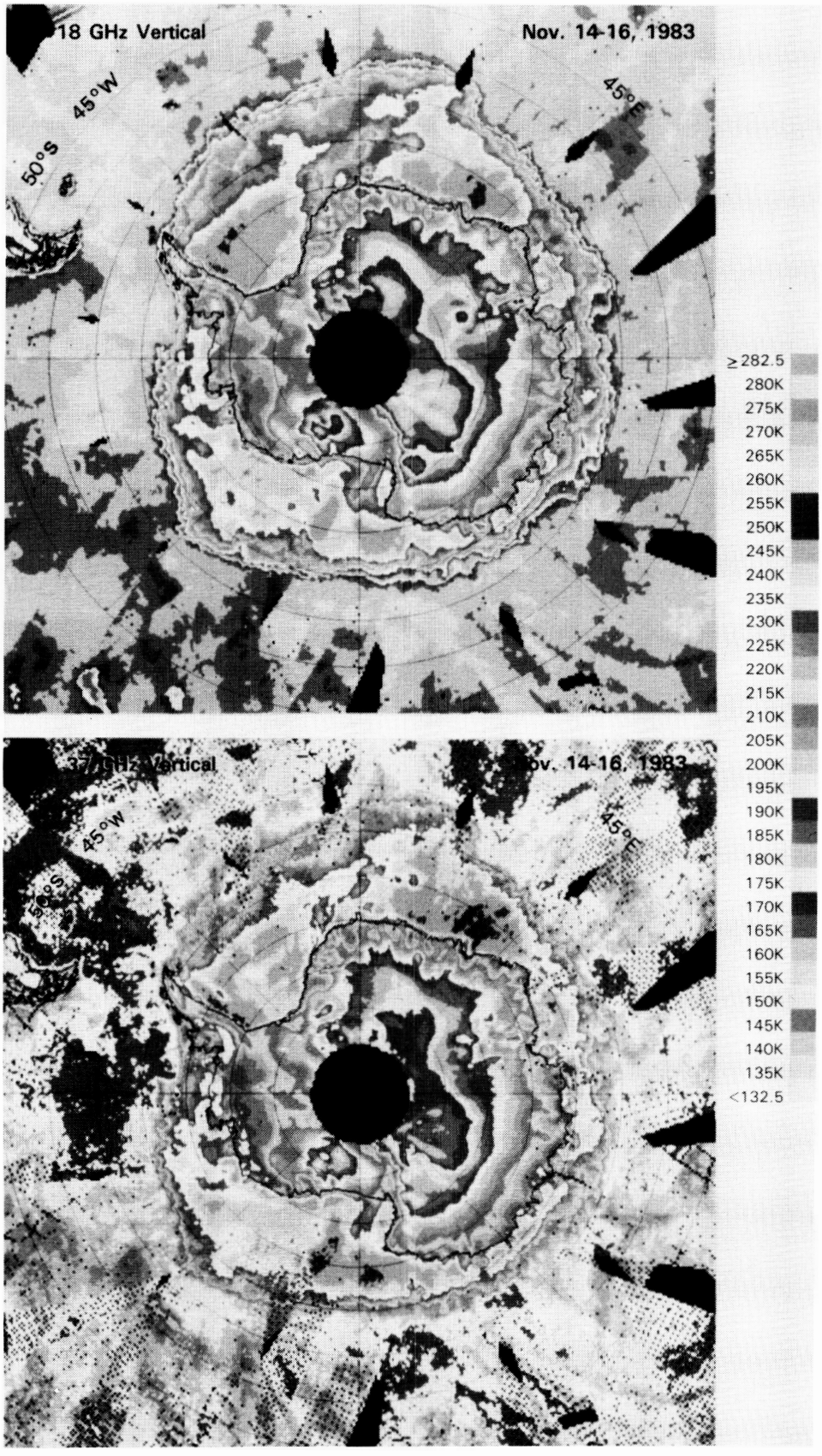

Figure 4. Sample 2-daily average polar maps of Antarctic brightness temperatures (18 GHz and 37 GHz at vertical polarization) using the ESMR grid.

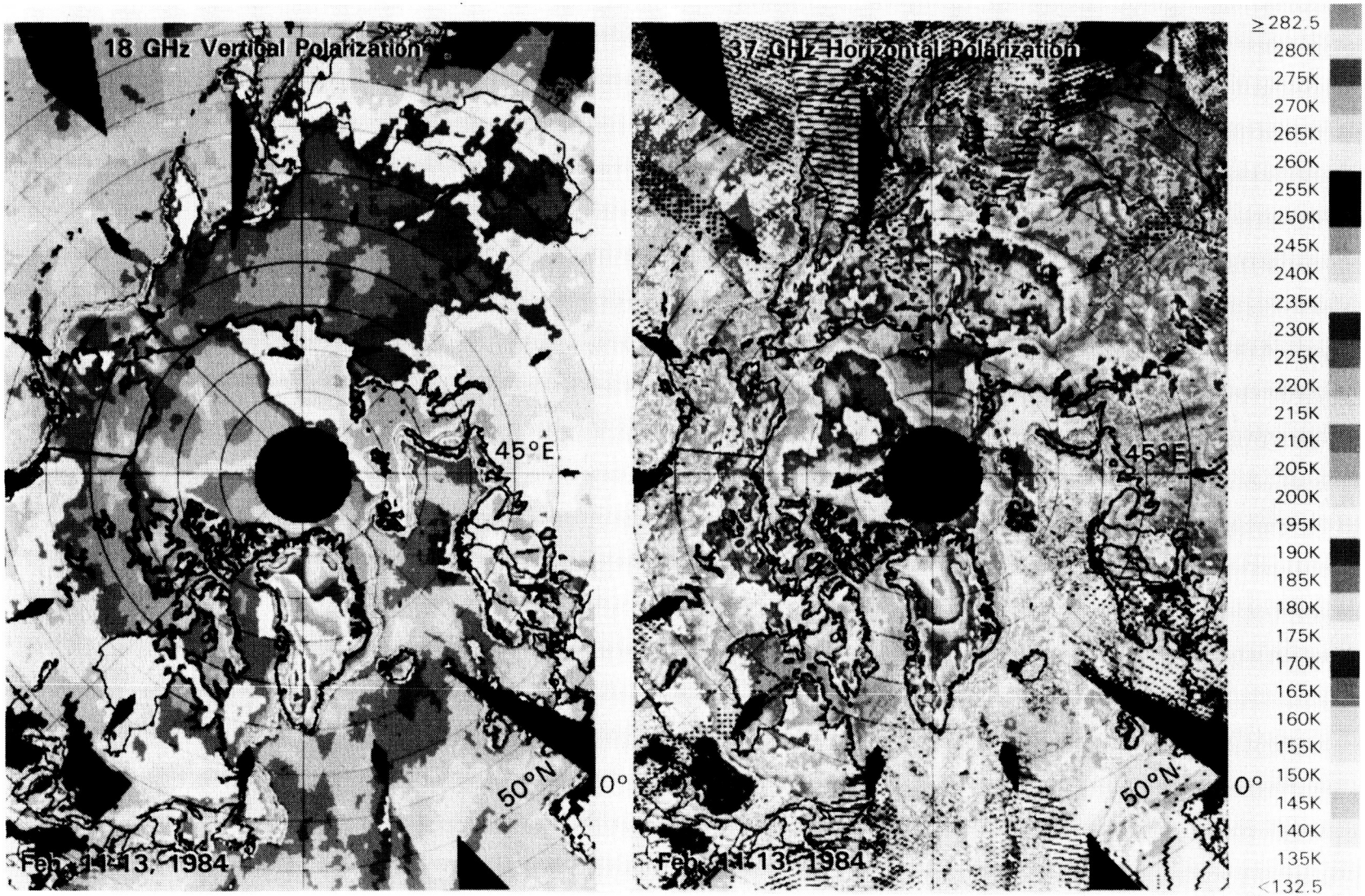

Figure 5. Sample 2-daily average polar maps of Arctic brightness temperatures (18 GHz vertical and 37 GHz horizontal) using the SSMI grid.

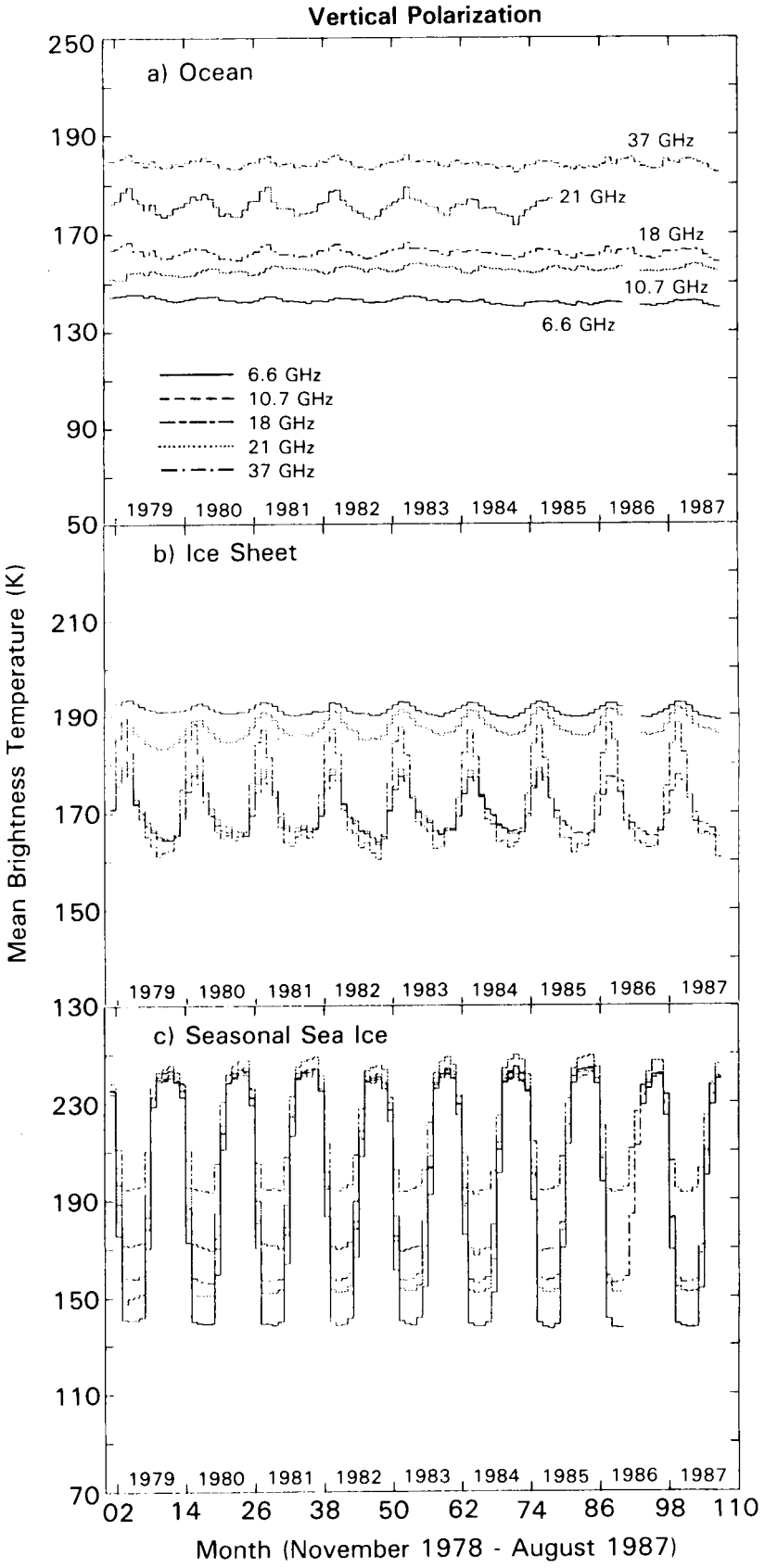

Figure 6. Time series of monthly mean T_B at vertical polarization: 1978-1987.

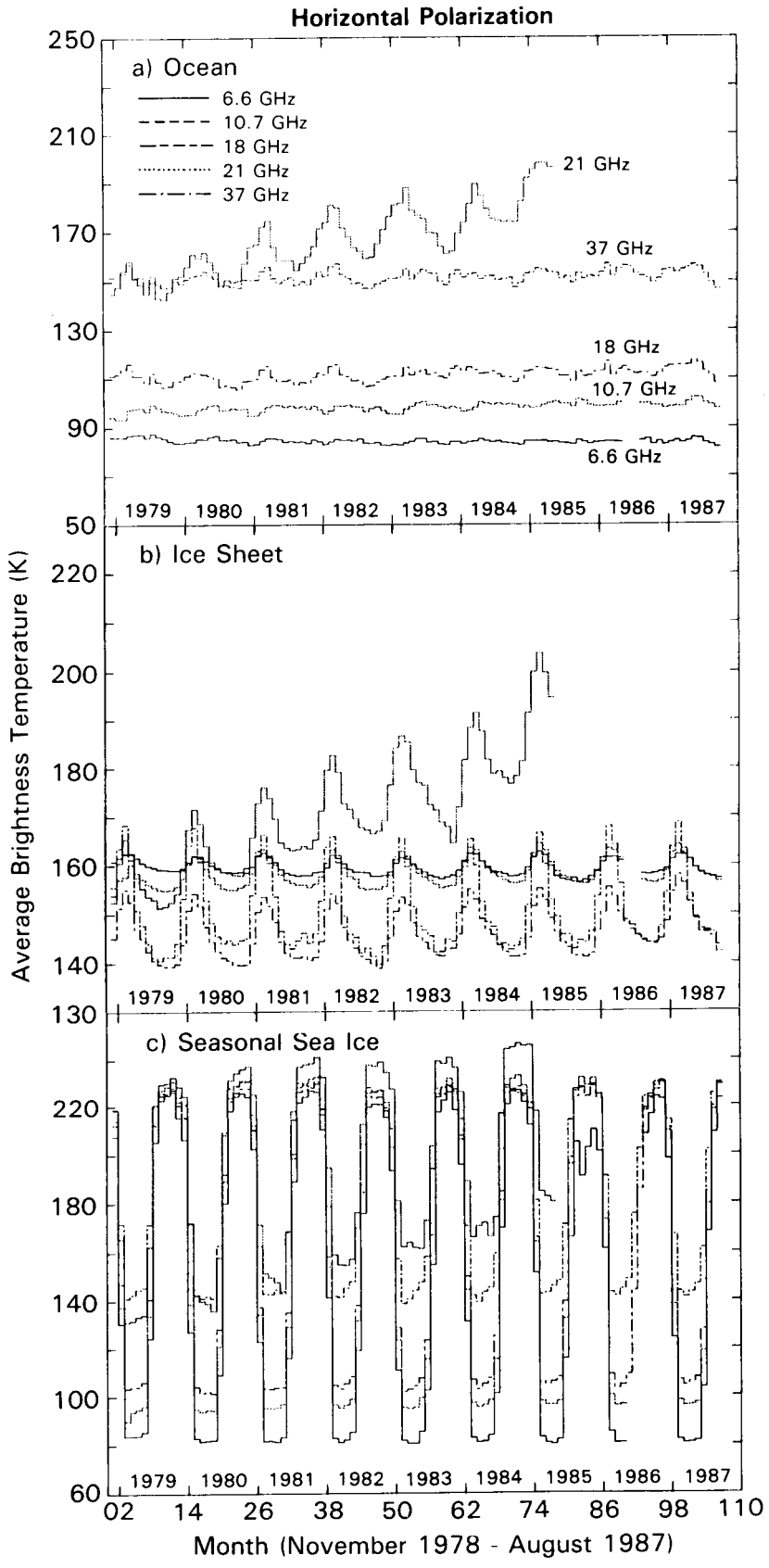

Figure 7. Time series of monthly mean T_B at horizontal polarization: 1978-1987.

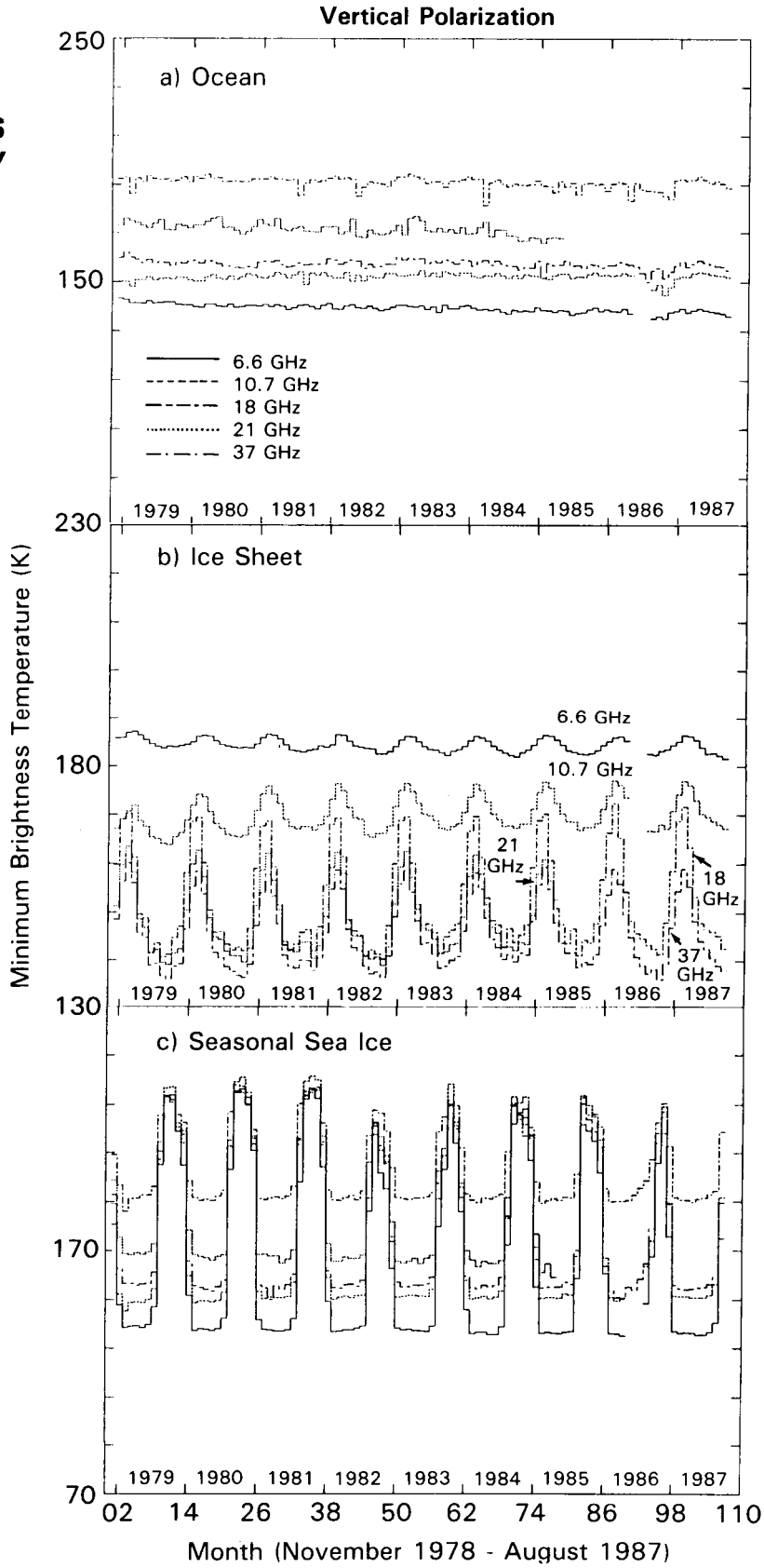

Figure 8. Time series of monthly minimum T_B at vertical polarization: 1978-1987.

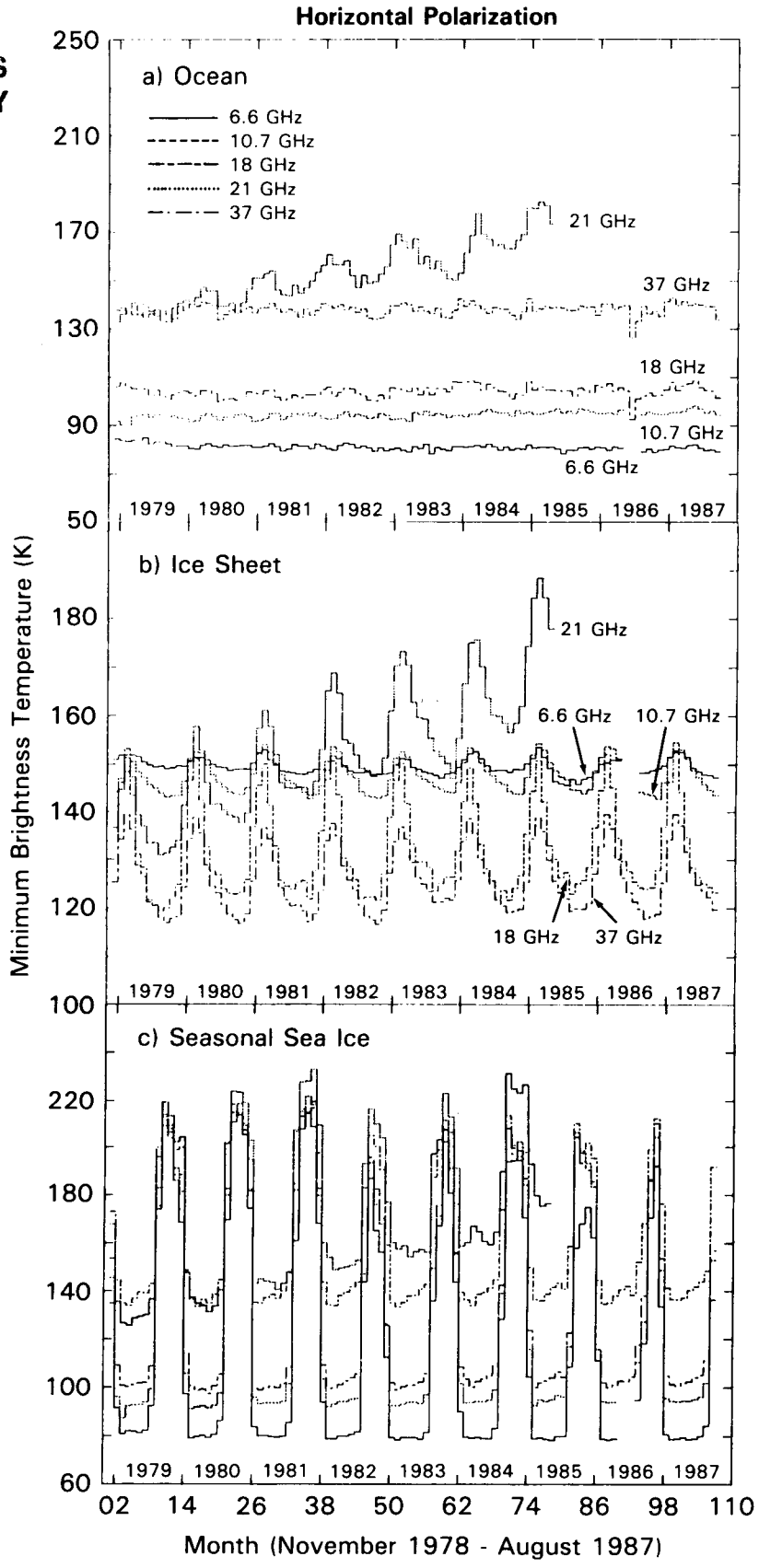

Figure 9. Time series of monthly minimum T_B at horizontal polarization: 1978-1987.

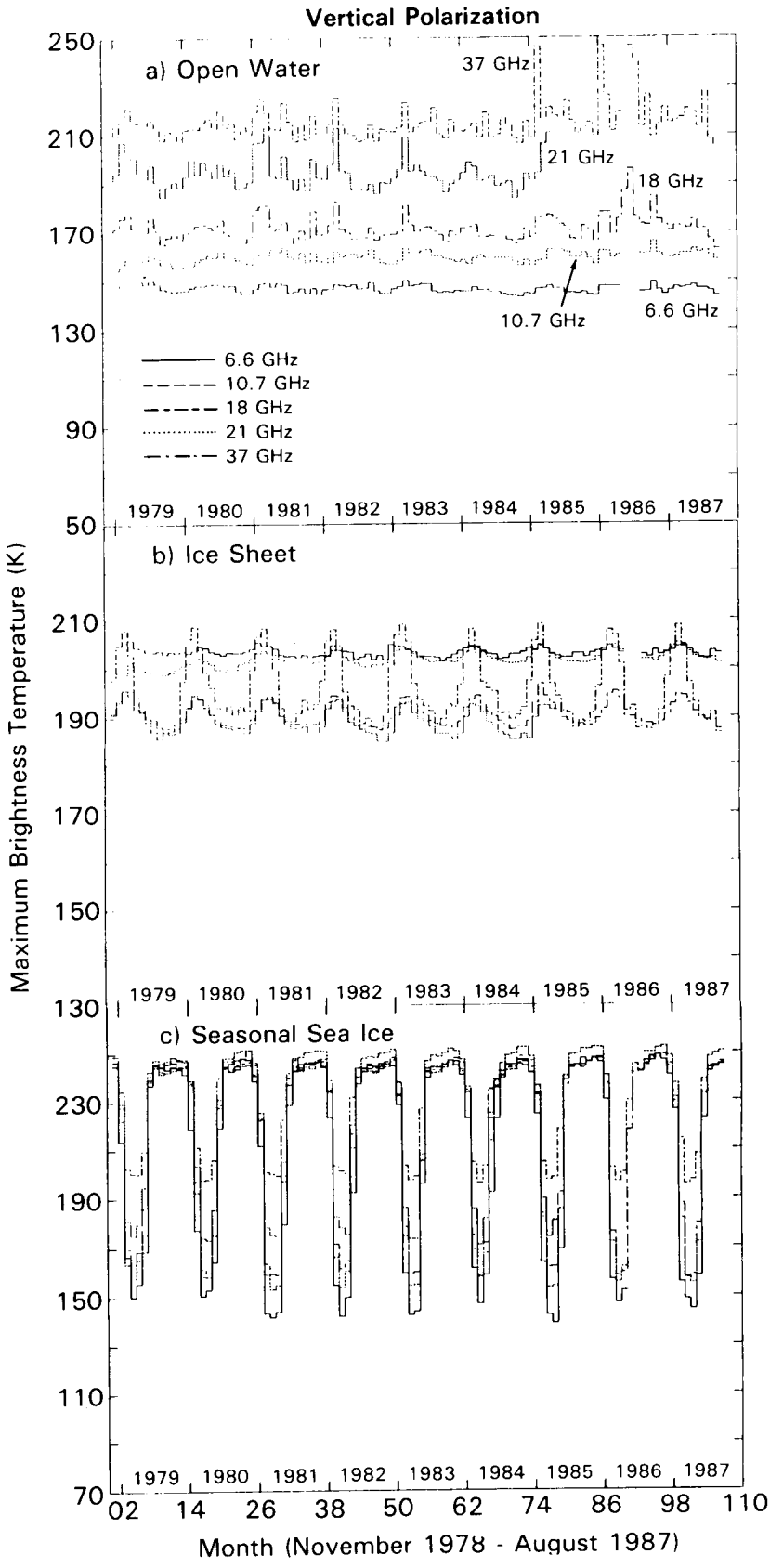

Figure 10. Time series of monthly maximum T_B at vertical polarization: 1978-1987.

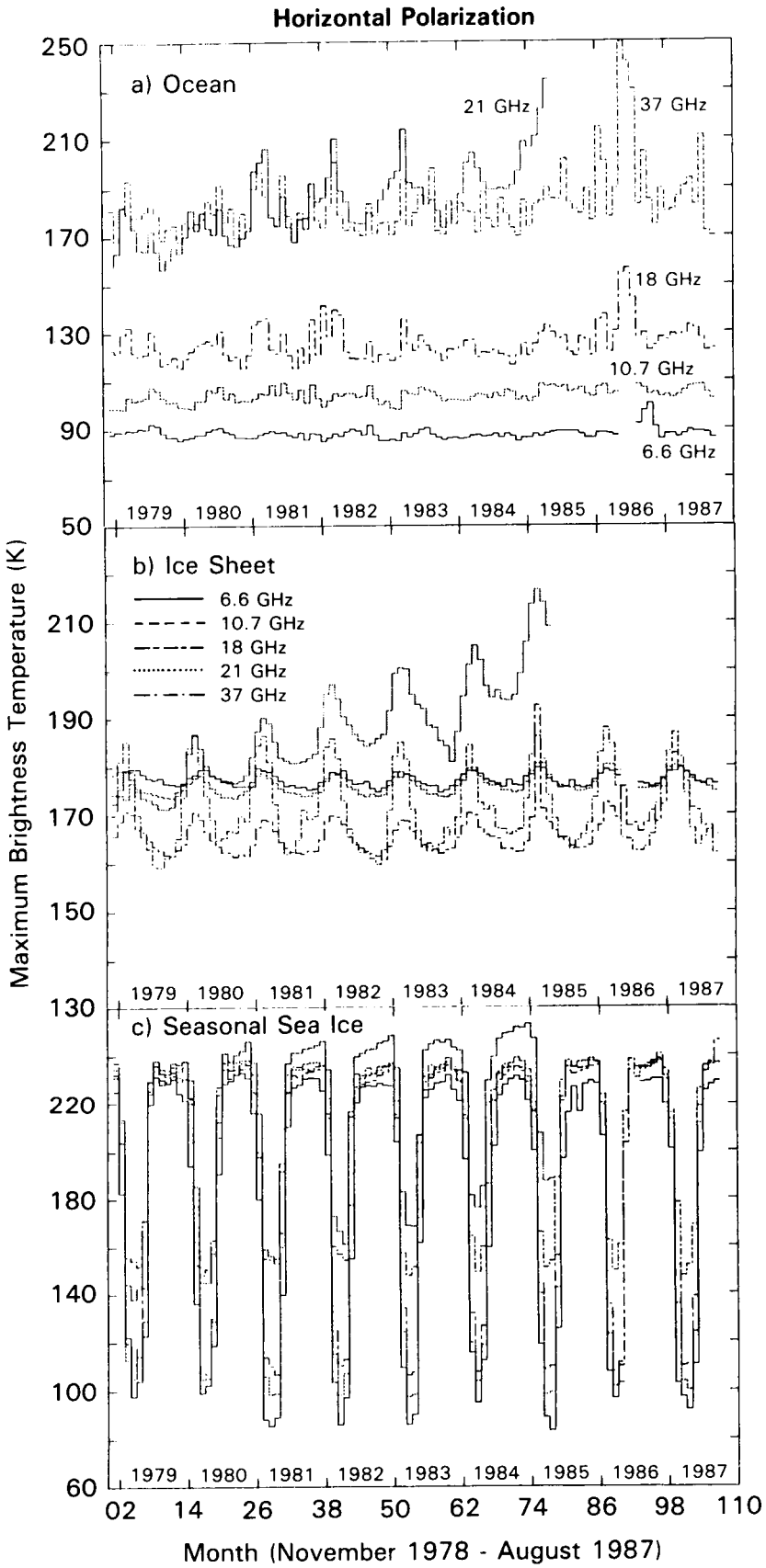

Figure 11. Time series of monthly maximum T_B at horizontal polarization: 1978-1987.

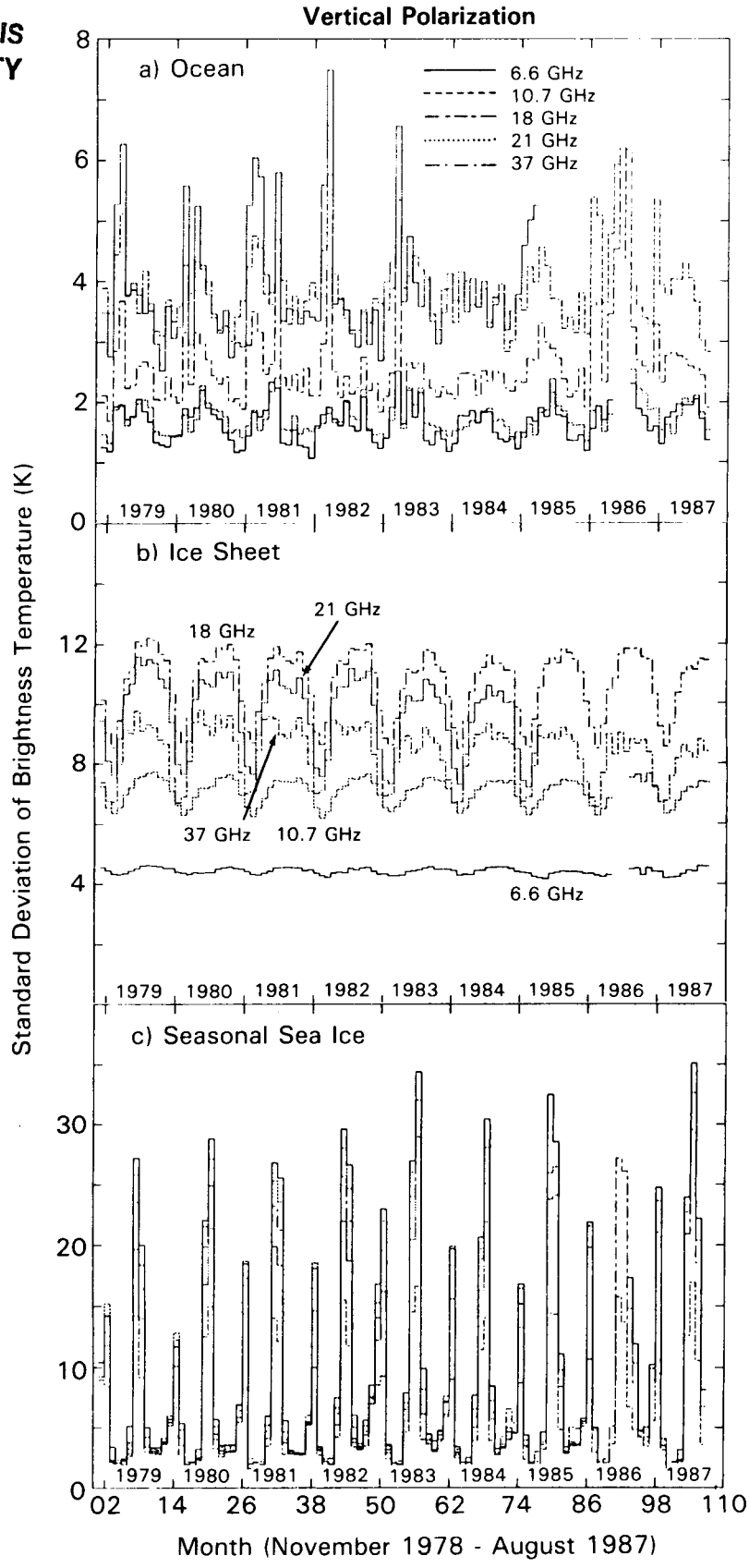

Figure 12. Time series of monthly standard deviations of T_B at vertical polarization: 1978-1987.

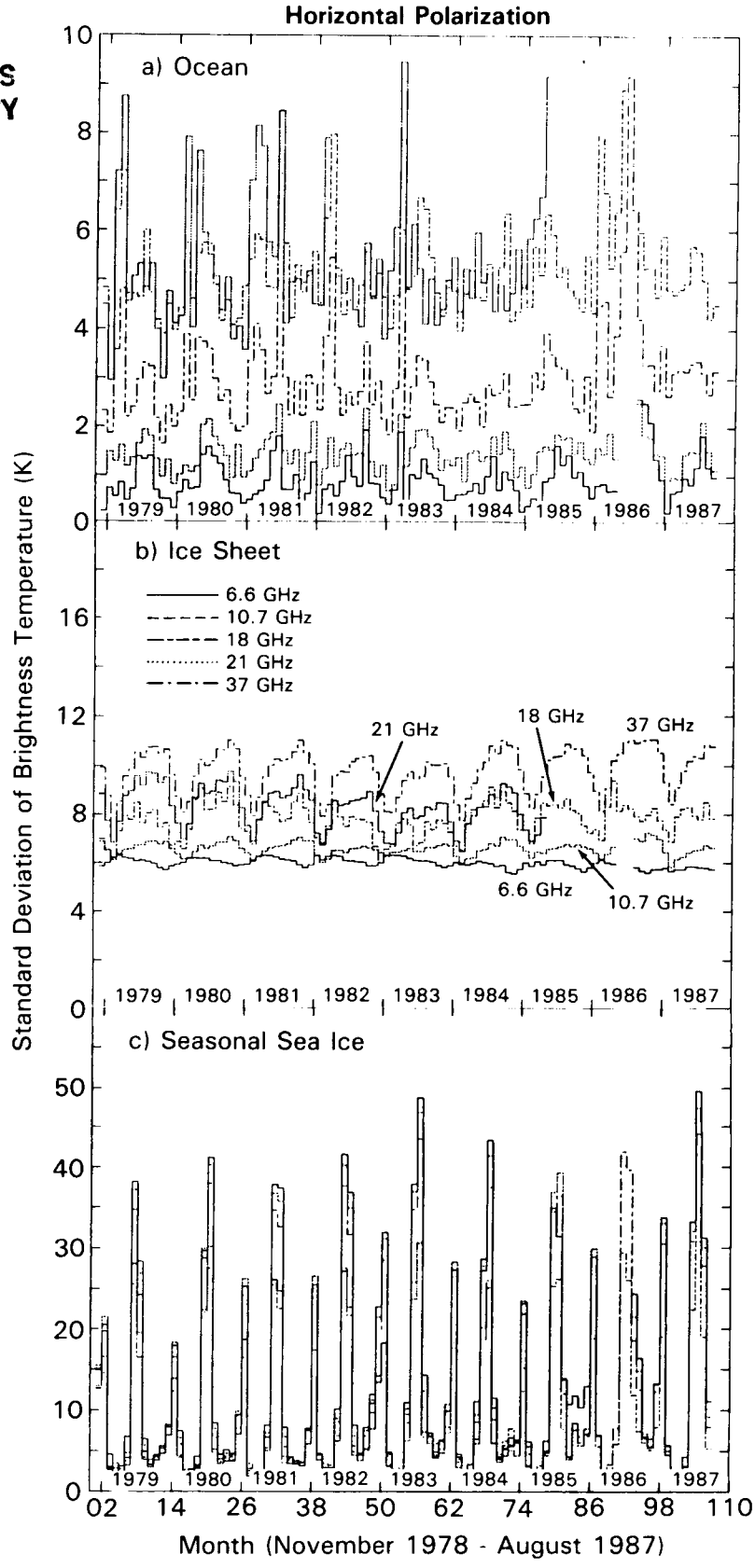

Figure 13. Time series of monthly standard deviations of T_B at horizontal polarization: 1978-1987.

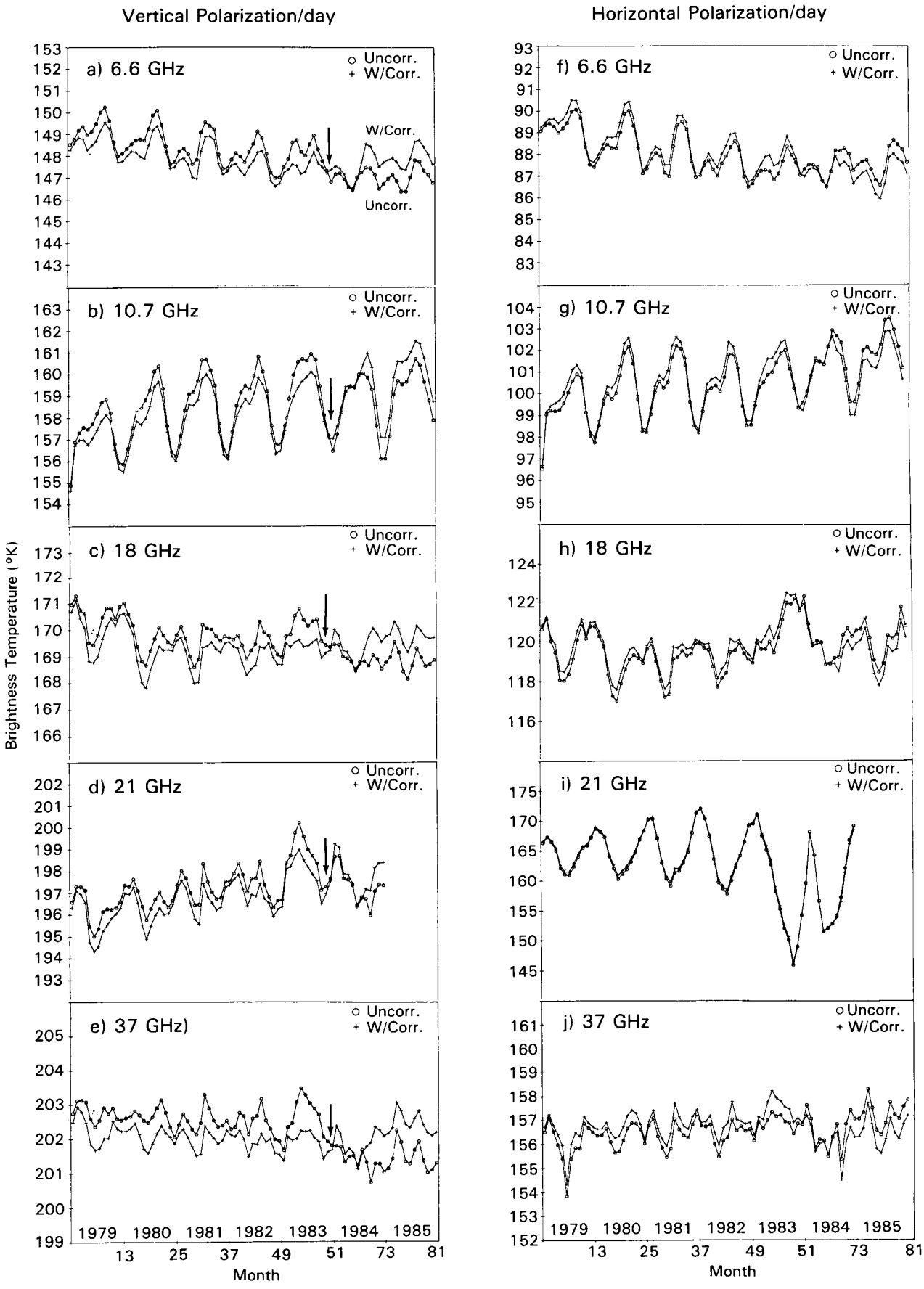

Figure 14. Time series of corrected and uncorrected T_B using day data only.

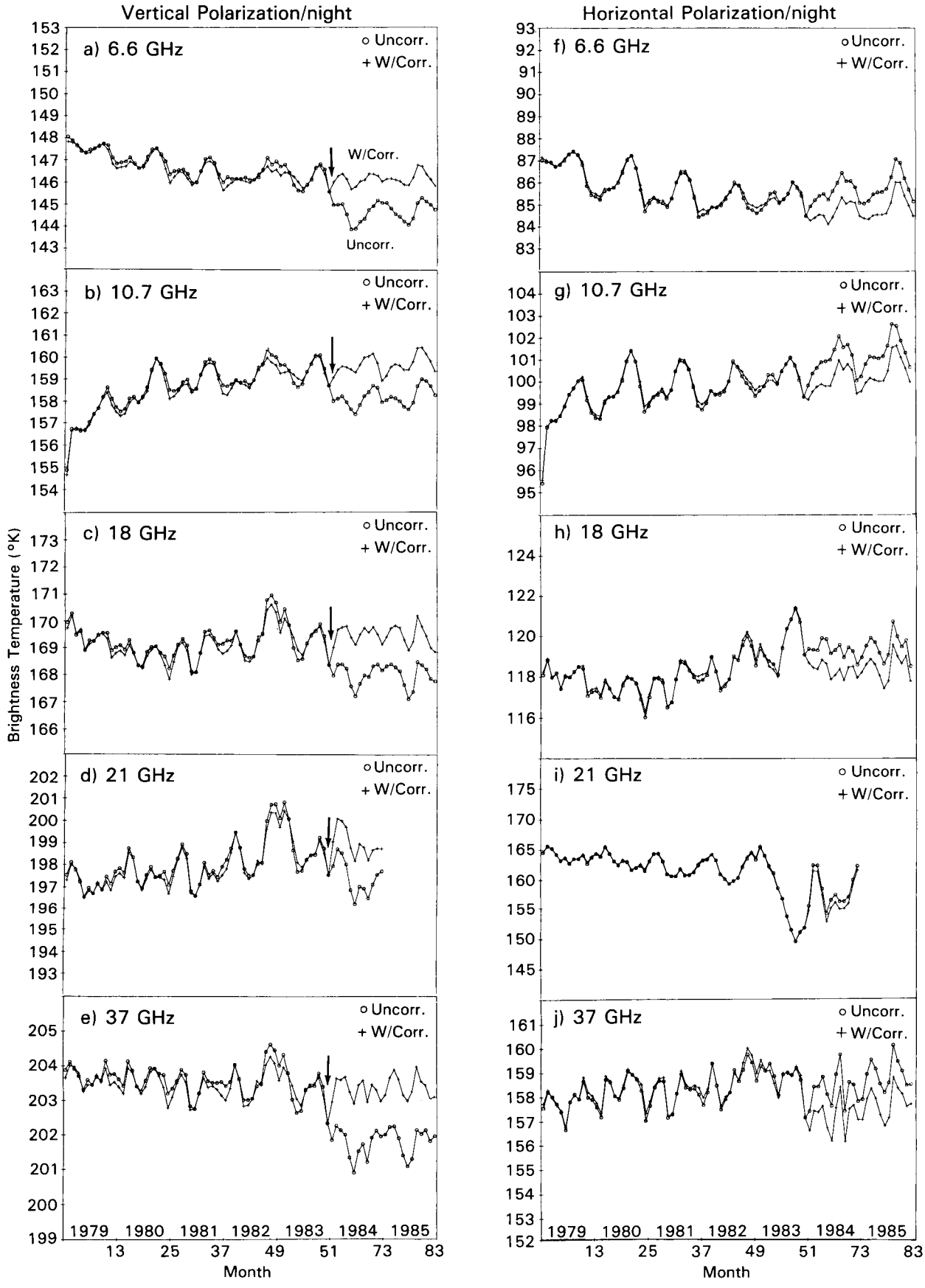

Figure 15. Time series of corrected and uncorrected T_B using night data only.

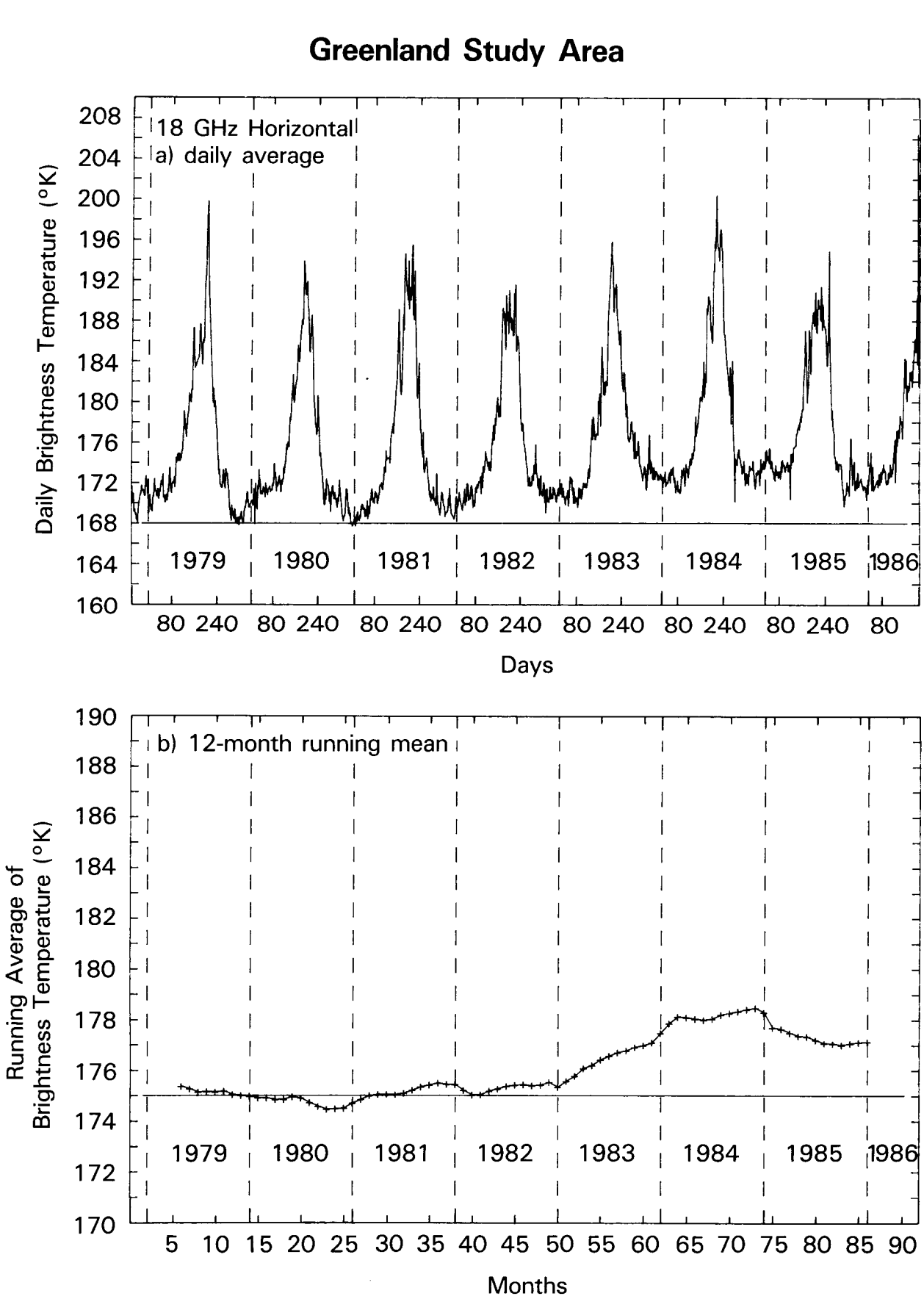

Figure 16. Time series of brightness temperature data over the Greenland ice sheets using (a) daily average values and (b) 12-month running averages.

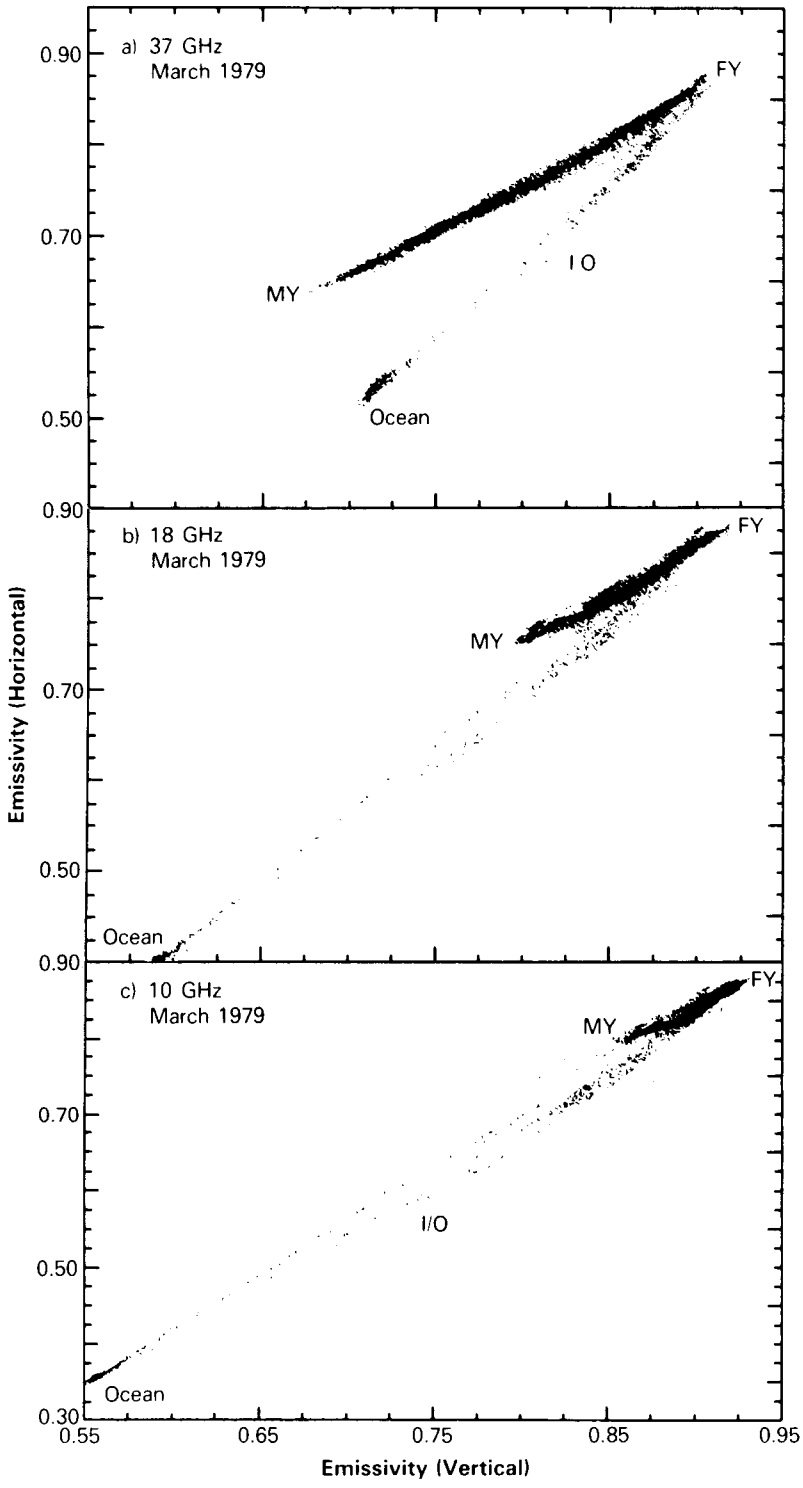

Figure 17. Scatter plot of 37H versus 37V over the Central Arctic region.

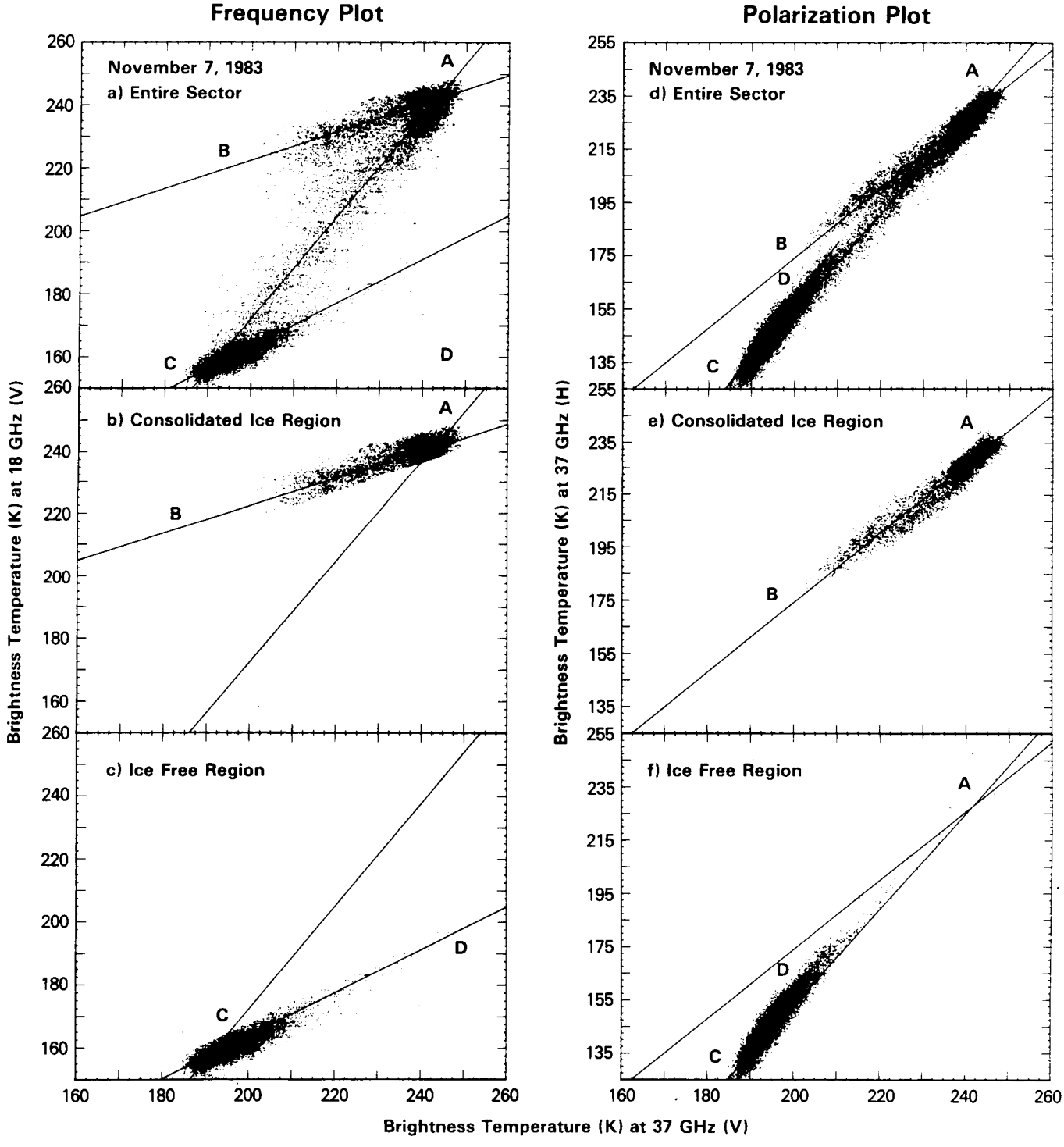

Figure 18. Scatter plot of 18V versus 37V over the Weddell Sea region.

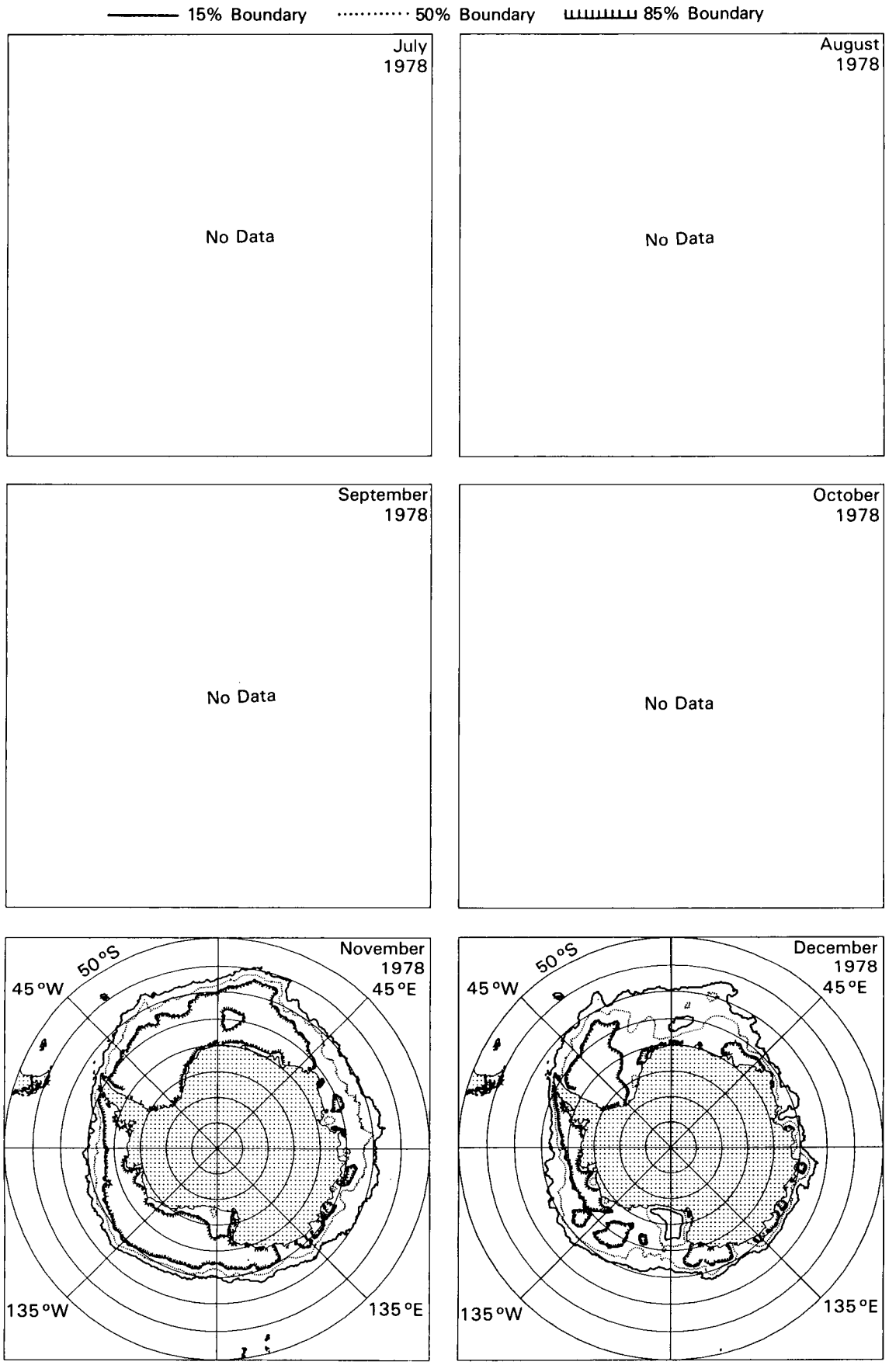

Figure 19. Antarctic monthly ice concentration contours for November to December 1978

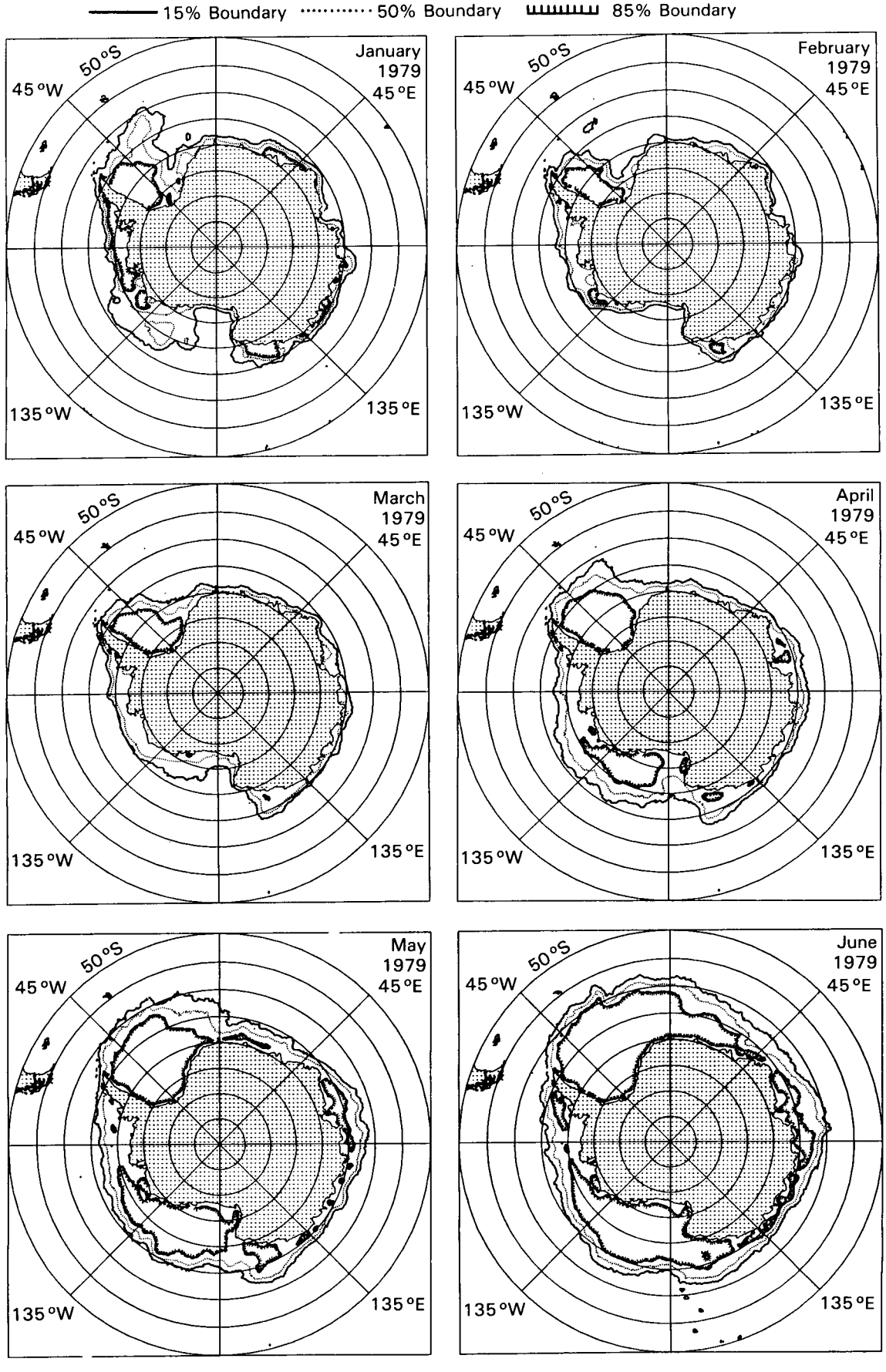

Figure 20. Antarctic monthly ice concentration contours for January to June 1979

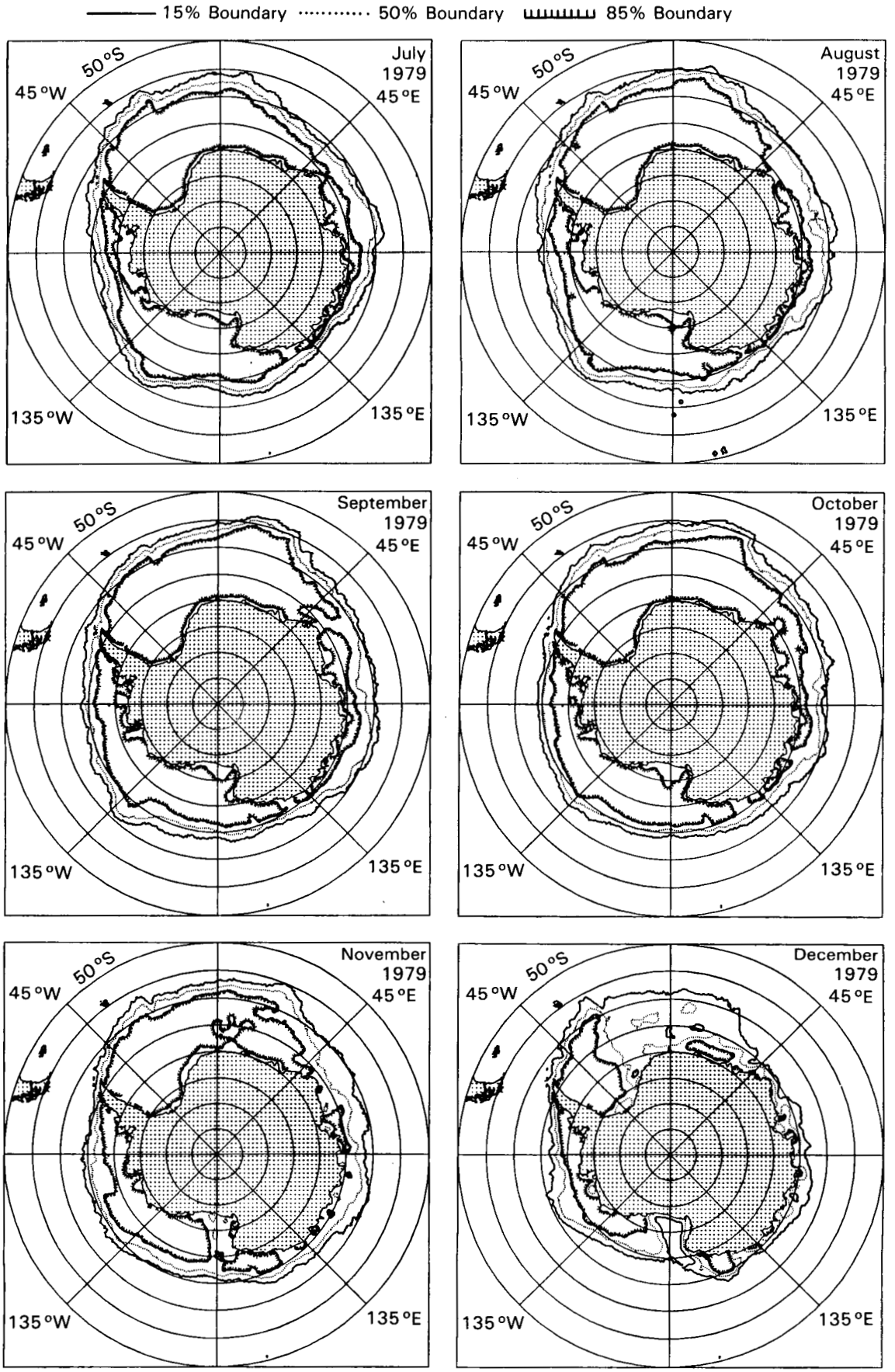

Figure 21. Antarctic monthly ice concentration contours for July to December 1979

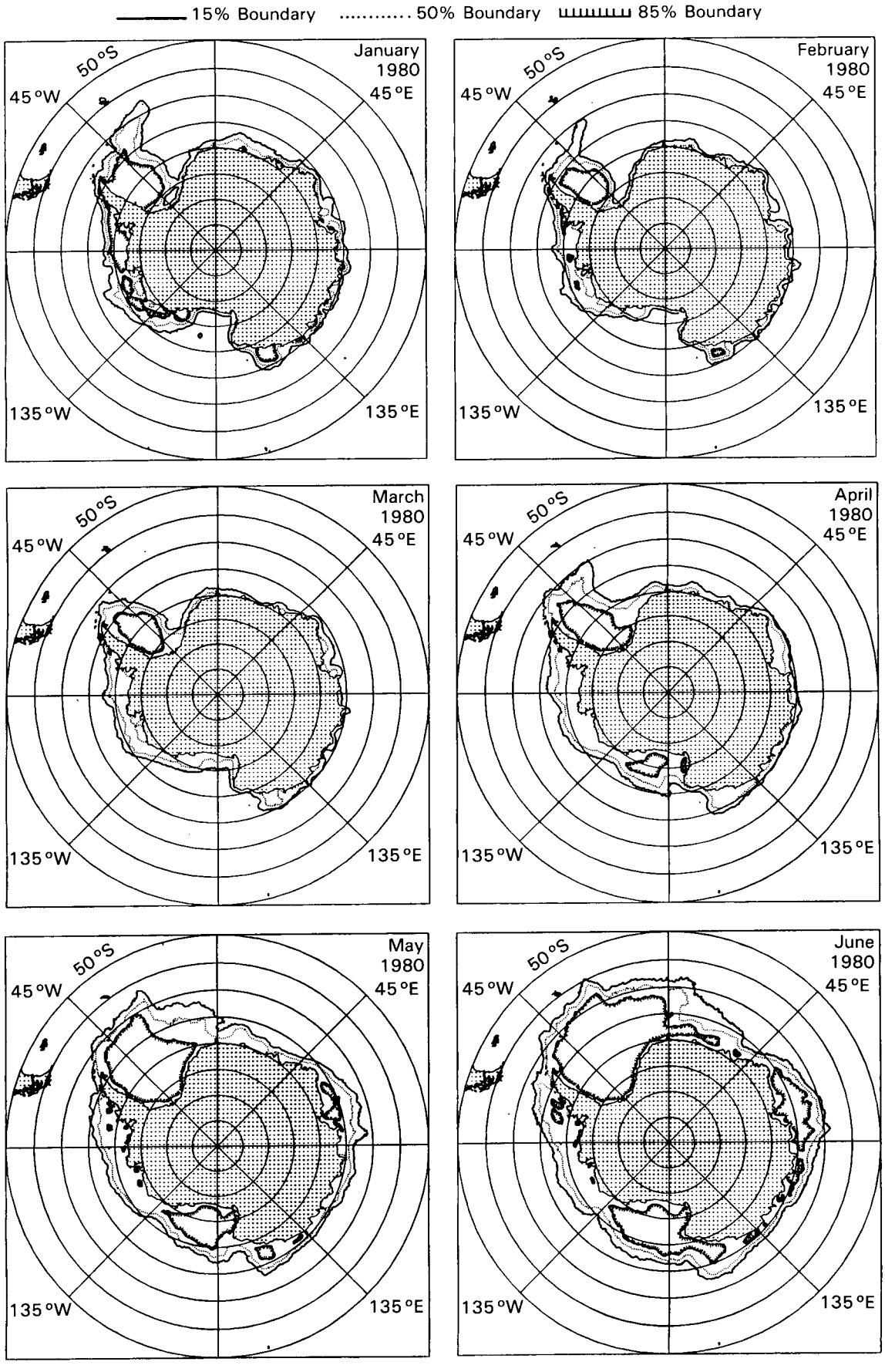

Figure 22. Antarctic monthly ice concentration contours for January to June 1980

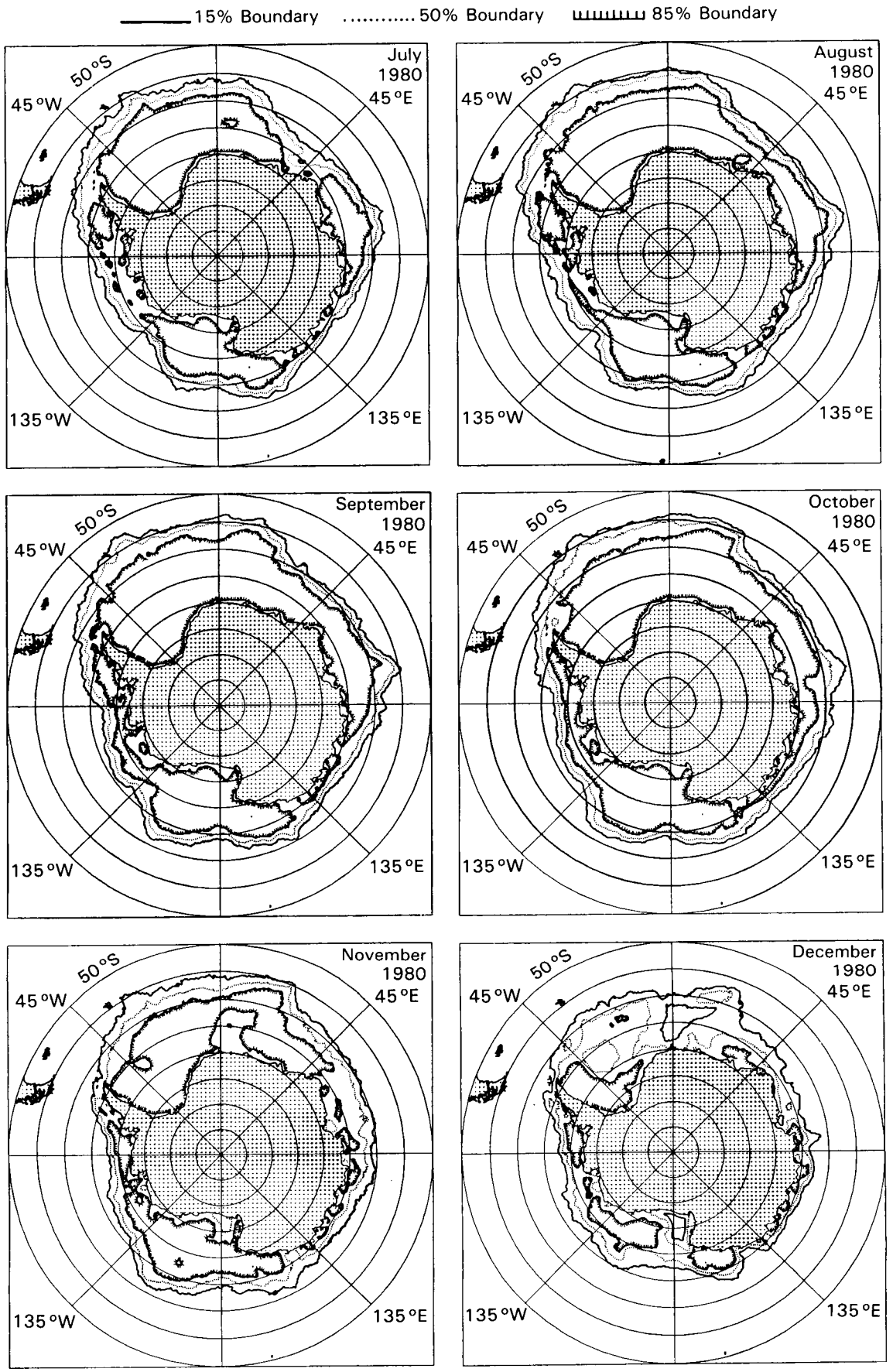

Figure 23. Antarctic monthly ice concentration contours for July to December 1980

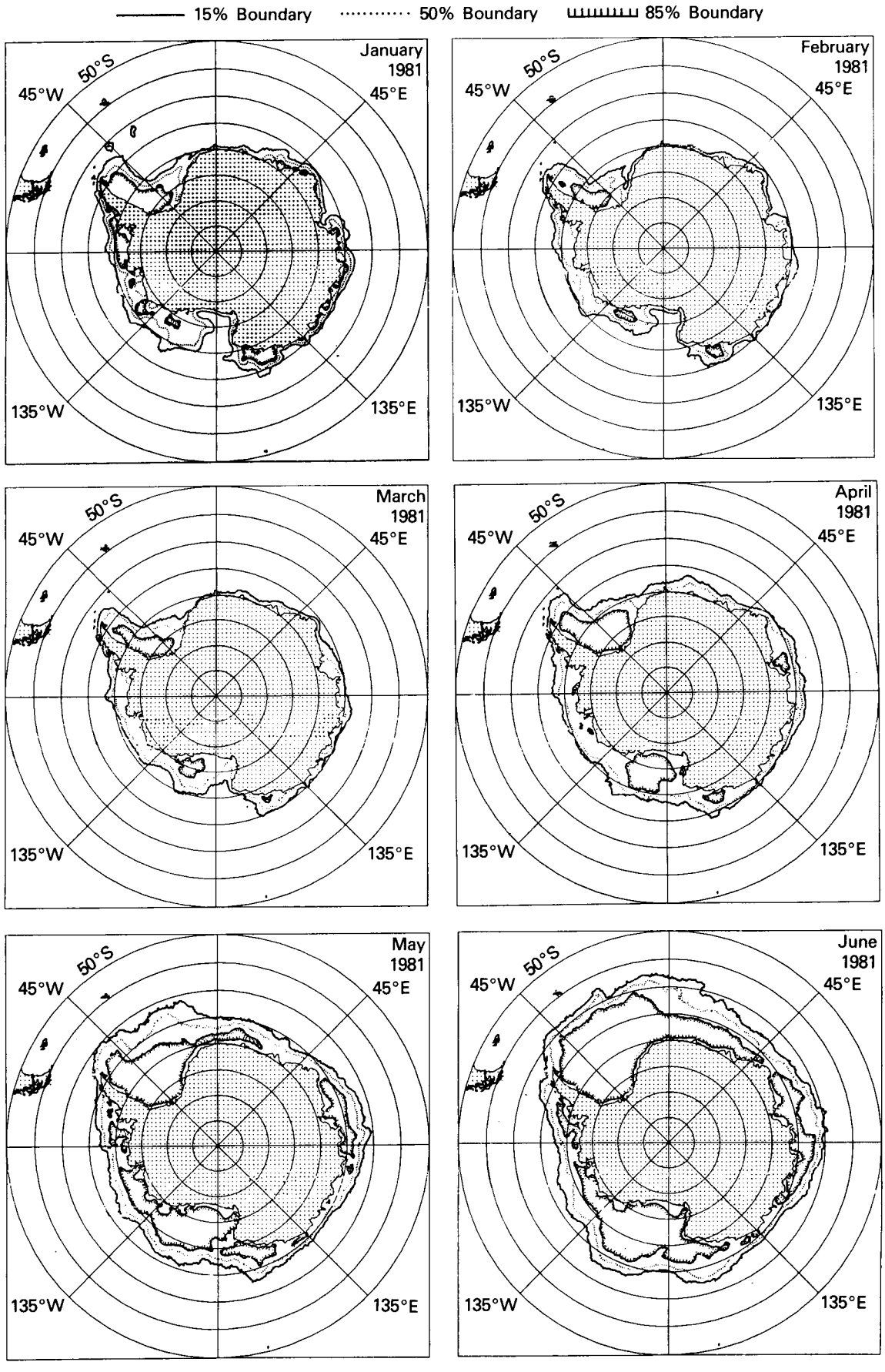

Figure 24. Antarctic monthly ice concentration contours for January to June 1981

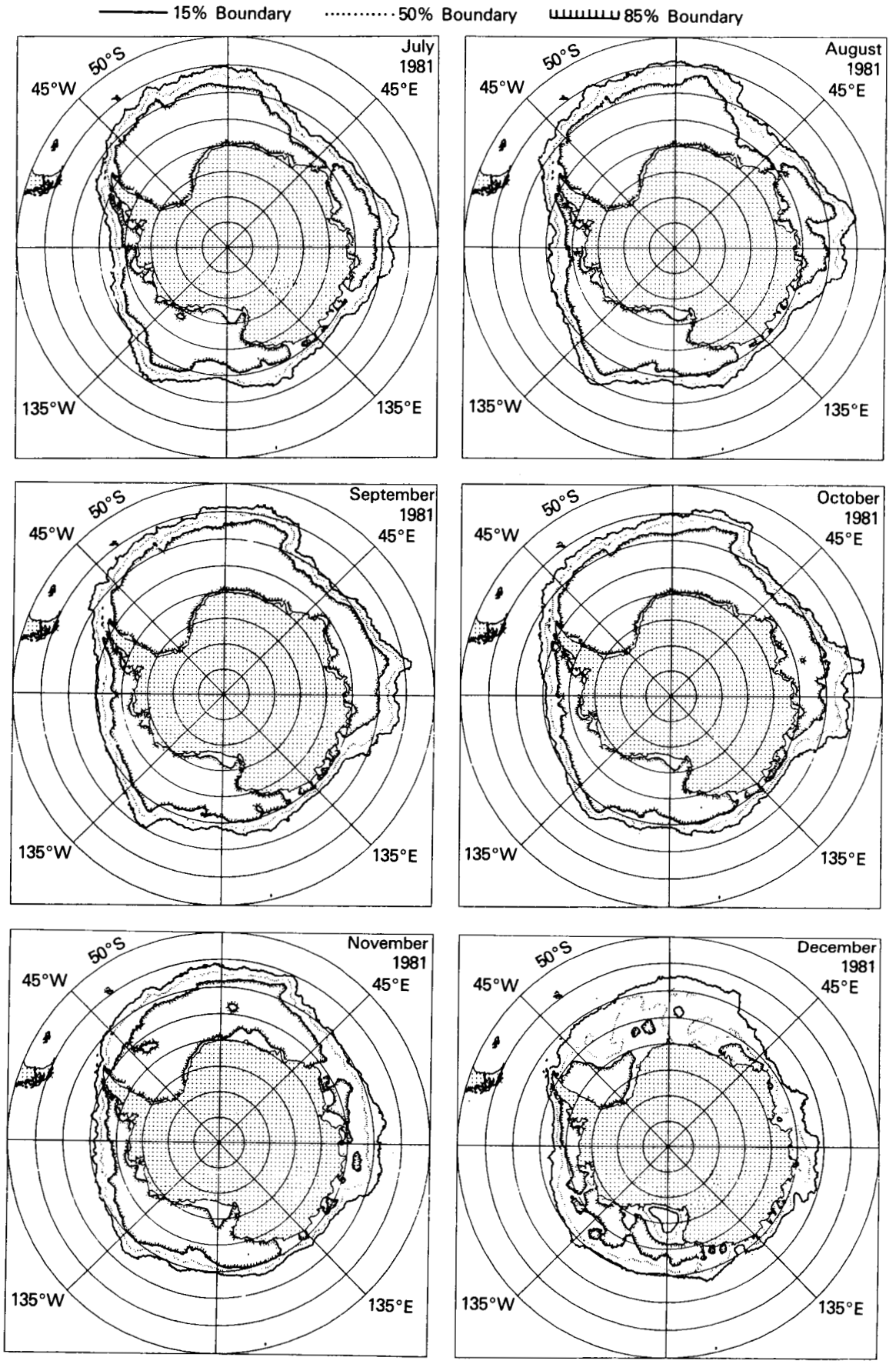

Figure 25. Antarctic monthly ice concentration contours for July to December 1981

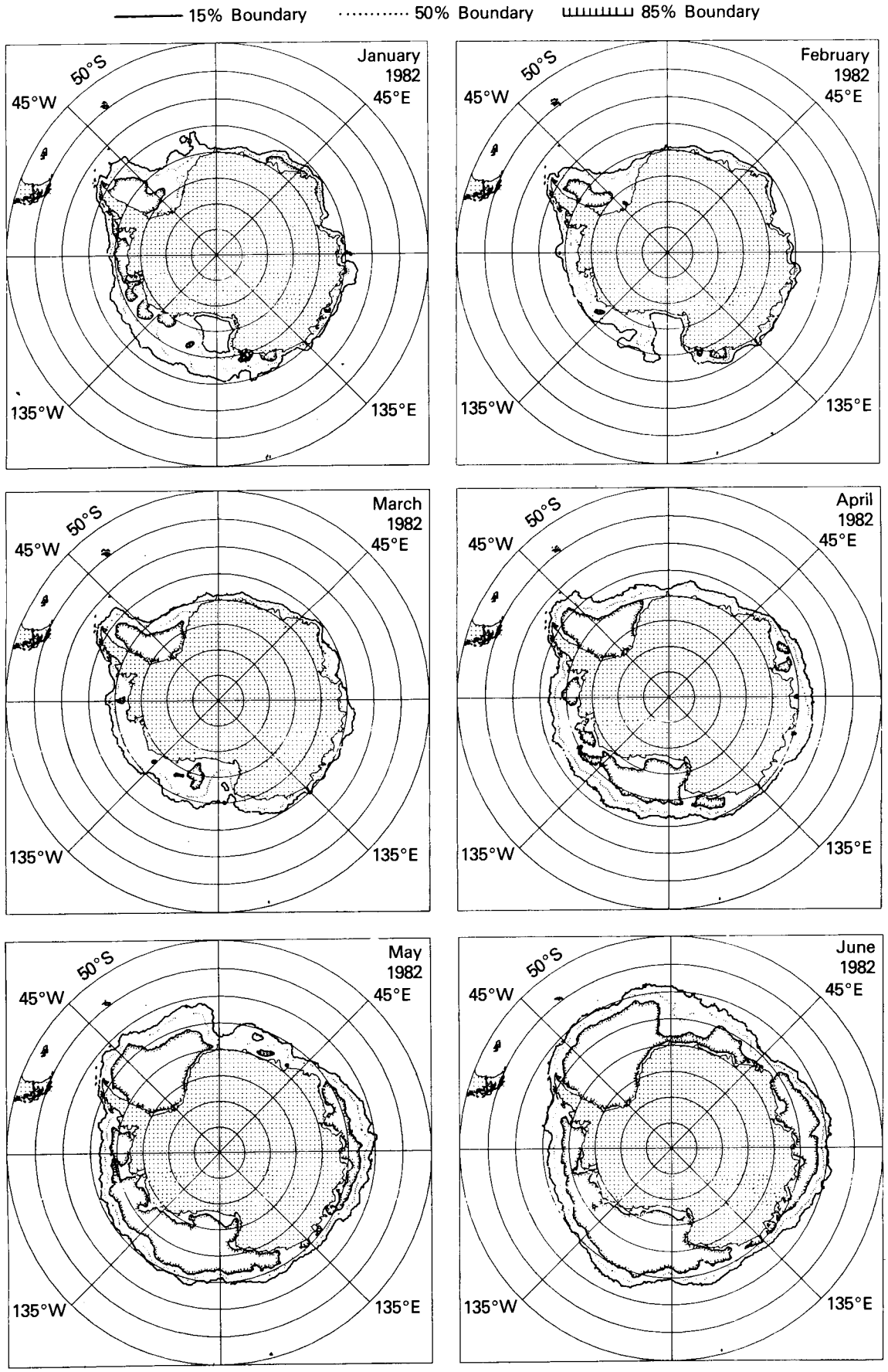

Figure 26. Antarctic monthly ice concentration contours for January to June 1982

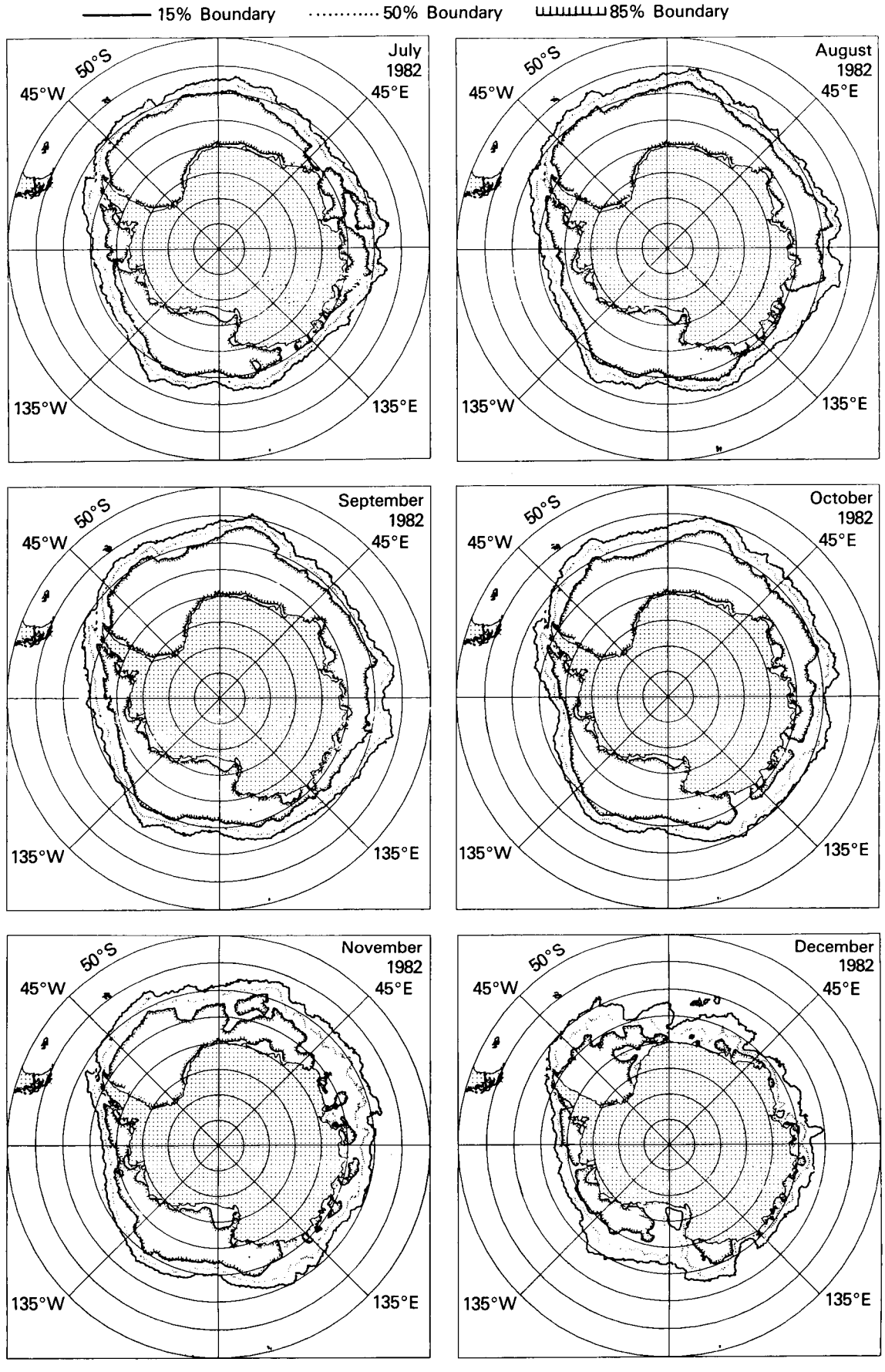

Figure 27. Antarctic monthly ice concentration contours for July to December 1982

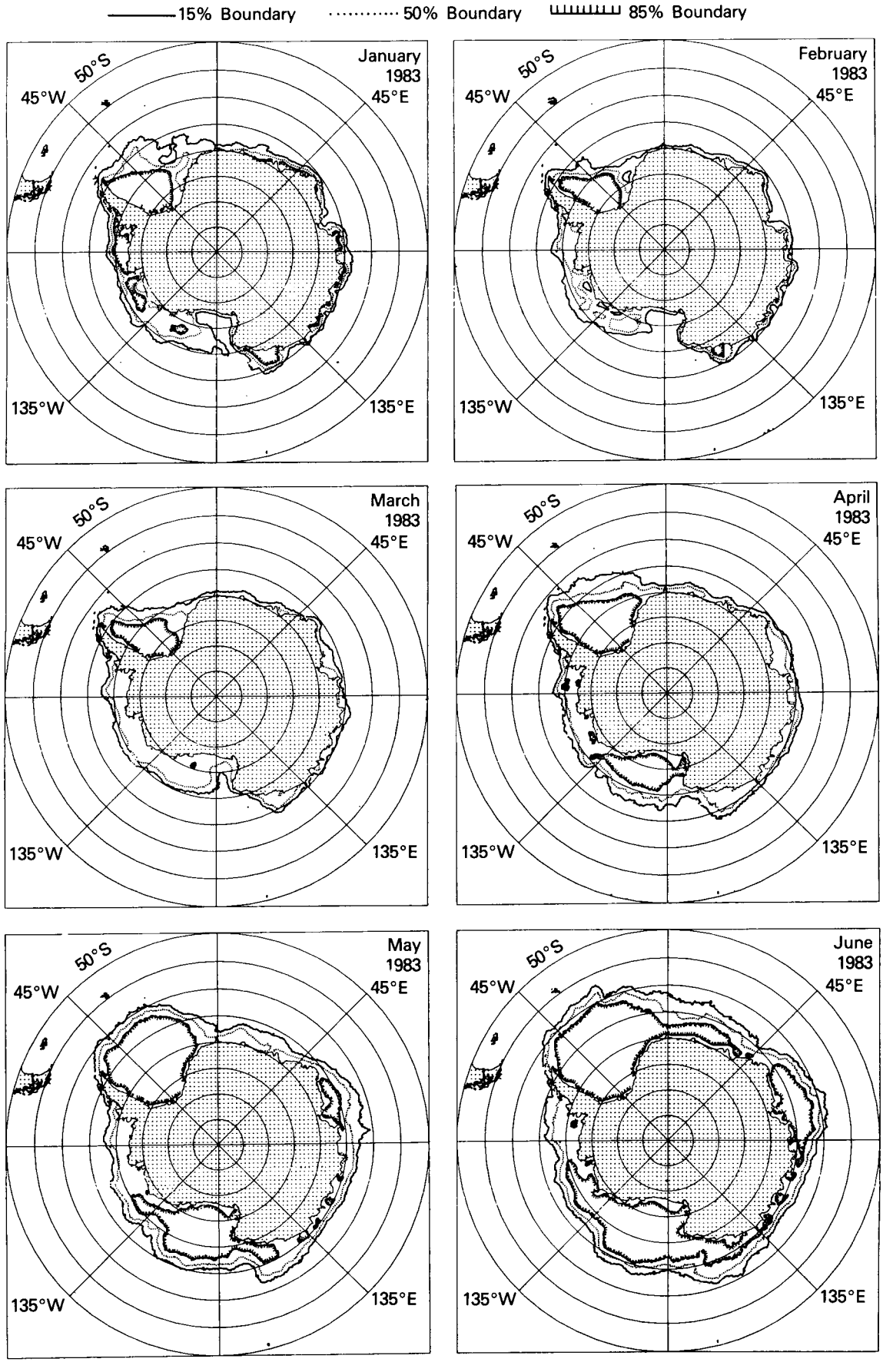

Figure 28. Antarctic monthly ice concentration contours for January to June 1983

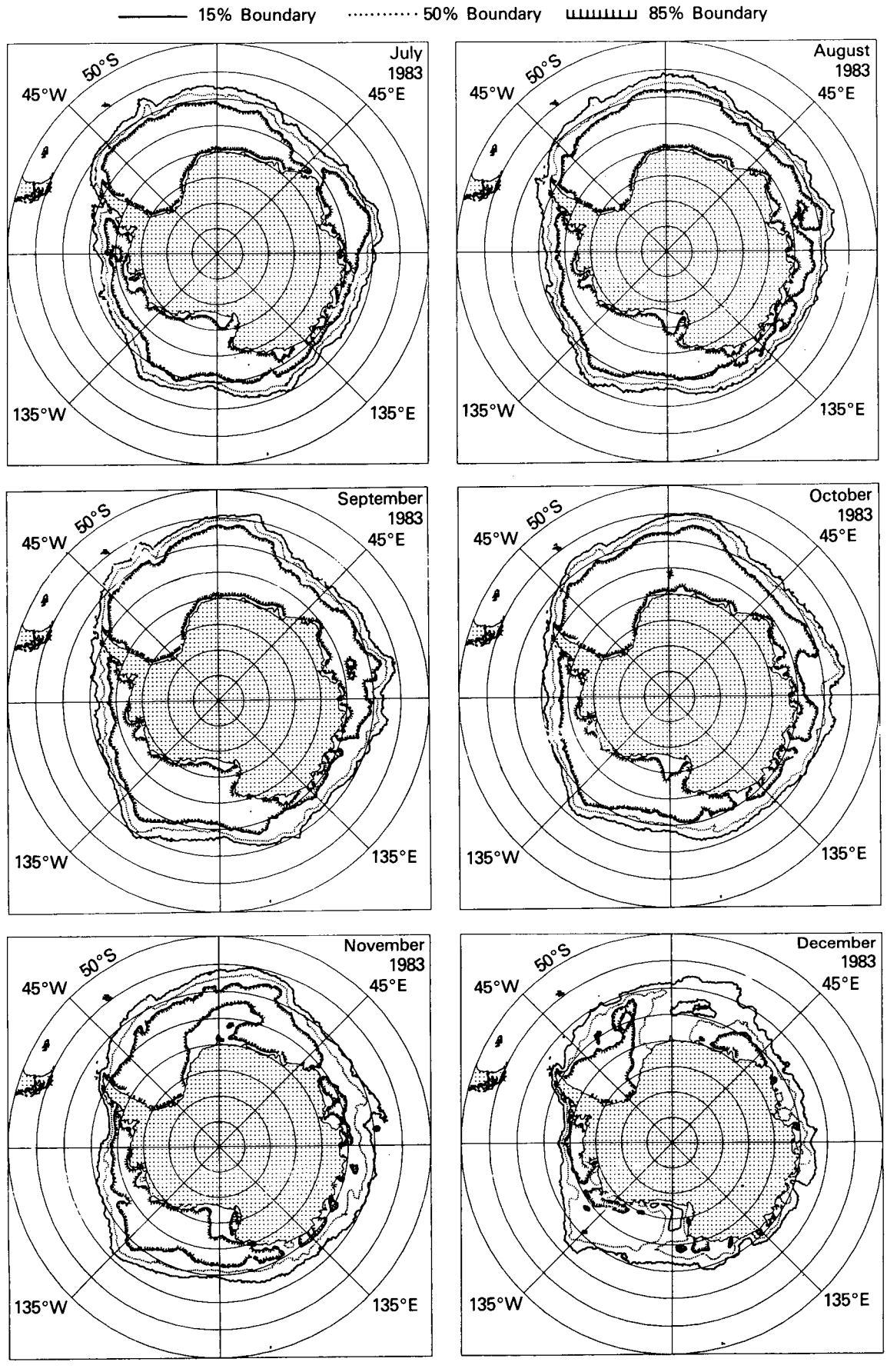

Figure 29. Antarctic monthly ice concentration contours for July to December 1983

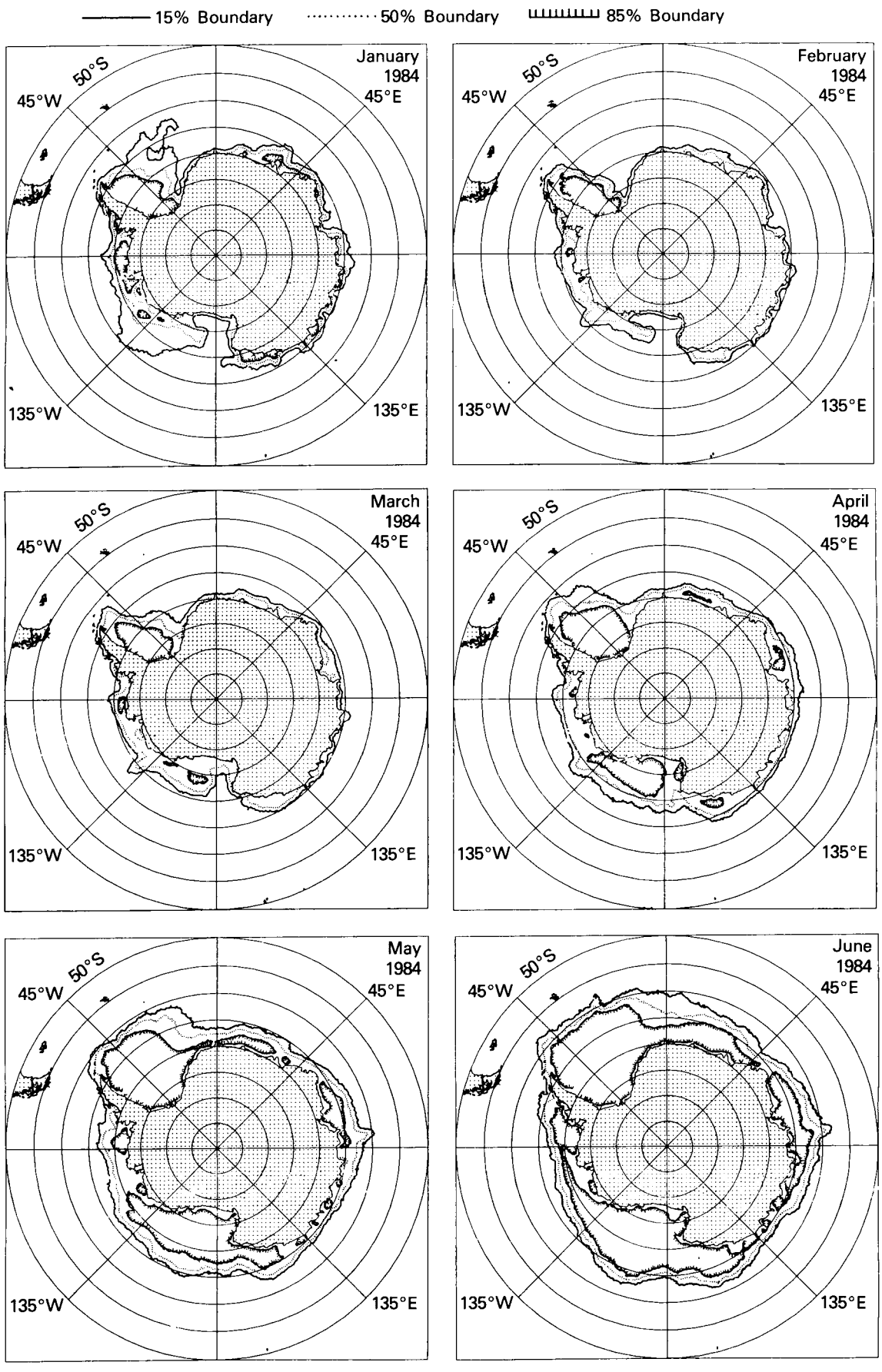

Figure 30. Antarctic monthly ice concentration contours for January to June 1984

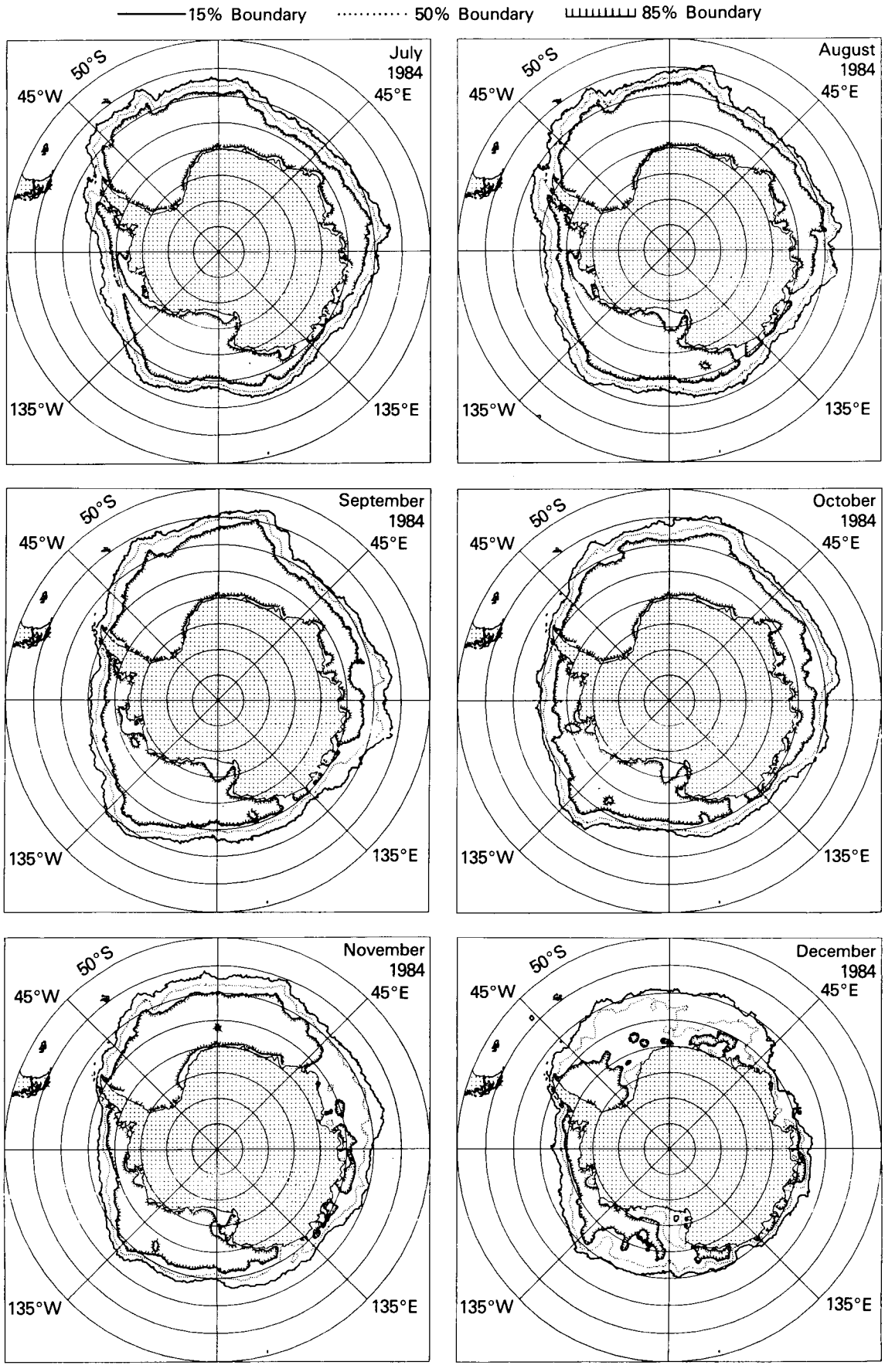

Figure 31. Antarctic monthly ice concentration contours for July to December 1984

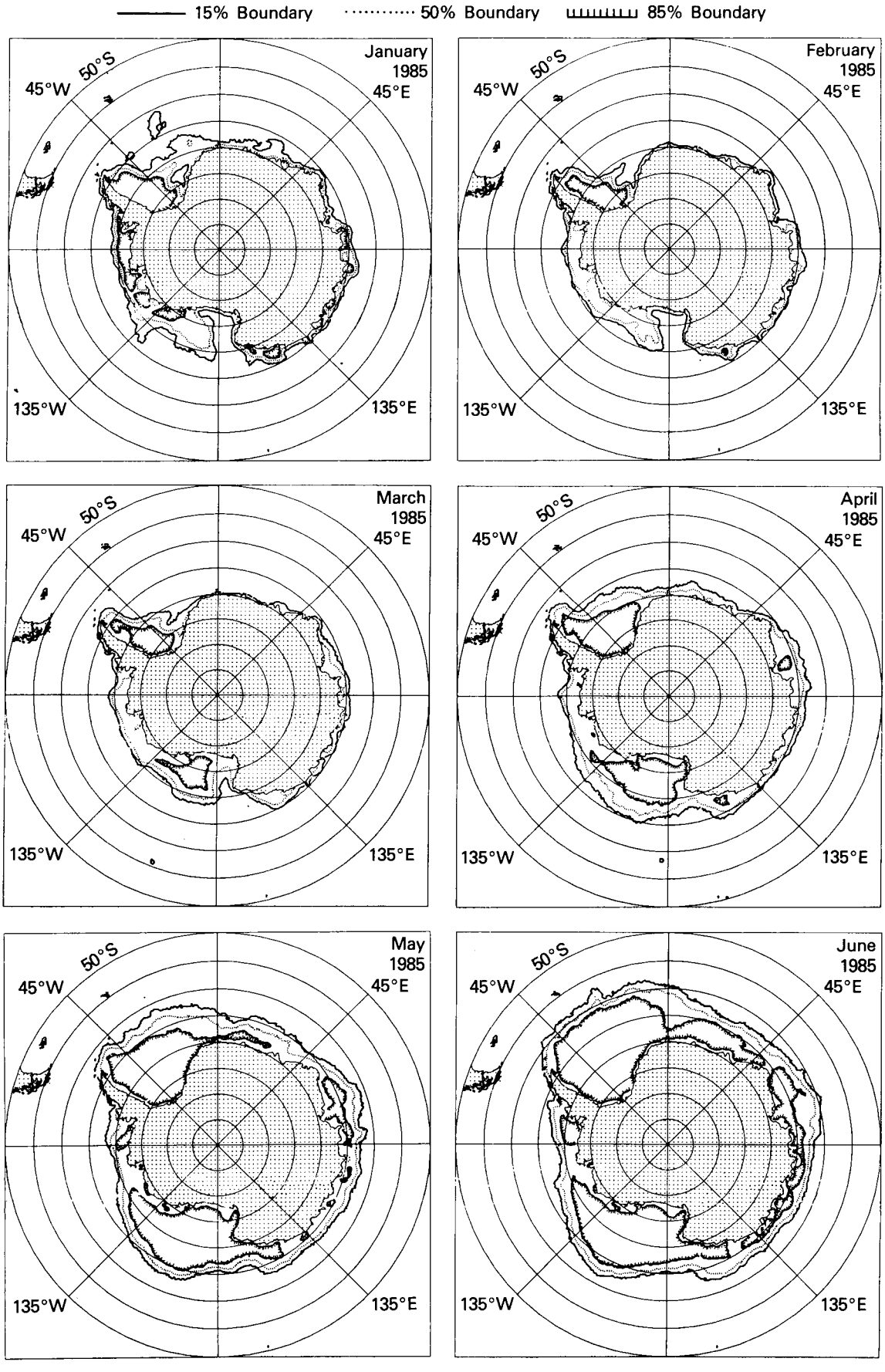

Figure 32. Antarctic monthly ice concentration contours for January to June 1985

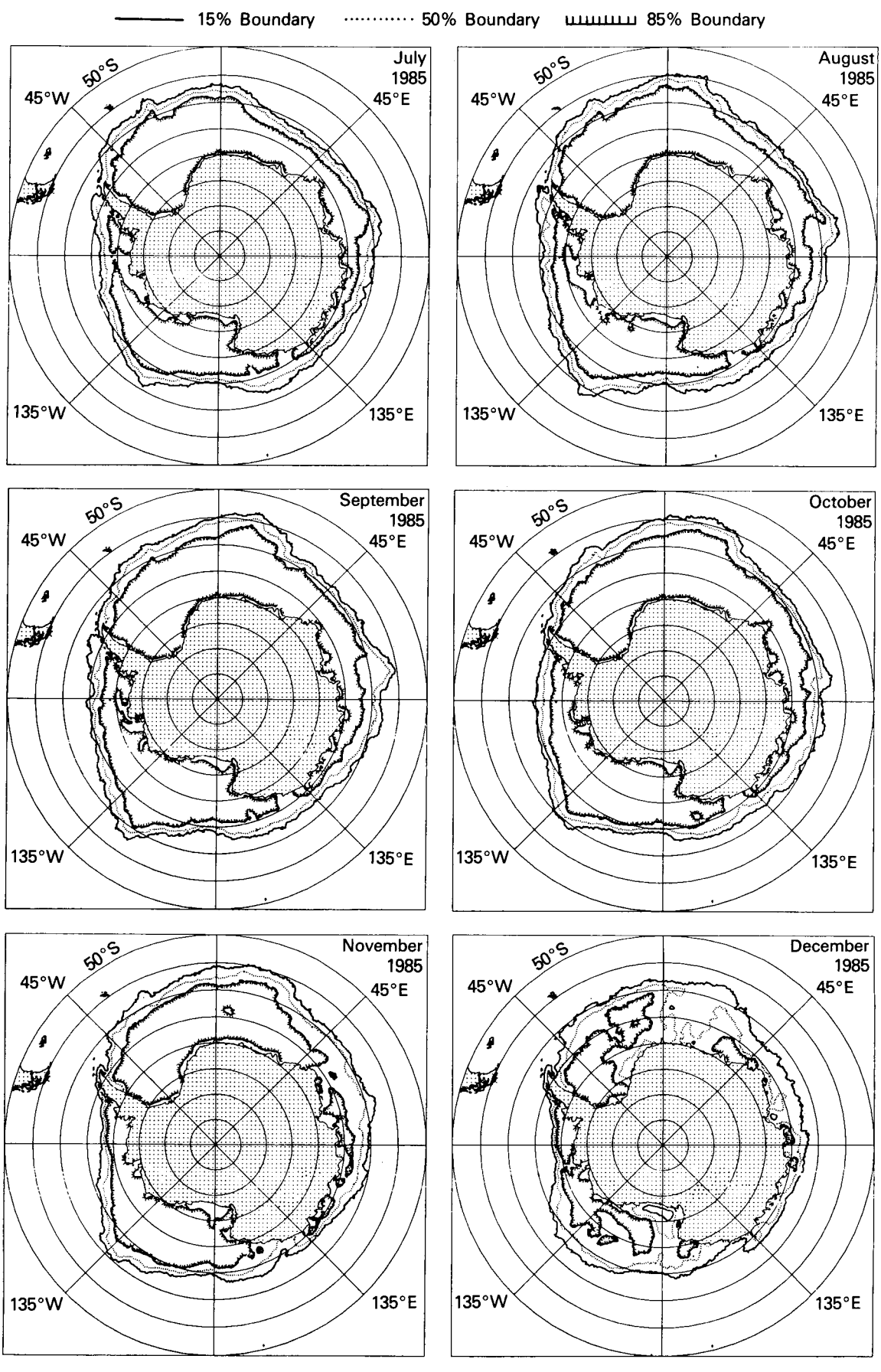

Figure 33. Antarctic monthly ice concentration contours for July to December 1985

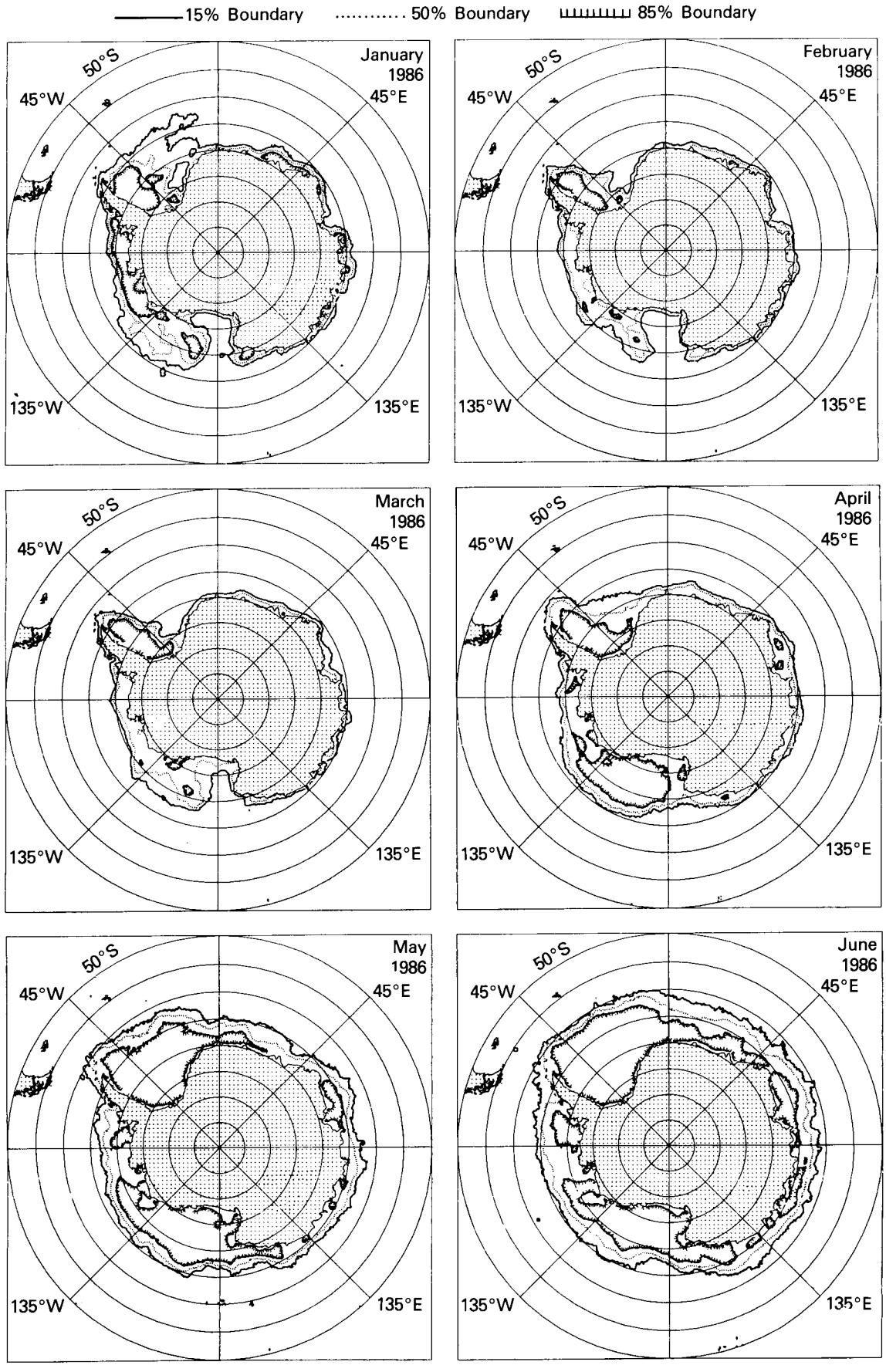

Figure 34. Antarctic monthly ice concentration contours for January to June 1986

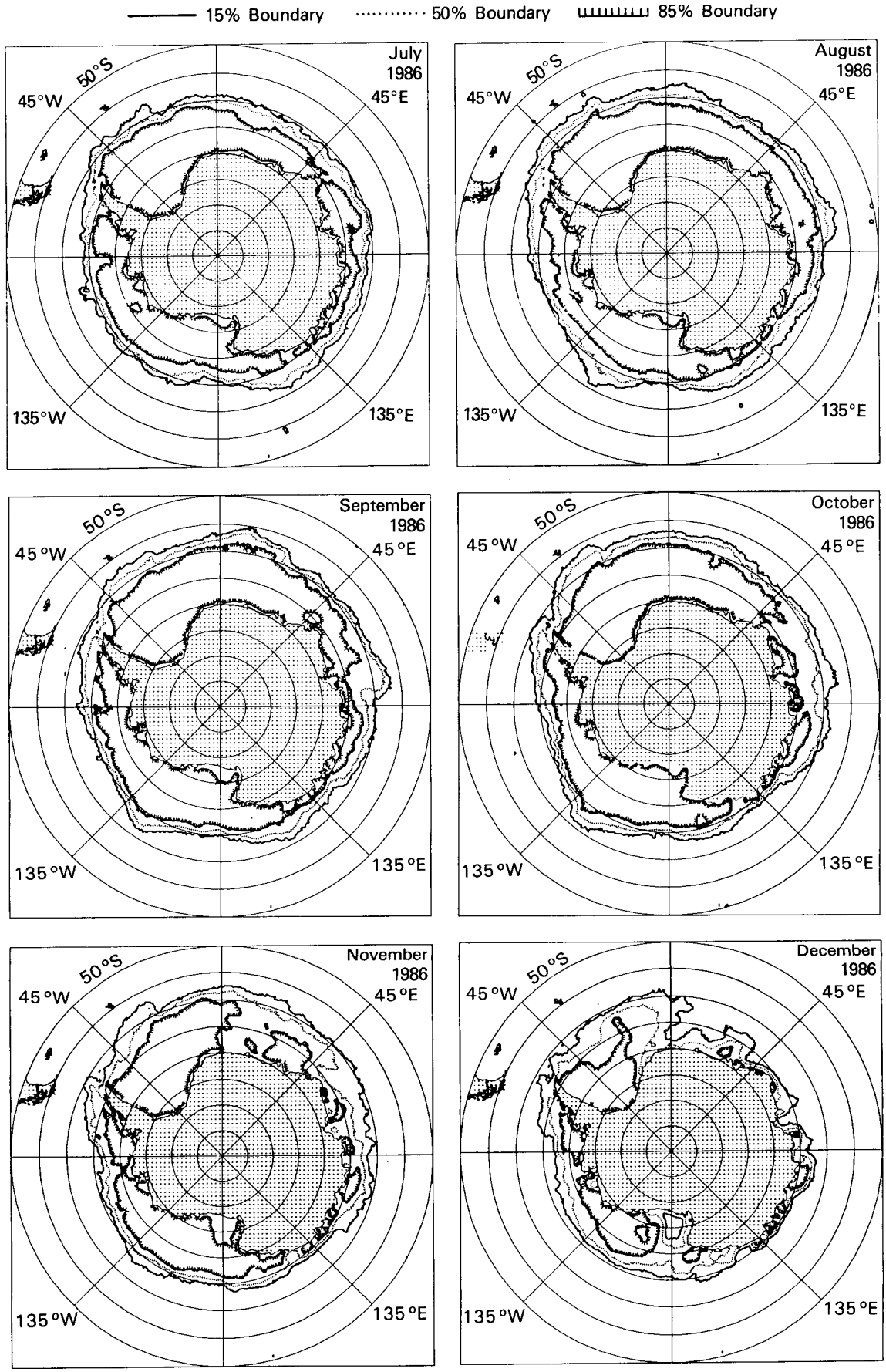

Figure 35. Antarctic monthly ice concentration contours for July to December 1986

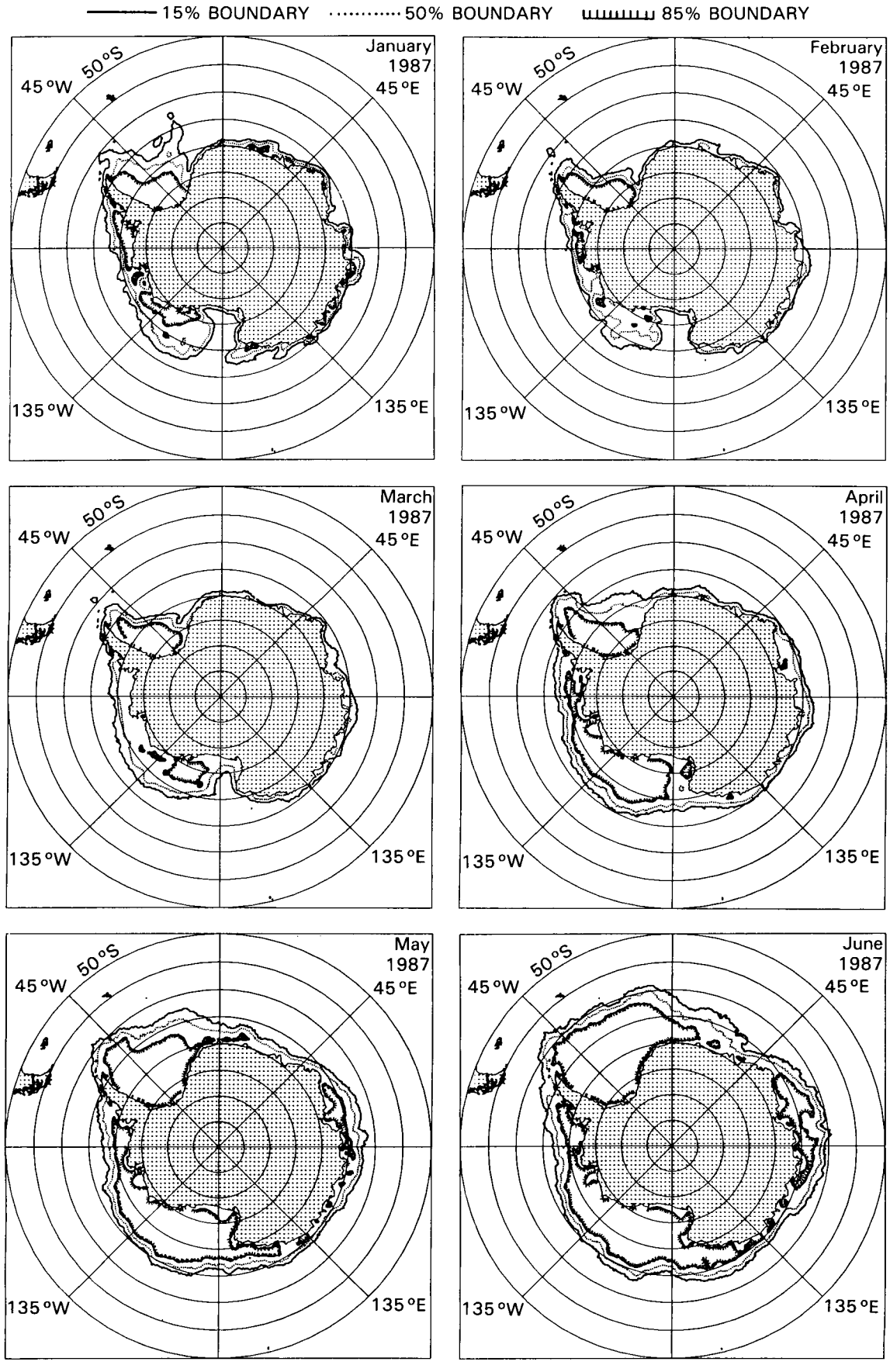

Figure 36. Antarctic monthly ice concentration contours for January to June 1987

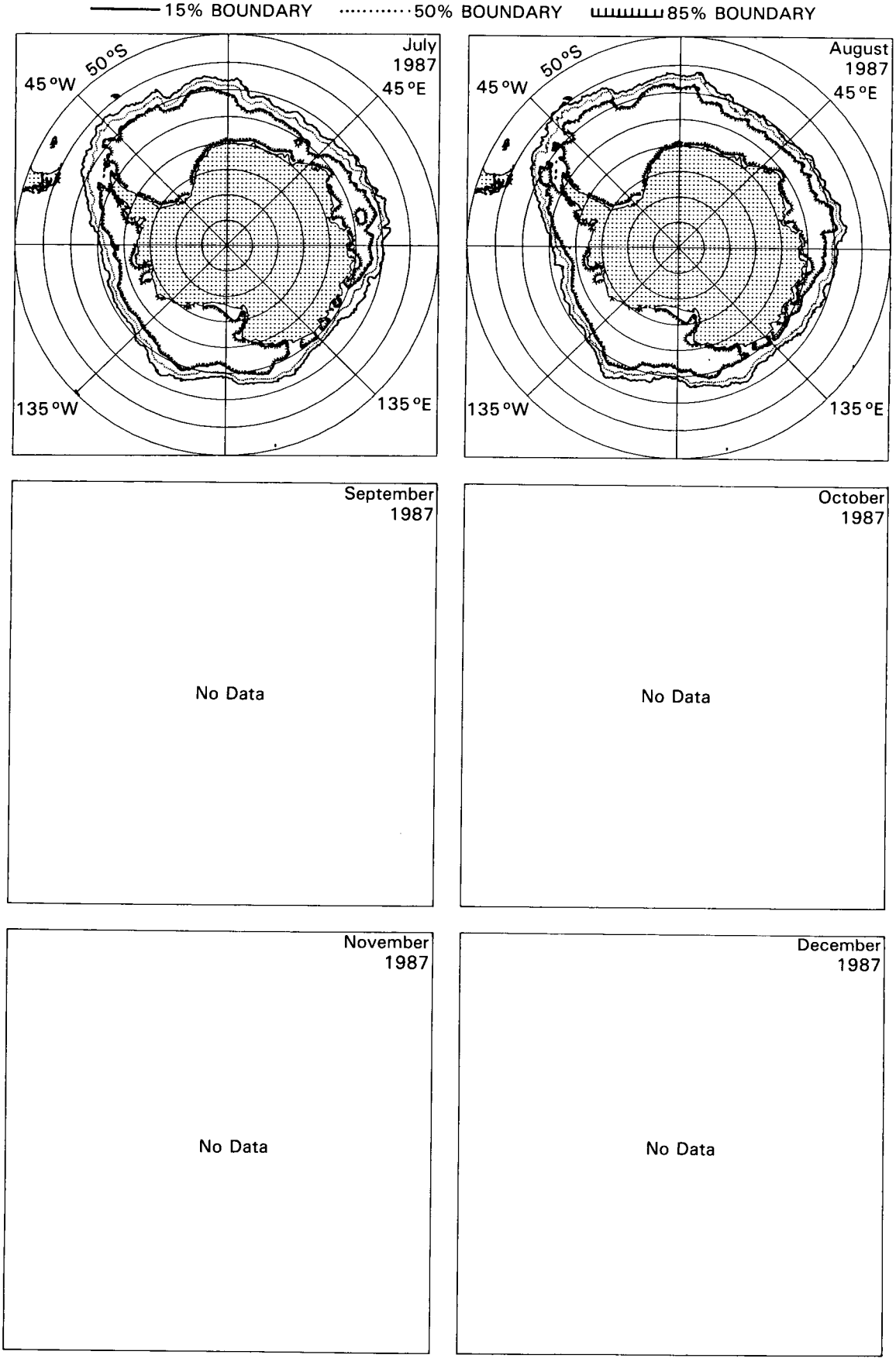

Figure 37. Antarctic monthly ice concentration contours for July to August 1987

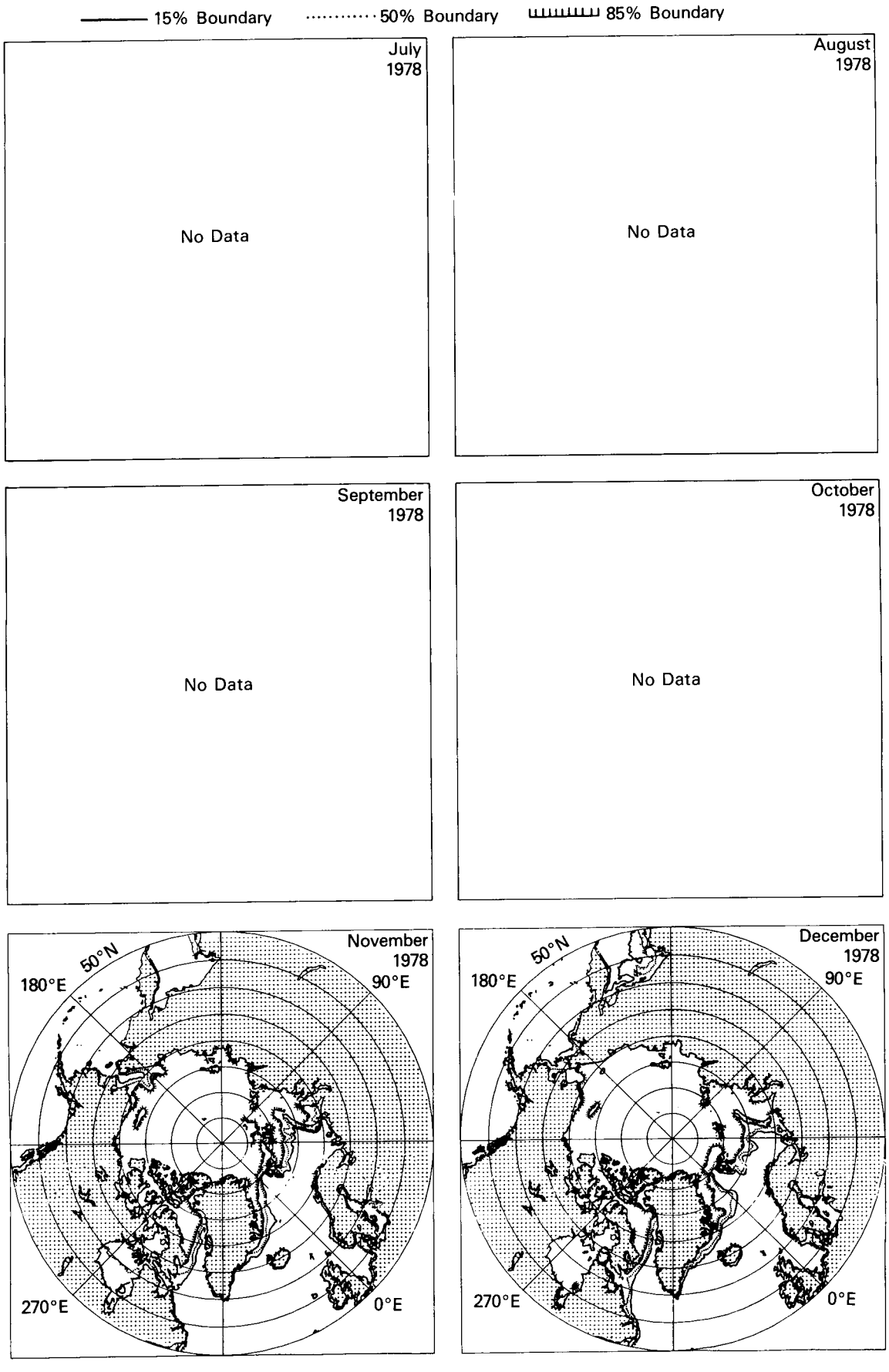

Figure 38. Arctic monthly ice concentration contours for November to December 1978

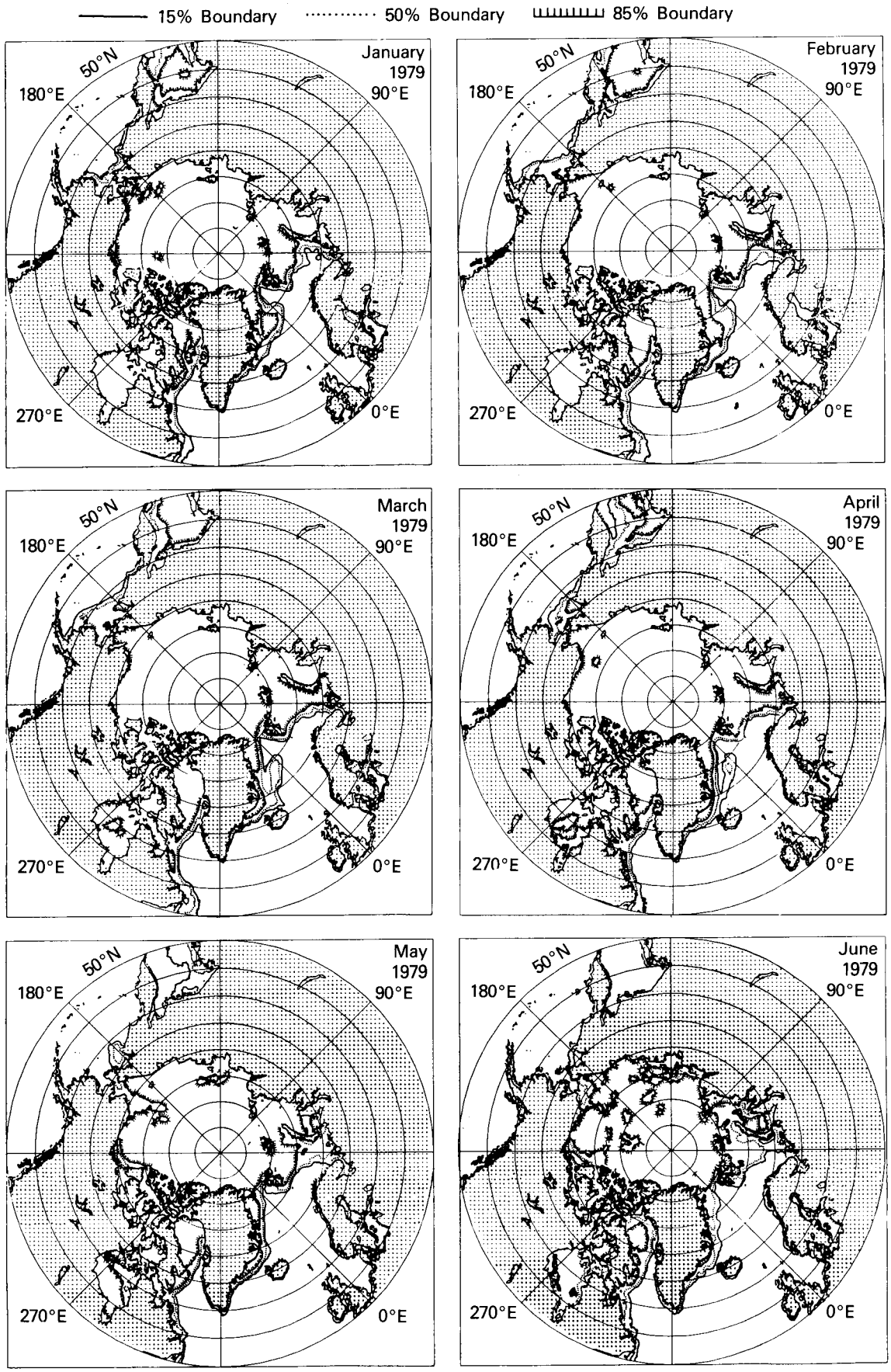

Figure 39. Arctic monthly ice concentration contours for January to June 1979

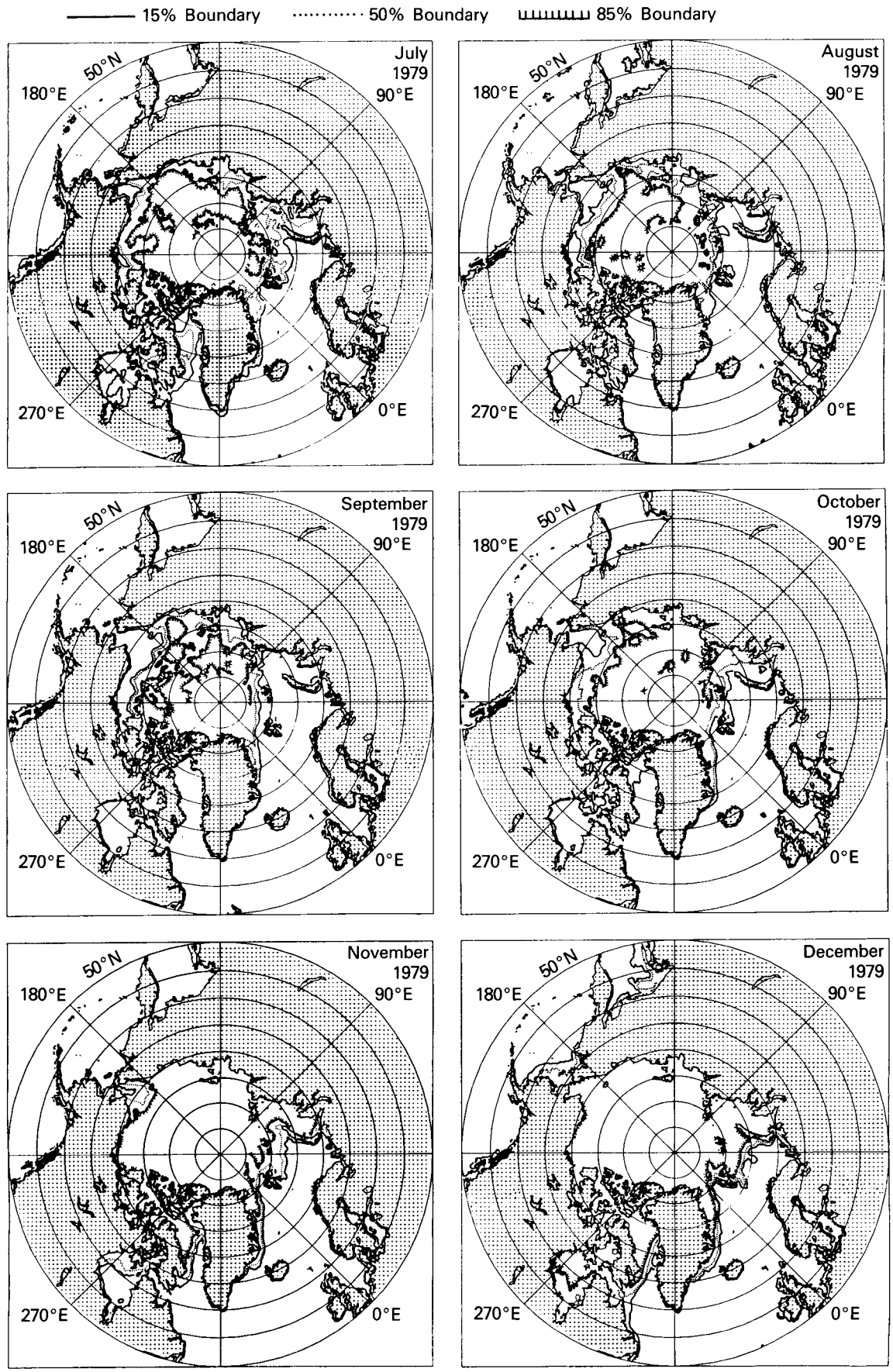

Figure 40. Arctic monthly ice concentration contours for July to December 1979

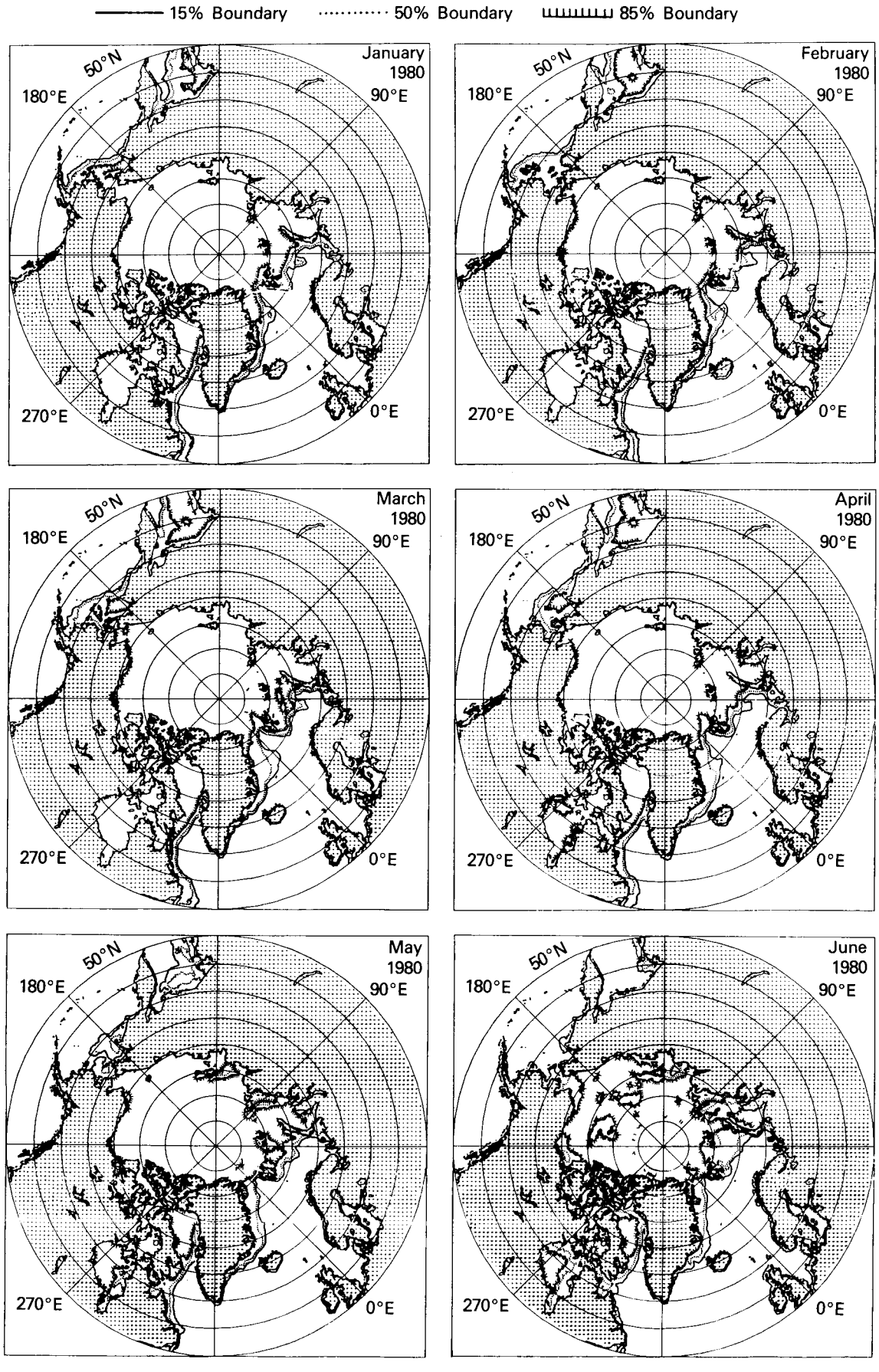

Figure 41. Arctic monthly ice concentration contours for January to June 1980

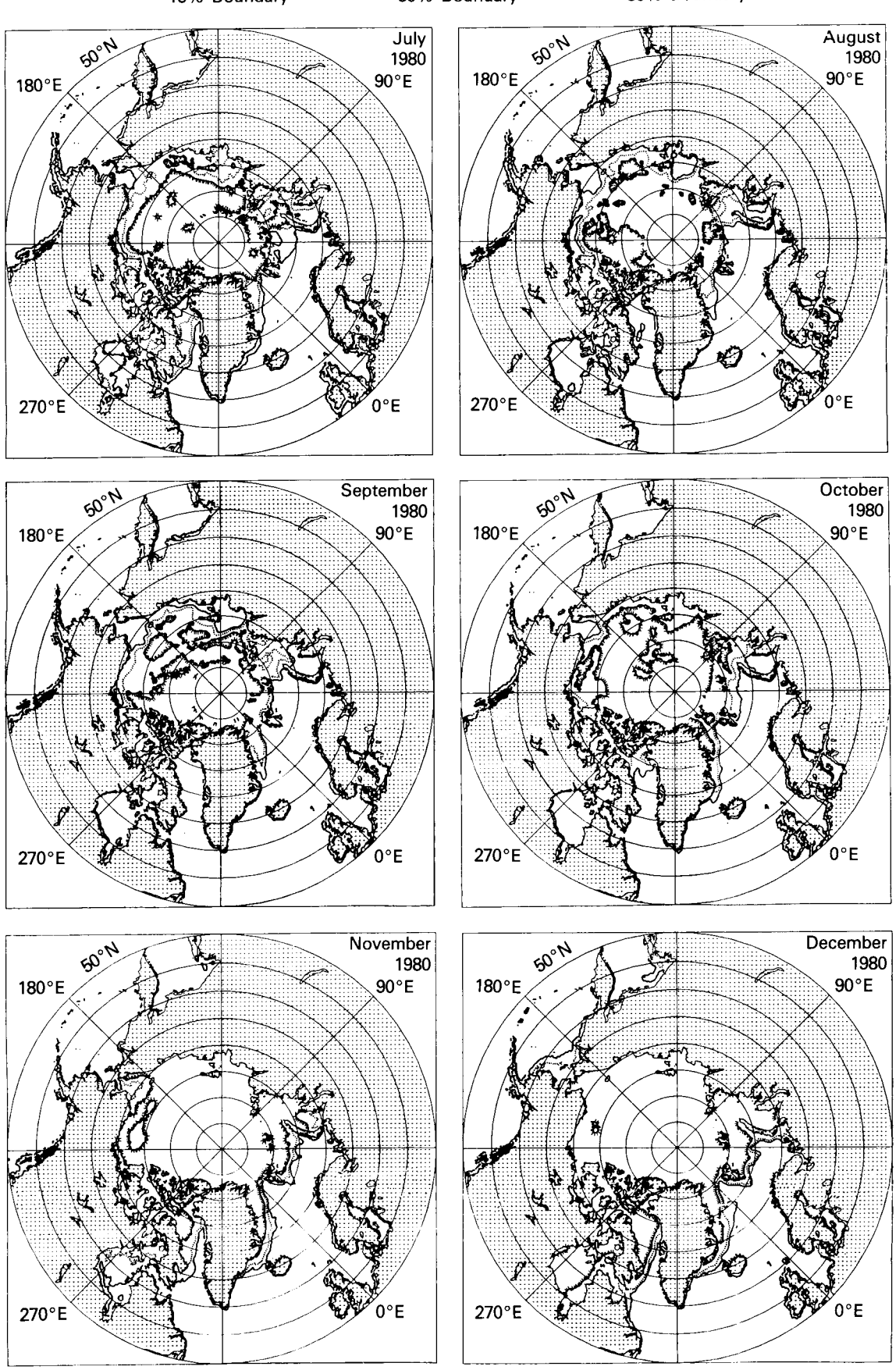

Figure 42. Arctic monthly ice concentration contours for July to December 1980

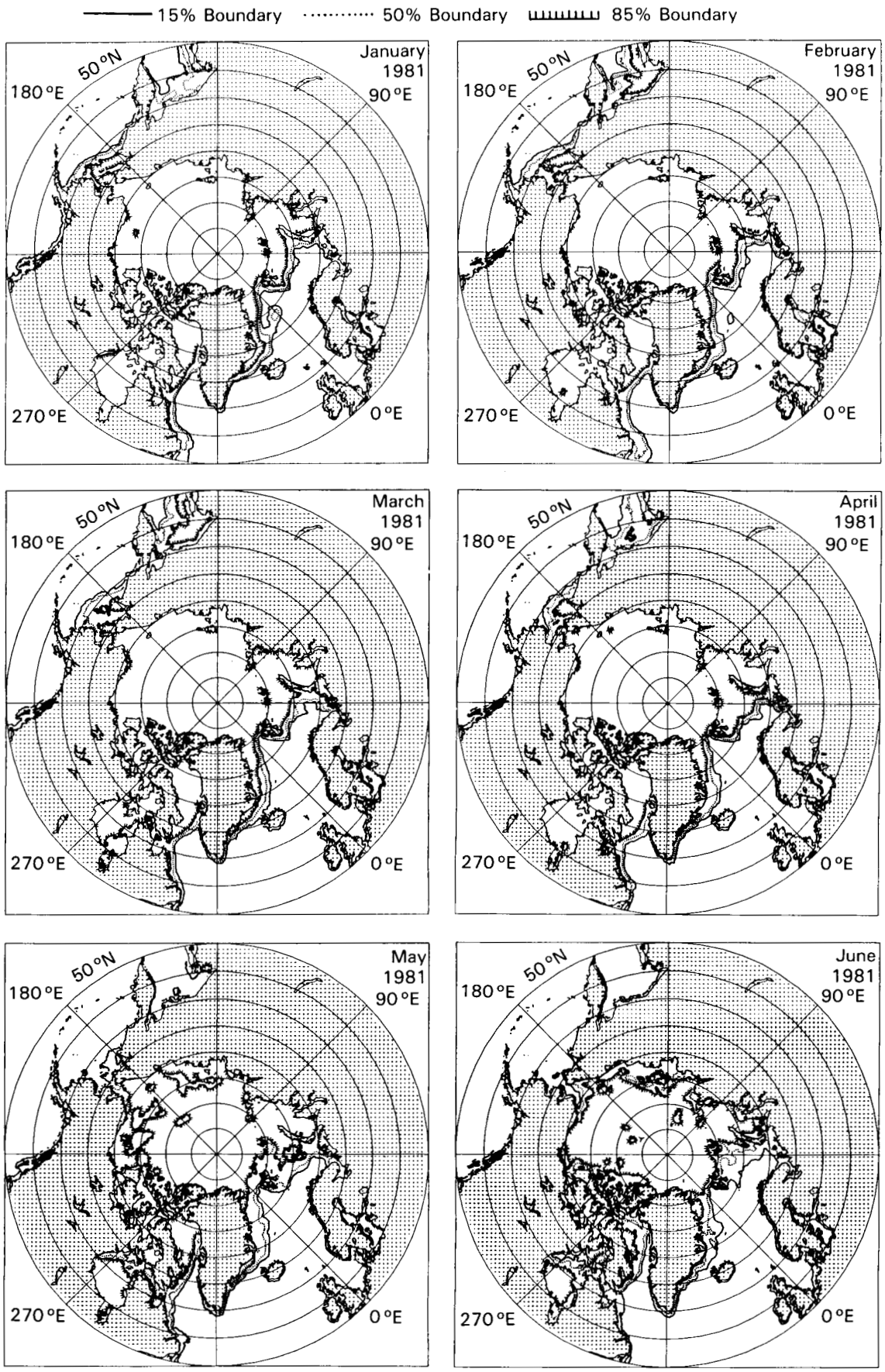

Figure 43. Arctic monthly ice concentration contours for January to June 1981

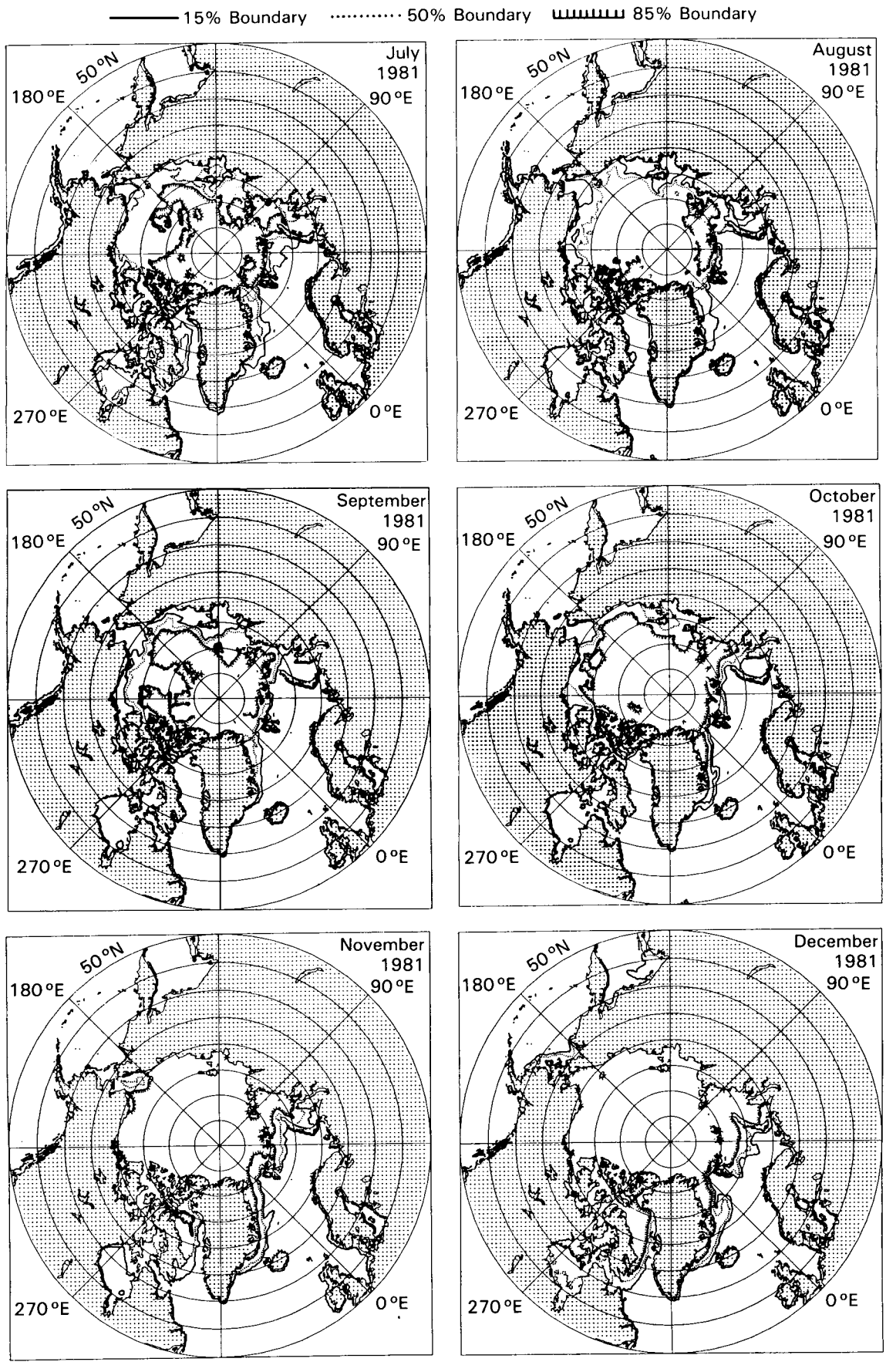

Figure 44. Arctic monthly ice concentration contours for July to December 1981

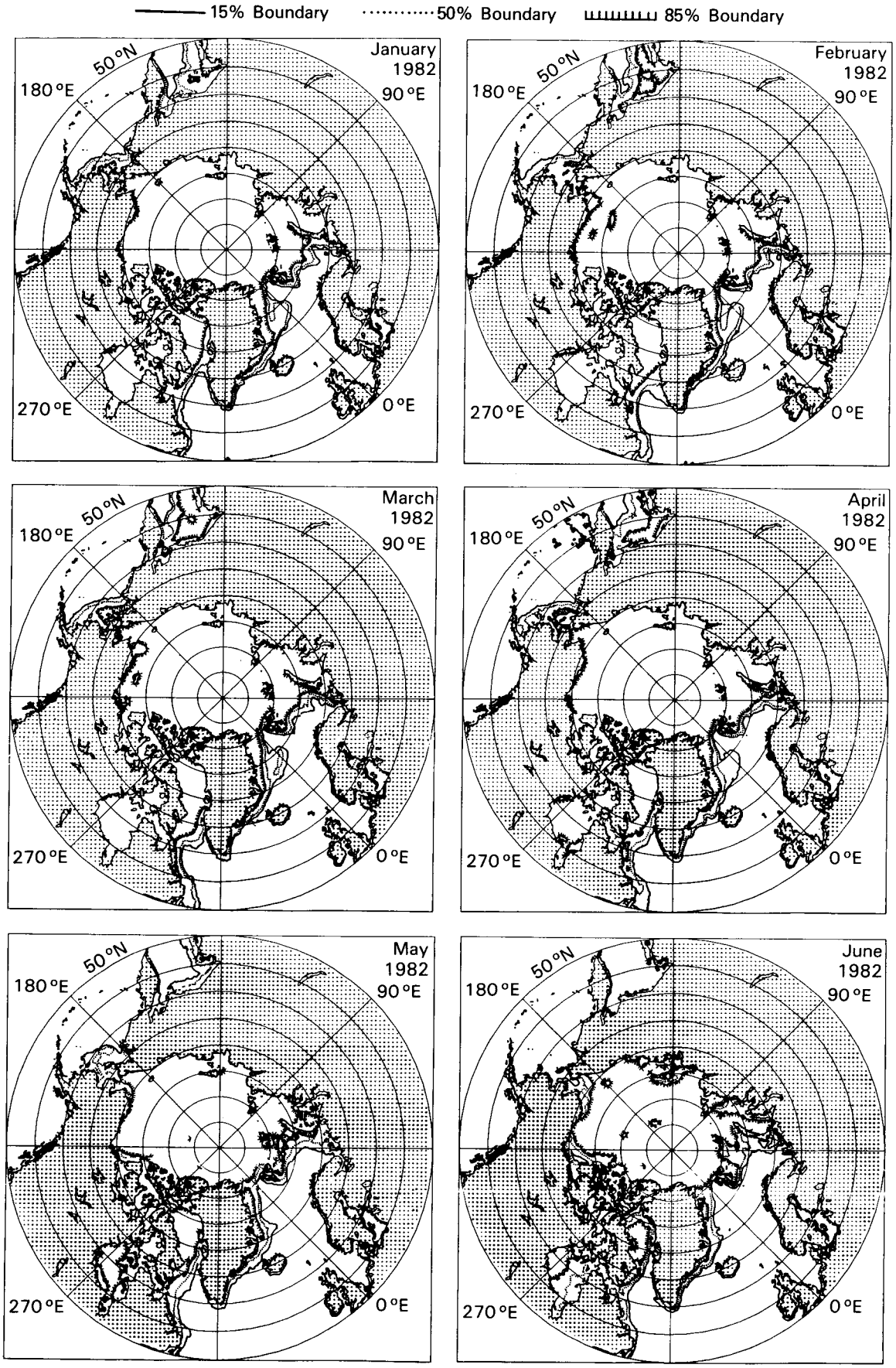

Figure 45. Arctic monthly ice concentration contours for January to June 1982

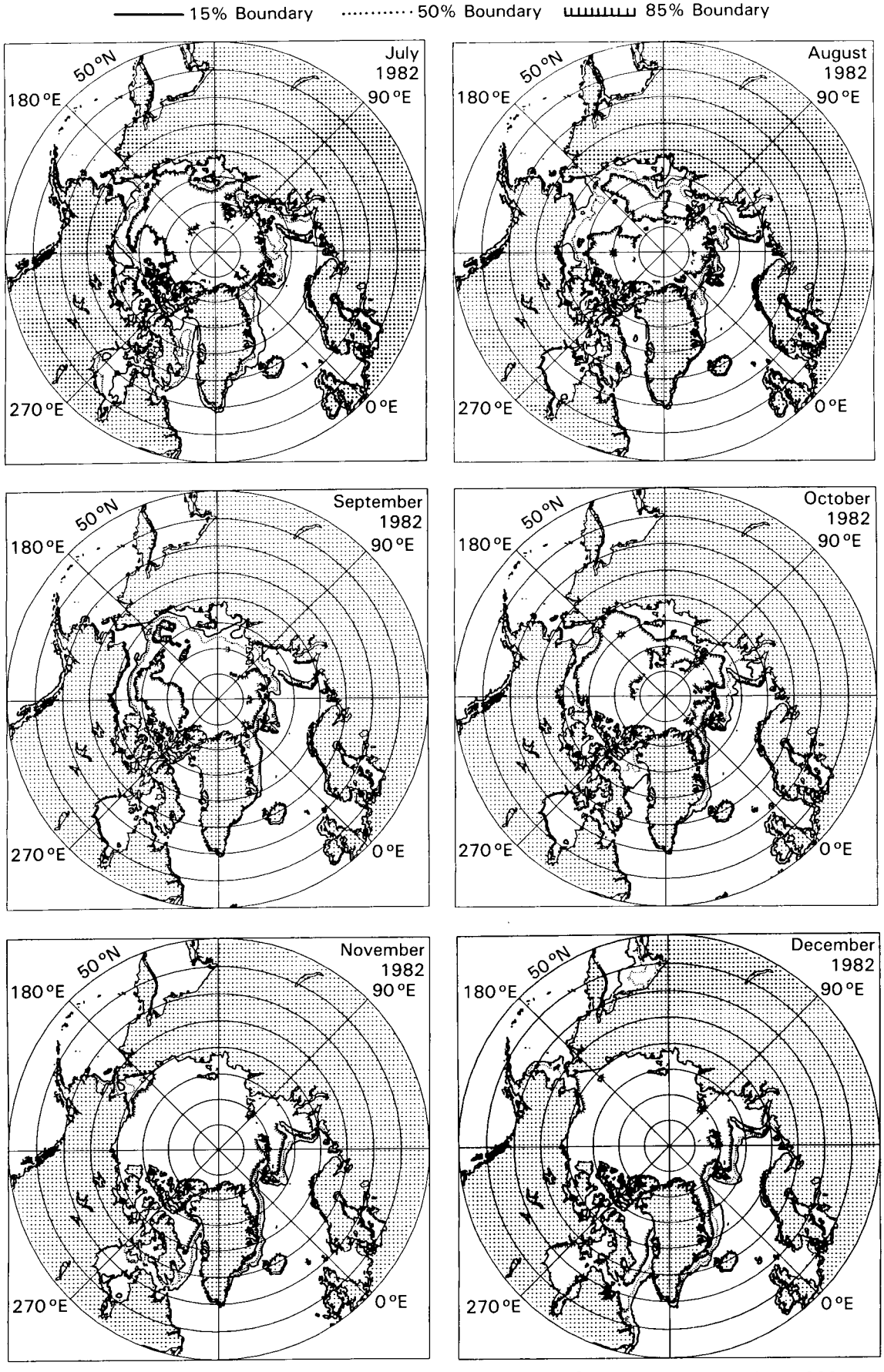

Figure 46. Arctic monthly ice concentration contours for July to December 1982

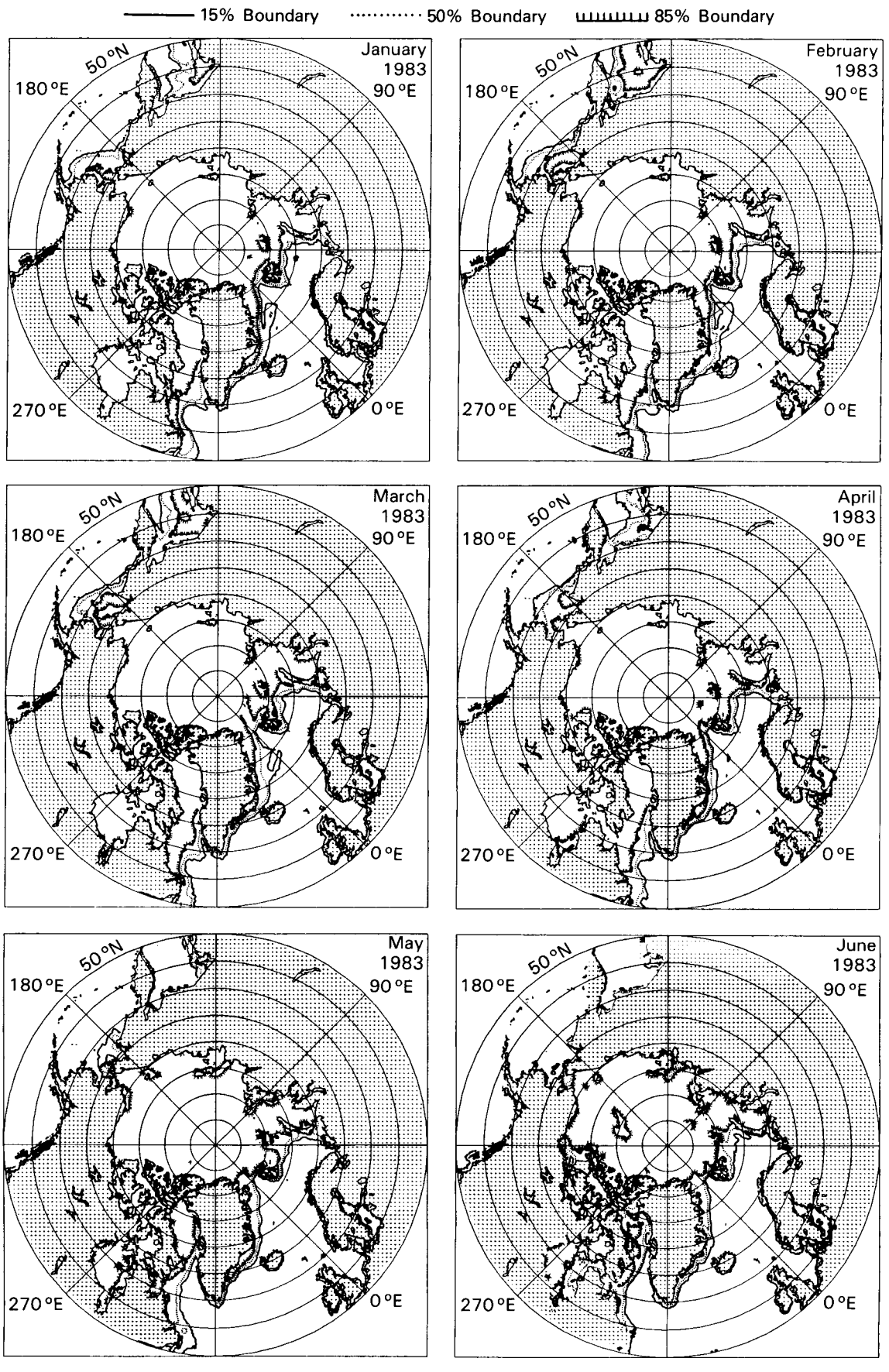

Figure 47. Arctic monthly ice concentration contours for January to June 1983

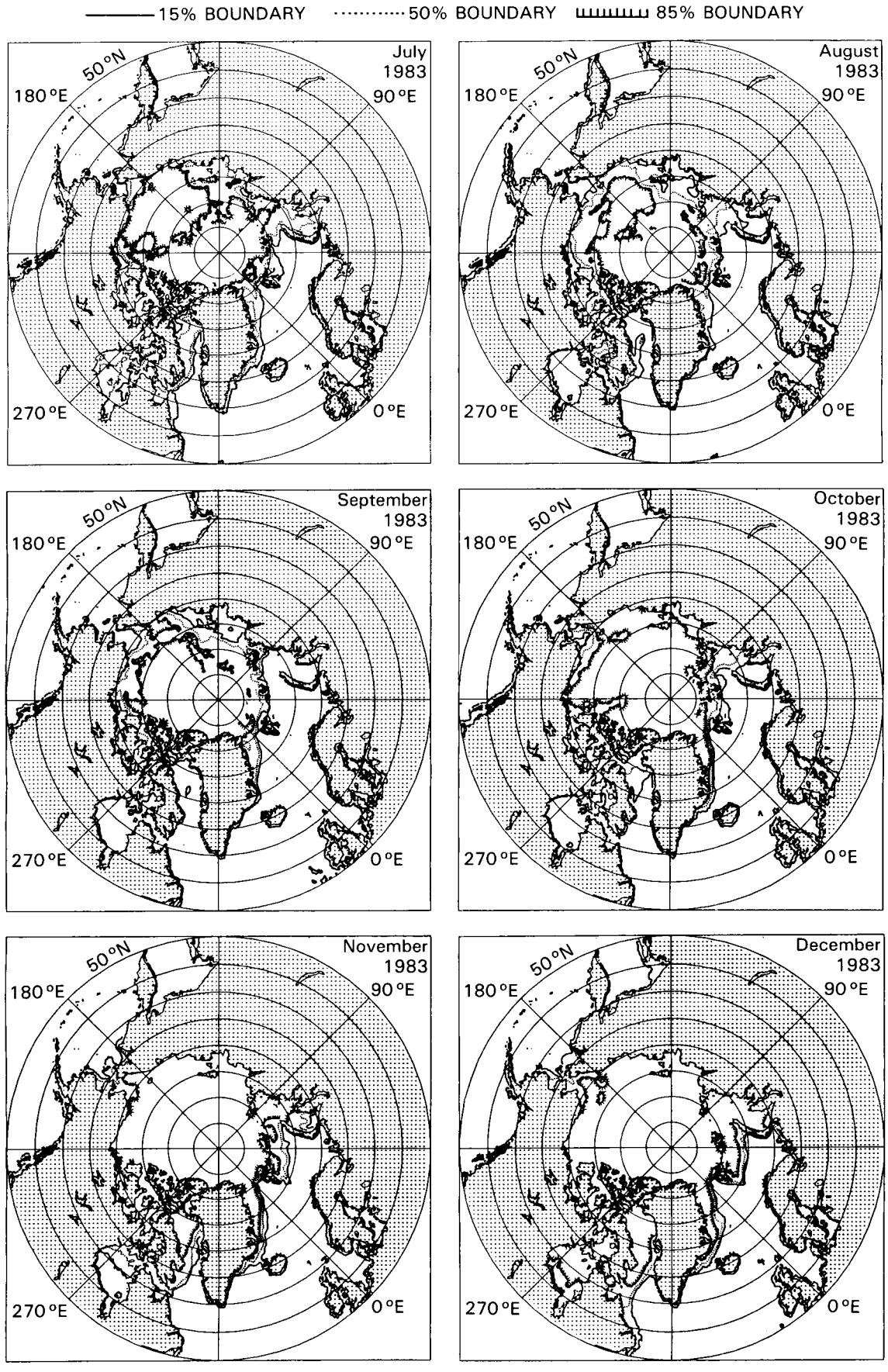

Figure 48. Arctic monthly ice concentration contours for July to December 1983

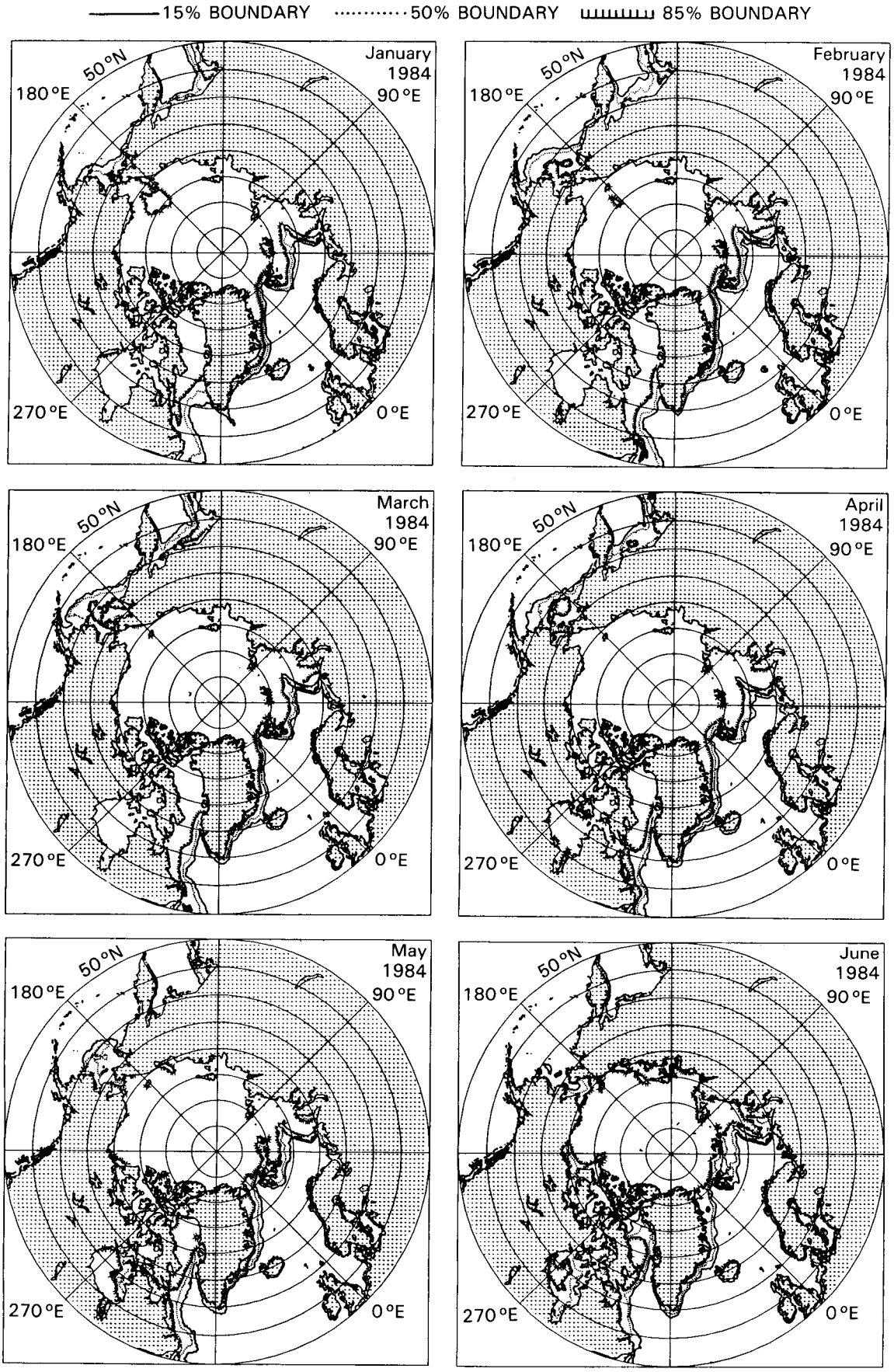

Figure 49. Arctic monthly ice concentration contours for January to June 1984

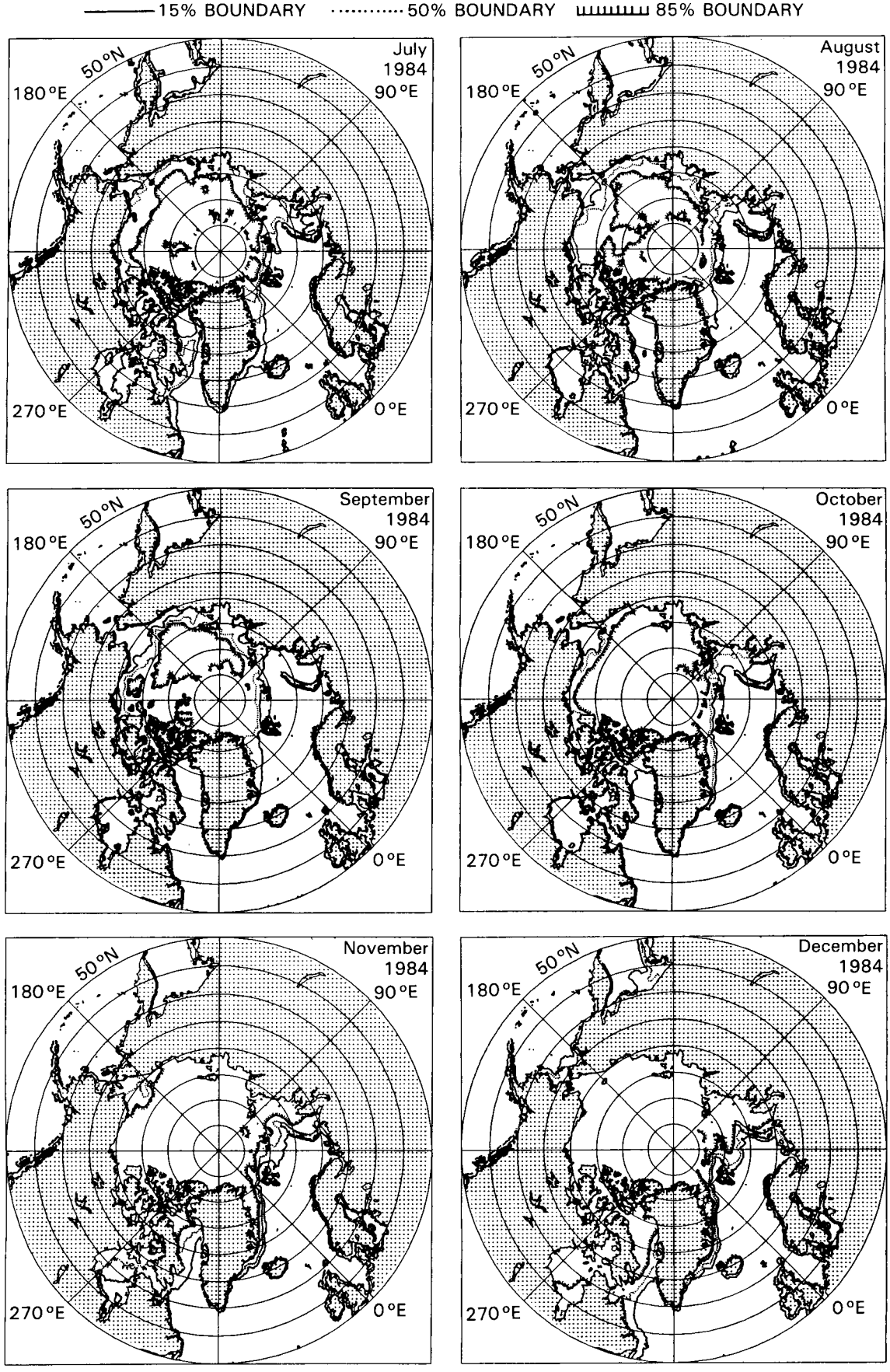

Figure 50. Arctic monthly ice concentration contours for July to December 1984

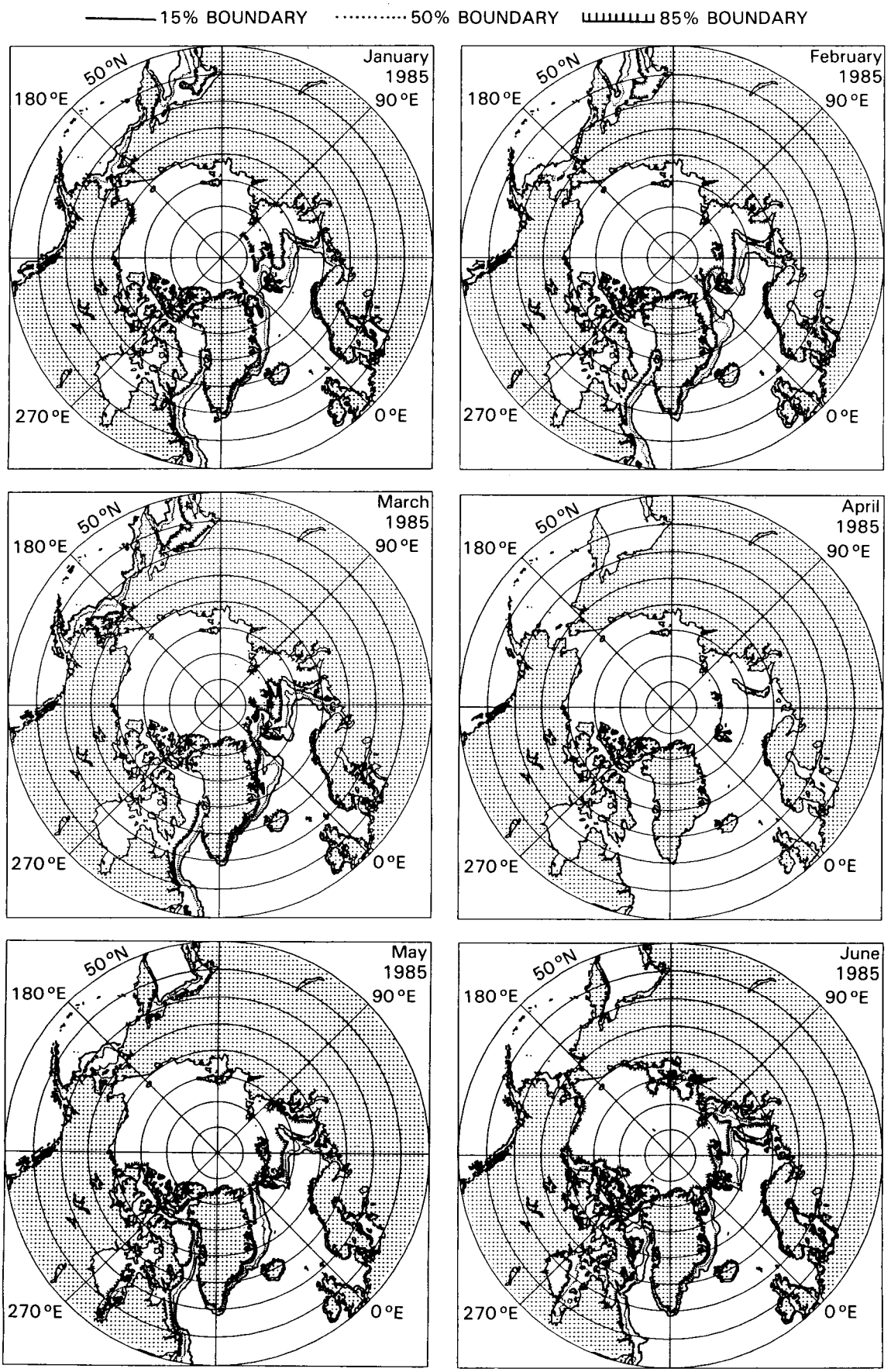

Figure 51. Arctic monthly ice concentration contours for January to June 1985

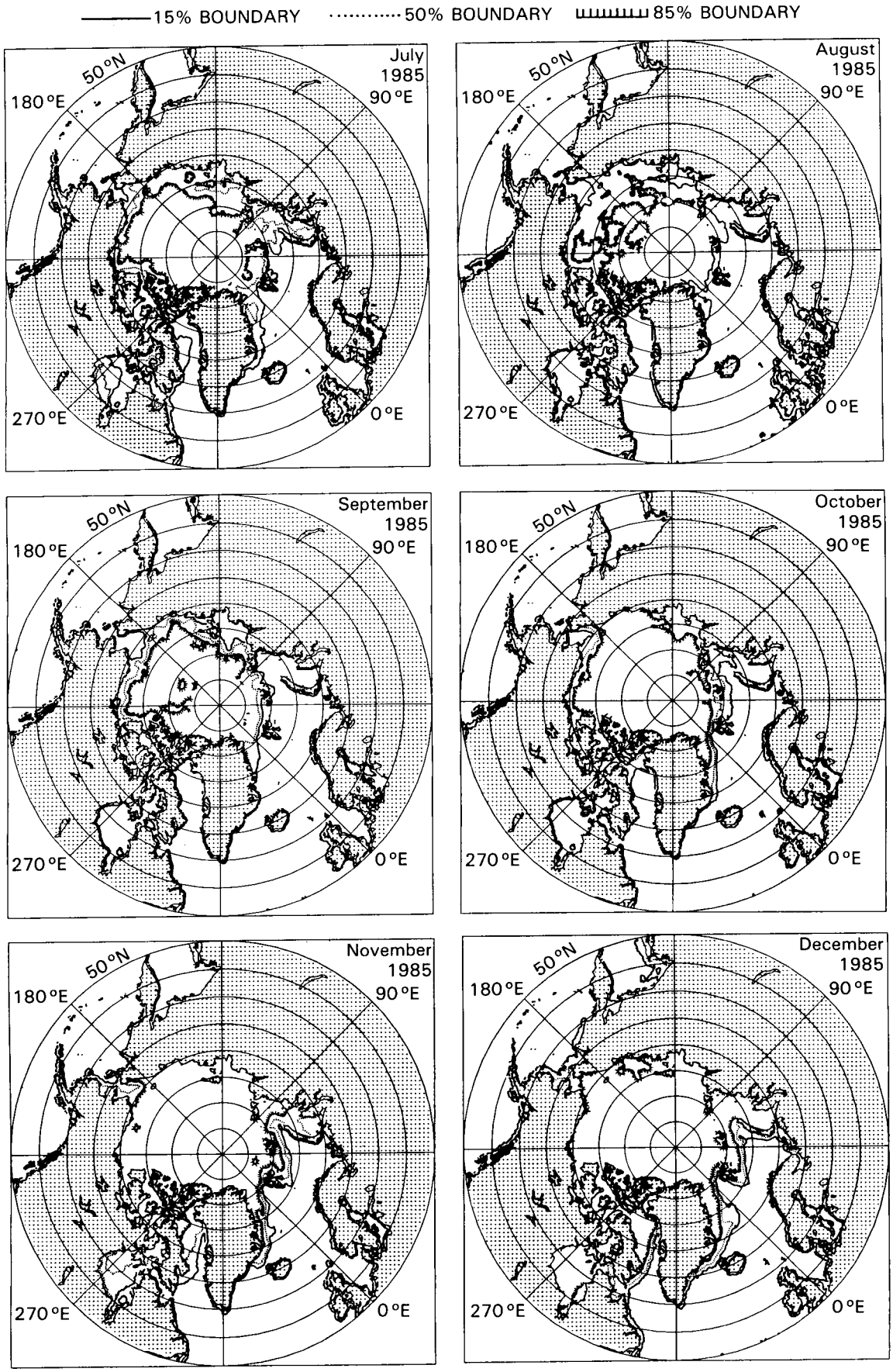

Figure 52. Arctic monthly ice concentration contours for July to December 1985

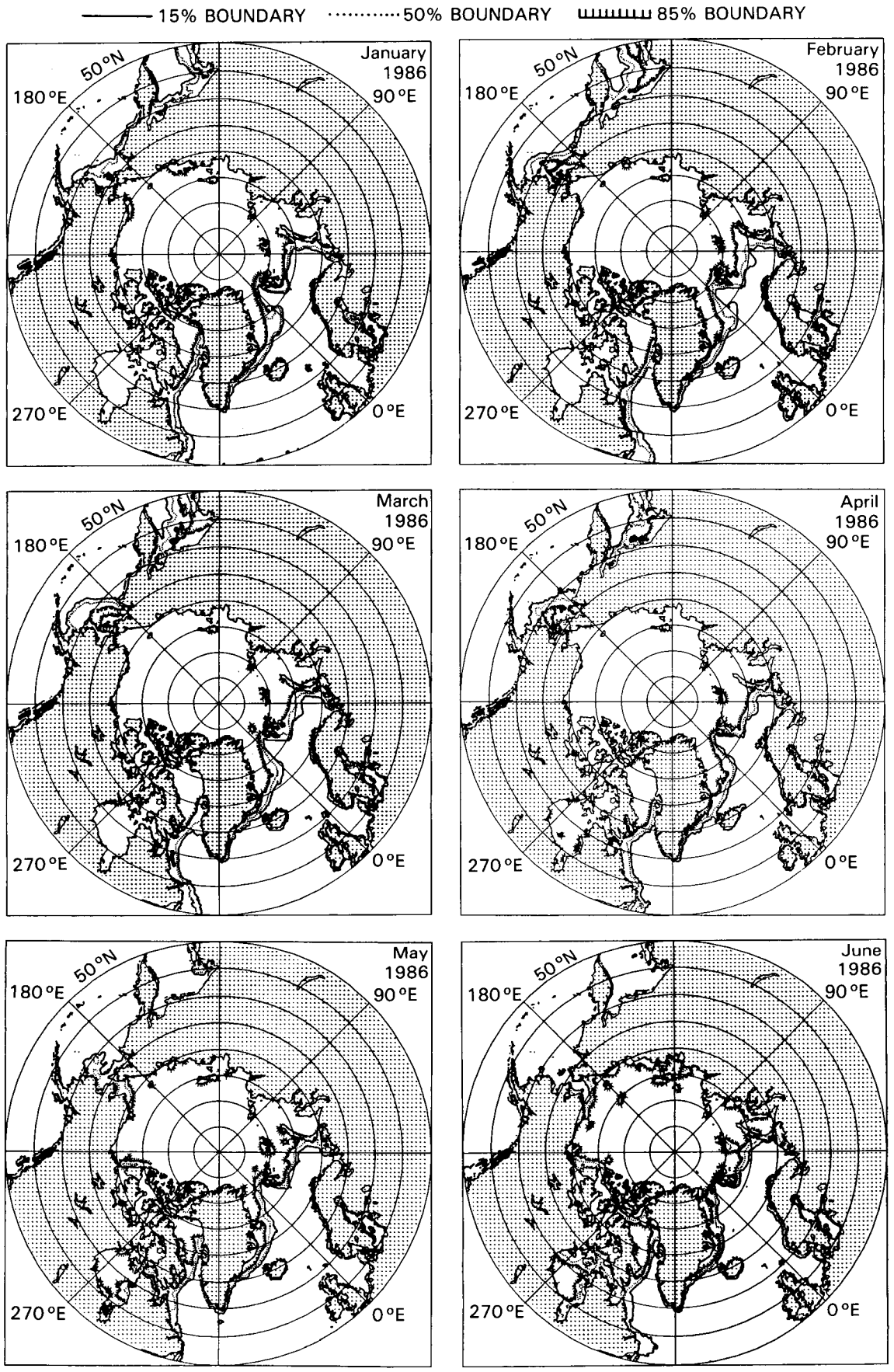

Figure 53. Arctic monthly ice concentration contours for January to June 1986

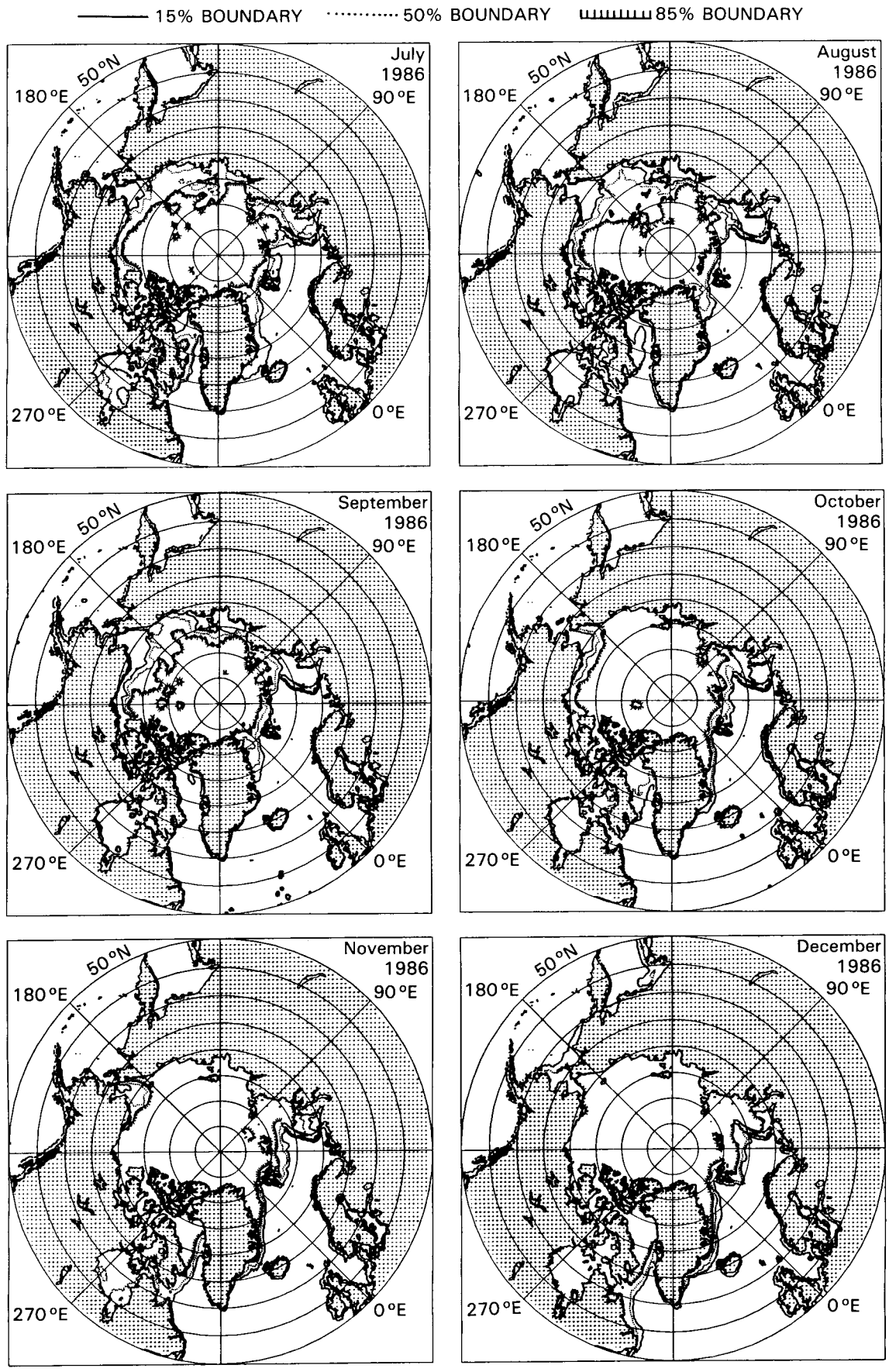

Figure 54. Arctic monthly ice concentration contours for July to August 1986

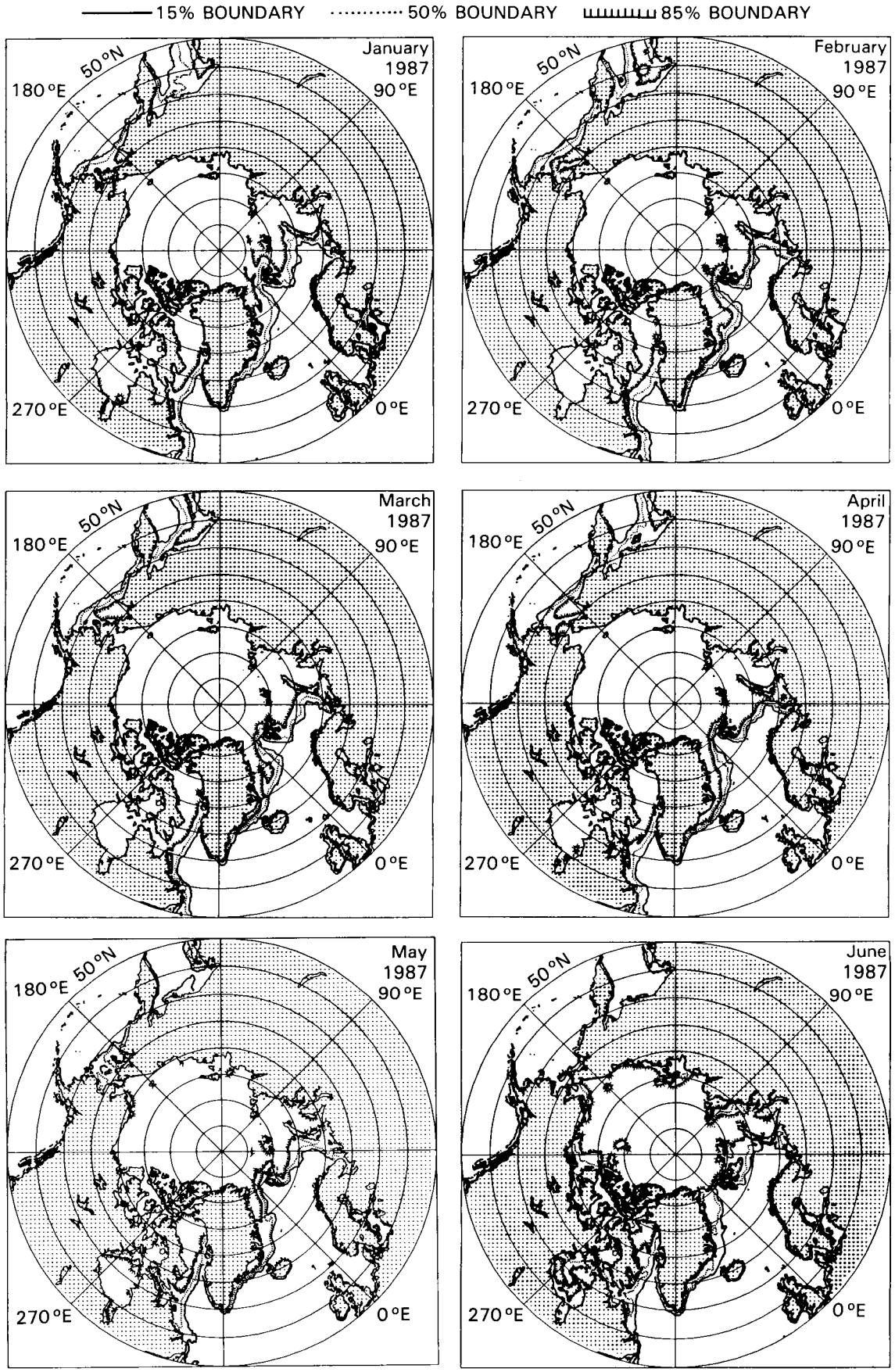

Figure 55. Arctic monthly ice concentration contours for January to June 1987

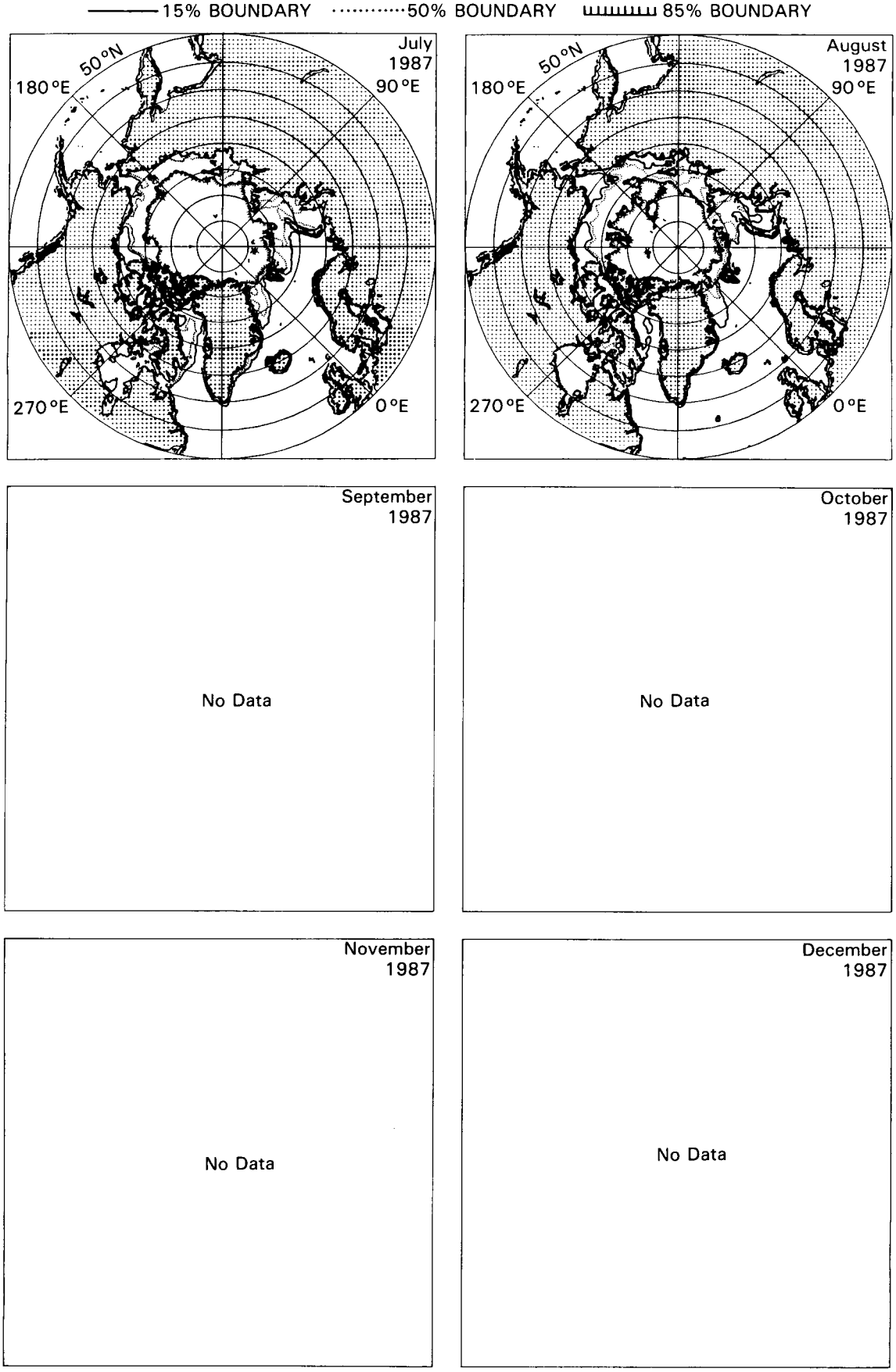

Figure 56. Arctic monthly ice concentration contours for July to August 1987

NASA
National Aeronautics and Space Administration

Report Documentation Page

1. Report No.	2. Government Accession No.	3. Recipient's Catalog No.
NASA RP-1223		

4. Title and Subtitle	5. Report Date
Polar Microwave Brightness Temperatures From Nimbus-7 SMMR - Time Series of Daily and Monthly Maps From 1978 to 1987	July 1989
	6. Performing Organization Code: 671
7. Author(s): Josefino C. Comiso and H. Jay Zwally	8. Performing Organization Report No.: 89B00167
	10. Work Unit No.: 161-40-14-01
9. Performing Organization Name and Address: Goddard Space Flight Center, Greenbelt, Maryland 20771	11. Contract or Grant No.: NAS5-29386
	13. Type of Report and Period Covered: Reference Publication
12. Sponsoring Agency Name and Address: National Aeronautics and Space Administration, Washington, D.C. 20546-0001	14. Sponsoring Agency Code

15. Supplementary Notes

16. Abstract A time series of daily brightness temperature gridded maps (October 25, 1978 through August 15, 1987) have been generated from all ten channels of the Nimbus-7 Scanning Multichannel Microwave Radiometer orbital data. This unique data set can be utilized in a wide range of applications including heat flux, ocean circulation, ice edge productivity, and climate studies. Two sets of data in polar stereographic format are created for the Arctic region: one with a grid size of about 30 km on a 293 by 293 array similar to that previously utilized for the Nimbus-5 Electrically Scanning Microwave Radiometer, while the other has a grid size of about 25 km on a 448 by 304 array identical to what is now being used for the DMSP Scanning Multichannel Microwave Imager. Data generated for the Antarctic region are mapped using the 293 by 293 grid only. The general technique for mapping, and a quality assessment of the data set are presented. Monthly and yearly averages are also generated from the daily data and sample geophysical ice images and products derived from the data are given. Contour plots of monthly ice concentrations derived from the data for October 1978 through August 1987 are presented to demonstrate spatial and temporal detail which this data set can offer, and to show potential research applications.

17. Key Words (Suggested by Author(s))	18. Distribution Statement
Ice Concentrations Microwave Brightness Temperatures Polar Stereographic Gridding Nimbus-7 Scanning Multichannel Microwave Radiometer (SMMR)	Unclassified - Unlimited Subject Category 42

19. Security Classif. (of this report)	20. Security Classif. (of this page)	21. No. of pages	22. Price
Unclassified	Unclassified	112	A06

NASA FORM 1626 OCT 86

NASA-Langley, 1989